Mixing by Ocean Eddies

by

Ryan Abernathey

Submitted to the Department of Earth, Atmospheric, and Planetary
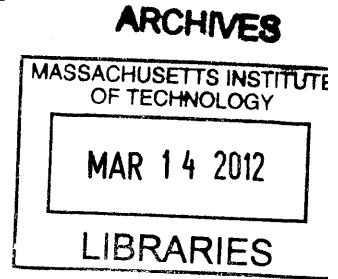Science
in partial fulfillment of the requirements for the degree of

Doctor of Philosophy

at the

MASSACHUSETTS INSTITUTE OF TECHNOLOGY

February 2012

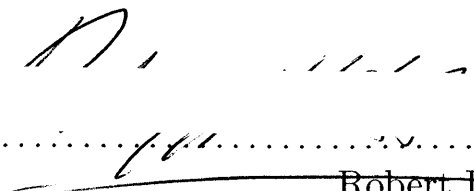Author . . . .
Department of Earth, Atmospheric, and Planetary Science
Feb 1, 2012

Certified by . . . .
John Marshall
Cecil and Ida Green Professor of Oceanography
Thesis Supervisor

Accepted by . . . .
Robert D. van der Hilst
Schlumberger Professor of Geosciences
Head, Department of Earth,Atmospheric and Planetary Sciences

Mixing by Ocean Eddies

by

Ryan Abernathey

Submitted to the Department of Earth, Atmospheric, and Planetary Science
on Feb 1, 2012, in partial fulfillment of the
requirements for the degree of
Doctor of Philosophy

Abstract

Mesoscale eddies mix and transport tracers such as heat and potential vorticity laterally in the ocean. While this transport plays an important role in the climate system, especially in the Southern Ocean, we lack a comprehensive understanding of what sets mixing rates. This thesis seeks to advance this understanding through three related studies. First, mixing rates are diagnosed from an eddy-resolving state estimate of the Southern Ocean, revealing a meridional cross-section of effective diffusivity shaped by the interplay between eddy propagation and mean flow. Effective diffusivity diagnostics are then applied to quantify surface mixing rates globally, using a kinematic model with velocities derived from satellite observations; the diagnosed mixing rates show a rich spatial structure, with especially strong mixing in the tropics and western-boundary-current regions. Finally, an idealized numerical model of the Southern Ocean is analyzed, focusing on the response to changes in wind stress. The sensitivity of the meridional overturning circulation to the wind changes demonstrates the importance of properly capturing eddy mixing rates for large-scale climate problems.

Thesis Supervisor: John Marshall
Title: Cecil and Ida Green Professor of Oceanography

Acknowledgments

First and foremost, I am deeply grateful to my advisor John Marshall. From the very beginning of graduate school, when I was searching for an interesting problem to work on, through today, John's enthusiasm for research and genuine enjoyment of science have been an inspiration and motivation for me. I am in awe of his almost uncanny intuition for ocean dynamics, which, combined with his relentless work ethic and appetite for new problems, makes him a truly exceptional scientist. I am honored to have had the chance to study with him.

Two other people have played crucial roles in my education: David Ferreira and Raffaele Ferrari. David has devoted countless hours to discussing the subtleties of residual-mean theory and the MITgcm with me. Needless to say, I had a lot more to gain from these conversations than he did, and I thank him deeply for his generosity and openness. Likewise, Raf's door has always been open to me when I had questions about turbulence and mixing, and I have learned a great deal from our discussions. Having shared an office with his students for the past two years, I have often felt like an adopted member of the "Ferrari group," an experience for which I am very grateful.

I also wish to thank many other colleagues who have collaborated with me in my work, both as coauthors or just informally through discussions: Emily Shuckburgh, Matt Mazloff, Jean-Michel Campin, Chris Hill, Helen Hill, Ross Tulloch, Brian Rose, Nicolas Barrier, Martha Buckley, Cim Wortham, Malte Jansen, Andreas Klocker, John Taylor, Shafer Smith, Alan Plumb, Jim Ledwell, and Patrick Heimbach. These people have all contributed greatly to my development as a scientist.

I am also deeply grateful for the support of my friends, which, although not of a technical nature, was even more essential to my progress. People seem to come and go in Cambridge with an unfortunate frequency, but this makes the lasting friendships even more valuable. So to those Cambridge friends who have been with me for the long haul—Nick DuBroff, Simon Gustavsson, Mike Halsall, Laura Meredith, Brian Rose, Cim Wortham, Danielle Wenemoser, and Mike Gavino—thank you! Devo ringraziare

anche i miei amici italiani: Giacomo, Gianluca, Nada, Pietro, e Serena.

I could never have reached this point without the love and support of my family. From a young age, my mother Nancy and my father John encouraged my interest in science while allowing my to find my own path. My sister Liz has taught me the meaning of hard work and determination, especially in recent years, and her example inspired me through the difficult times in graduate school.

Finally, no one deserves more thanks than my wonderful girlfriend Chiara. She has been by my side through the frustrations of research, the late nights of writing, and the pressure of impending deadlines. She has been a constant reassuring and calming presence, and a source of happiness when I needed it most. I literally don't know if I could have done it without her.

Contents

List of Figures

13

14

17

List of Tables

19

Chapter 1

Introduction

Understanding the physics of the planet we live on is an essential task for humanity. But beyond practical concerns, something subtle and fascinating beckons scientists to the study of ocean dynamics. At the heart of this fascination lies the immense range of scales present, not merely superimposed on each other, but in interaction. Interaction among different scales is a hallmark of complexity and underlies many of today's great scientific challenges, from the brain to the cell to the stock market. Added to the inherent difficulty of understanding such interactions is the fact that the ocean is so difficult to observe directly. The "long" time scales in the ocean span millennia, far to long for humans to observe directly, while the "short" scales involve, for instance, turbulent wave-breaking events that occur in minutes. The richness of the physics, together with a paucity of observations, makes physical oceanography an exciting and dynamic field to work in, with no shortage of open problems ripe for progress!

One of the great challenges of the past forty years has been to understand the physics of "mesocale" eddies. This unfortunately sterile term has nevertheless achieved universal usage in the field to refer to fluctuations in ocean circulation with the following general properties:

- Spatial scales of roughly 10 - 200 km, the same order as the *deformation radius*

- Low Rossby number; the motions are geostrophically balanced and consequently...

- The circulations are primarily horizontal

- The eddies are believed to arise from baroclinic instability

These motions are ubiquitous in the world oceans and contain an important fraction of the ocean's total energy. Furthermore, mesoscale eddies typify the challenge of scale interaction. It has long been recognized that they derive their energy from an instability of the large-scale background flow. More recent research has led to a growing appreciation of the role in eddies in actually *setting* the large-scale circulation and stratification, in particularly in the Southern Ocean. This two-way scale interaction makes the study of mesoscale eddies a truly rich problem.

One way to frame the role of mesoscale eddies in the large-scale ocean, and the perspective adopted by this thesis, is with the concept of *mixing*: the eddies stir their environment and tend to homogenize background properties. If the mixing rates are known, then the overall effect of the eddies on the large-scale can be understood. Because eddies cannot be resolved in current-generation climate models, their effects must be "parameterized" be specifying a predetermined mixing rate, which in most cases is constant in space and time. Although this thesis is not concerned directly with eddy parameterization, the hypothetical state of constant mixing rates is an important reference point throughout. This assumption of spatially homogenous and unchanging mixing rates underlies all model-based predictions about anthropogenic climate change over the next century, as well as models of past climates such as the last glacial maximum. Our results challenge the assumption of uniform mixing rates and describe some potential consequences for the large-scale ocean circulation of departures from that state.

The three chapters of the thesis each examine the issue of mixing in a different way. The first chapter explores how mixing rates vary with latitude and depth in the Antarctic Circumpolar Current, a region where eddy effects are known to be particularly important, making use of a high-resolution state estimate of the ocean circulation. The second employs satellite observations to calculate mixing rates globally using a diagnostics based on the tracer variance budget. The final chapter de-

scribes an idealized model of the Southern Ocean and shows how the eddy mixing rates, and consequently the meridional overturning circulation, vary with changes in surface wind forcing.

Before delving into these chapters, however, we first give a phenomenological description of ocean eddies. We then review two topics central to the understanding of mesoscale eddies: (1) eddy-mean flow interactions and eddy-driven circulations, and (2) some basic results from baroclinic instability theory. Although this material is by now well-understood in the oceanographic community, it provides a foundation and motivation for the subsequent studies.
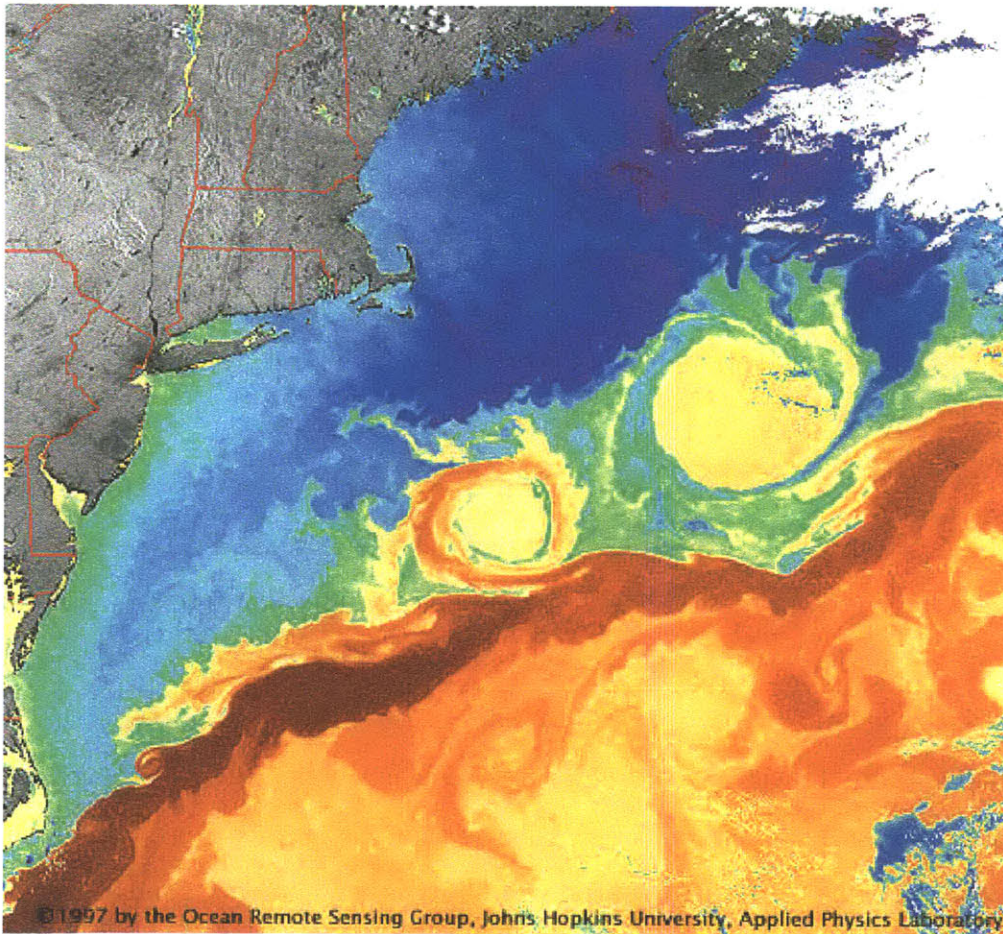
Figure 1-1: A satellite image of sea-surface temperature in the gulf-stream region, from the Advanced Very High Resolution Radiometer (AVHRR) instrument. Color scale is 5° C (dark blue) to 30° C (dark red). Image courtesy of the Ocean Remote Sensing Group, Johns Hopkins University, Applied Physics Laboratory.

1.1 What Are Eddies?

Fig. 1-1 shows a satellite image of sea-surface temperature (SST) in the Gulf Stream region. Mesoscale eddies are clearly visible in the image as the large as swirls and rings of various sizes. These swirling patterns are result from the vortical motion of the underlying currents, which act to stir together warm and cold water, creating the complex and beautiful filamentary structure evident in the image. This "stirring together" of water with different physical properties is precisely what we mean by eddy mixing. This process is fundamentally no different from what happens when you stir milk into your morning coffee; the eddies are acting to homogenize the properties of the fluid, flattening out the temperature gradient across the gulf stream.

Some of the main questions addressed by this thesis arise by simply contemplating this image. There is clearly a region of strongest mixing in the center, with less vigorous stirring to the north and south. So what is the spatial distribution of eddy mixing, how does it vary in the horizontal and the vertical? And how how does one go about *quantifing* the mixing rates at all? These questions are addressed in various ways by Chapters 2 and 3.

Although eddies have long been known to exist in the Gulf Stream region, only since the development of satellite technology has their ubiquity in the global ocean become clear. Satellite observations of sea-surface height can provide instantaneous snapshots of the large-scale scale surface currents. One such snapshot is shown in Fig. 1-2; this figure reveals rings and eddies of many shapes and sizes throughout the Pacific ocean. Indeed, while a few large scale currents are visible (the Kuroshio, the equatorial jets), the overall impression is that the surface flow is *dominated* by eddies. At the same time, great spatial variability is evident, with some regions of the ocean clear devoid of eddies. Chapter 3 makes use of this satellite data to examine the global distribution of mixing at the surface.

Figs. 1-1 and 1-2, taken together, suggest that eddies can play an important role in the global climate system. Seeing the large swirls of warm and cold water in Fig. 1-1 suggests that mixing by eddies can help set the large-scale distribution

1994-11-23
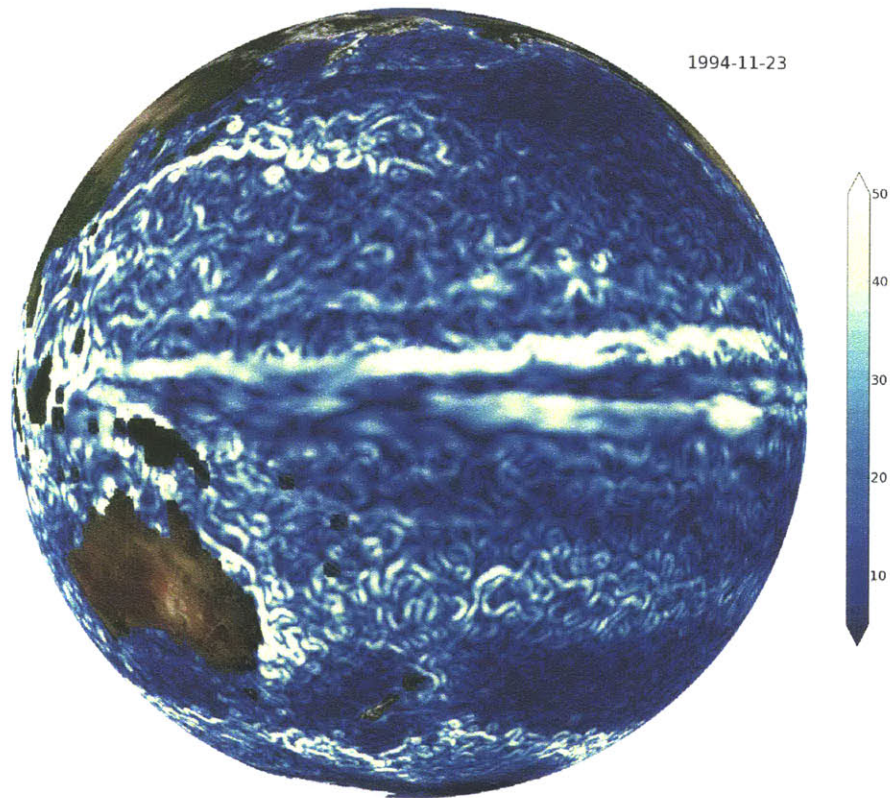
Figure 1-2: A snapshot of the speed of ocean currents in the Pacific as observed by satellite. From the AVISO data archive. The color scale ranges from 0 to 50 cm s^{-1}. Eddies are visible as the numerous rings and curls of the currents.

of important physical quantities: heat, this case, but also salt, density, potential vorticity, and biological nutrients. Indeed we will see shortly that, even though the eddies themselves vanish in long-term averages, the fluxes they produce do not, and these fluxes can have a strong impact on ocean circulation. The ubiquity of eddies throughout the world oceans revealed by 1-2 shows that this effect is not limited to isolated regions.

Indeed, from a climate perspective, this is the main reason for studying eddy mixing. The fluxes of density and potential vorticity have a special relevance for climate because they contribute to the meridional overturning circulation, particularly in the Southern Ocean. Examining how eddy mixing rates vary in response to wind changes, and how this affects the meridional overturning circulation, is a key focus of Chapter 4.

1.2 Eddy-Mean-Flow Interaction in the Ocean

1.2.1 Reynolds Averages

The very notion of *climate* implies some sort of averaging, a smoothing out of short-term and small-scale variations in order to grasp the "big picture." Mathematically, averaging procedure requires separating the long-term climate variables from the "eddies" through some sort of filter, which we will denote generally by an overbar. This filtering operator can be viewed as an average over many realizations of the system (an "ensemble" average) or a long time average over many eddy life-cycles (equivalent to an ensemble average under ergodic conditions). It can also include a spatial smoothing or even a zonal / streamwise average, as is appropriate to the symmetry of the problem in question. For the moment, we remain agnostic about the specific type of averaging and review some general conventions.

A given variable q can then be written as the sum of mean ($\bar{q}$) and eddy (q'), i.e.

$$q(x, y, z, t) = \bar{q} + q'(x, y, z, t) .$$

(1.1)

26

The most essential properties of the average are that $\overline{q'} = 0$ and that $\overline{\overline{q}} = \overline{q}$. The averaging is frequently assumed to be linear, such that $\overline{\phi q} = \phi \overline{q}$ (where ϕ is a constant), and $\overline{p + q} = \overline{p} + \overline{q}$. (The assumption of linearity can be relaxed(Gent and McWilliams, 1996), although we will not consider this case.) Applying this operator to the fluid governing equations yields a *Reynolds average* form of the equations. Consider, for instance, the equation for the transport of a scalar q with source / sink Q:

$$\frac{\partial q}{\partial t} + \boldsymbol{u} \cdot \nabla q = Q \ . \tag{1.2}$$

Averaging this equation provides an equation for the evolution of $\overline{q}$:

$$\frac{\partial \overline{q}}{\partial t} + \overline{\boldsymbol{u}} \cdot \nabla \overline{q} = -\nabla \cdot \overline{\boldsymbol{u}'q} + \overline{Q} \ . \tag{1.3}$$

This equation is identical to the un-averaged equation for q, except for the addition of the eddy flux divergence term $\nabla \cdot \overline{\boldsymbol{u}'q}$ on the right-hand side. In general, closure theories for turbulence focus on predicting the form of these eddy fluxes in terms of other mean quantities.

1.2.2 Transformed Eulerian Mean

To illustrate more specifically how eddy fluxes can impact ocean general circulation, we consider a canonical configuration pertinent to the Southern Ocean: a zonally re-entrant channel forced by momentum and buoyancy fluxes at the surface. This model is similar to that of Marshall and Radko (2003) and is the inspiration for the numerical experiments described in the last chapter. Here we will keep things simple by just considering the quasi-geostrophic form of the equations, which contain the essential elements. They key point of this section is to see how eddies can cause a transport analogous to advection, rather than just mixing diffusively. The potential importance of this transport for the large-scale circulation is a key motivation for the subsequent investigation of mixing rates.

We begin with the inviscid Boussinesq momentum equation:

$$\frac{\partial \boldsymbol{u}}{\partial t} + \boldsymbol{u} \cdot \nabla \boldsymbol{u} + f\hat{\boldsymbol{k}} \times \boldsymbol{u} = -\frac{1}{\rho_0}\nabla p + b\hat{\boldsymbol{k}} + \frac{1}{\rho_0}\frac{\partial \boldsymbol{\tau}}{\partial z} \; . \tag{1.4}$$

The stress $\boldsymbol{\tau}$ includes externally applied stresses such as wind and bottom drag, b is the buoyancy, and ρ_0 is a constant reference density. Our averaging operator, a so-called *Eulerian mean*, will indicate an average in time as well as zonally (x-direction) at constant depth, such that $\partial \bar{q}/\partial t = \partial \bar{q}/\partial x = 0$. Applying this average to (1.4) yields the equation for the zonally-averaged steady-state momentum equation:

$$-f\bar{v} + \bar{v}\frac{\partial \bar{u}}{\partial y} + \bar{w}\frac{\partial \bar{u}}{\partial z} = -\frac{\partial}{\partial y}(\overline{u'v'}) - \frac{\partial}{\partial z}(\overline{u'w'}) + \frac{1}{\rho_0}\frac{\partial \overline{\tau^x}}{\partial z} \tag{1.5}$$

Applying standard quasi-geostrophic scaling arguments (see Pedlosky, 1987; Vallis, 2006) to this equation yields a simple approximate form:

$$-f\bar{v} = -\frac{\partial}{\partial y}\overline{u'v'} + \frac{1}{\rho_0}\frac{\partial \overline{\tau^x}}{\partial z} \; . \tag{1.6}$$

The Reynolds stress term $\overline{u'v'}$, capable of transferring momentum meridionally, is very important for atmospheric dynamics, but somewhat less so for the ocean.

We can define a streamfunction for the mean meridional overturning in the y-z plane: $\bar{v} = -\partial\overline{\Psi}/\partial z$, $\bar{w} = \partial\overline{\Psi}/\partial y$. Integrating (1.6) from the surface to any interior point outside of the Ekman layer, and neglecting the $\overline{u'v'}$ term, gives

$$\overline{\Psi} = -\frac{\overline{\tau_s^x}}{f\rho_0} \; , \tag{1.7}$$

where $\overline{\tau_s^x}$ is the wind stress applied at the surface. This shows that the Eulerian-mean overturning circulation simply reflects the Ekman transport induced by the surface wind. Similarly, integrating (1.6) in z from top to bottom yields the simple stress balance $\overline{\tau_s^x}(y) = \overline{\tau_b^x}(y)$ where $\overline{\tau_b^x}$ is the bottom stress (Munk and Palmén, 1951; Johnson and Bryden, 1989; Olbers, 1998). In a Southern Ocean context, $\overline{\tau_b^x}$ might represent topographic form stress, but the specific form of the bottom stress is not

important for our purposes here.

The baroclinic part of the mean zonal flow $\bar{u}(y, z)$ is determined by the thermal wind equation:

$$f\frac{\partial \bar{u}}{\partial z} = -\frac{\partial \bar{b}}{\partial y} \ . \tag{1.8}$$

To determine the buoyancy distribution, one must consider the zonally-averaged buoyancy budget. With a buoyancy flux $\mathcal{B}$ applied at the surface, the full zonally-averaged buoyancy equation is

$$\bar{v}\frac{\partial \bar{b}}{\partial y} + \bar{w}\frac{\partial \bar{b}}{\partial z} = -\frac{\partial}{\partial y}(\overline{v'b'}) - \frac{\partial}{\partial z}(\overline{w'b'}) - \frac{\partial}{\partial z}\mathcal{B} + \kappa\frac{\partial \bar{b}}{\partial z} \ . \tag{1.9}$$

From here on, we will neglect the vertical diffusion term in the buoyancy budget, restricting ourselves to the nearly adiabatic regime of ocean circulation in the main thermocline. Diabatic mixing certainly play a crucial role in the ocean, and an extensive literature exists on its effects. Increasingly convincing experimental evidence (Ledwell et al., 1998, 2011) and theoretical arguments (Toggweiler and Samuels, 1998; Wolfe and Cessi, 2011), however, have suggested that much of the upper ocean overturning circulation can be understood without invoking diabatic mixing. Again applying quasi-geostrophic scaling, the budget then reduces to

$$\bar{w}\frac{\partial \bar{b}}{\partial z} = -\frac{\partial}{\partial y}(\overline{v'b'}) - \frac{\partial}{\partial z}\mathcal{B} \ . \tag{1.10}$$

The primary difficulty in solving (1.10) is the presence of the eddy buoyancy flux term on the right side. A technique that has proved extremely useful in both atmospheric and oceanic problems is to transform the equation to represent part of the eddy flux as advection, a so-called *transformed Eulerian mean* or *TEM* formulation(Andrews and McIntyre, 1976; Andrews et al., 1987; Marshall and Radko, 2003; Plumb and Ferrari, 2005). This is possible because the divergence of eddy fluxes directed along the mean buoyancy gradient, called *skew fluxes*, have the same mathematical form as advection terms. The eddy advection can then be combined with the mean advection

29

in a residual streamfunction Ψ_{res}:

$$\Psi_{res} = \overline{\Psi} + \Psi^* .\qquad(1.11)$$

Plumb and Ferrari (2005) emphasize that the TEM eddy streamfunction is not unique and discuss the various trade-offs for different choices. However, in a quasi-geostrophic context, there is only one possibility:

$$\Psi^* = \frac{\overline{v'b'}}{\overline{b}_z}\qquad(1.12)$$

Since $w_{res} = \partial\Psi_{res}/\partial y$, we see that (1.10) can be written as

$$w_{res}\frac{\partial\overline{b}}{\partial z} = -\frac{\partial}{\partial z}\overline{\mathcal{B}} .\qquad(1.13)$$

The eddy flux has been subsumed completely into the residual advection, which must be balanced by the diabatic flux $\overline{\mathcal{B}}$.[1] The TEM form of the momentum equation, obtained by adding $-fv^*$ to (1.6) is,

$$-fv_{res} = \overline{v'q'} + \frac{1}{\rho_0}\frac{\partial\overline{\tau^x}}{\partial z} .\qquad(1.14)$$

where

$$\overline{v'q'} = -\frac{\partial}{\partial y}\overline{u'v'} + \frac{\partial}{\partial z}\left(f\frac{\overline{v'b'}}{\overline{b}_z}\right)\qquad(1.15)$$

is the eddy flux of quasi-geostrophic potential vorticity (QGPV), equivalent to the divergence of the Eliassen-Palm flux. The effect of the eddies on the residual circulation evidently all boils down to this term.

One useful simplification that can be made is to neglect the $\overline{u'v'}$ term; as previously mentioned, this term is negligble on scales larger than the deformation radius (Vallis,

---

[1]In general (i.e. in non-quasi-geostrophic cases), a part of the eddy flux may be left over, unable to be absorbed into Ψ_{res}. This "diabatic eddy flux" is discussed by Treguier et al. (1997) and Marshall and Radko (2003), and Plumb and Ferrari (2005).

2006, p. 706). This allows us to define a zonal "eddy stress" as

$$\tau_e^x = \rho_0 f \frac{\partial}{\partial z} \left(\frac{\overline{v'b'}}{\overline{b}_z} \right)$$ (1.16)

and rewrite the momentum equation as

$$- f v_{res} = \frac{1}{\rho_0} \frac{\partial}{\partial z} (\overline{\tau_s^x} + \tau_e^x) .$$ (1.17)

The eddy stress here plays a role very similar to the wind stress. One interpretation of this form of the equation is that the coriolis force on the residual velocity v_{res} is balanced by the divergence of both external and eddy stresses.

We have shown how the effect of eddies in this QG channel flow can be represented as an advection by a residual circulation. We transformed the momentum and buoyancy equations to use this residual circulation instead of the standard eulerian-mean circulation, and as a result the eddy terms were completely eliminated from the buoyancy equation. In the transformed momentum equation, the eddy flux of QGPV acts as a forcing of the residual flow. We will now show how this forcing is related to eddy mixing.

1.2.3   Eddy Diffusivity

To fully "close" the eddy-mean-flow interaction problem described above, one must somehow relate the unknown eddy fluxes to the background state. The most straightforward approach is to use a down-gradient diffusive closure for the QGPV flux, such that

$$\overline{v'q'} = -K_q \frac{\partial \overline{q}}{\partial y} .$$ (1.18)

Here K_q is a diffusivity and

$$\frac{\partial \overline{q}}{\partial y} = \beta - \frac{\partial^2 \overline{u}}{\partial y^2} - f \frac{\partial s}{\partial z}$$ (1.19)

31

is the background QGPV gradient. The variable $s = \overline{b}_y/\overline{b}_z$ is the mean isopycnal slope. Arguments based on the eddy enstrophy budget (Rhines, 1979; Rhines and Young, 1982) indicate that in general K_q must be positive, causing QGPV to diffuse down the mean gradient. If this coefficient is known, then the strength and sense of the residual flow can be inferred. Because QGPV obeys a conservation equation equivalent to a passive tracer, the diagnostics of mixing based on passive tracers described in the subsequent subsequent are closely related to K_q.

An alternative approach that is very common in oceanography is to instead make a closure based on the horizontal flux of buoyancy:

$$K_b = -\overline{v'b'}/\overline{b}_y \ . \tag{1.20}$$

This allows the eddy stress to be written as $\tau_e^x = \rho_0 f K_b s$. This form is convenient because it leads to a closure for the whole eddy streamfunction, rather than the eddy-induced velocity v^*. This is particularly useful in ocean models. For instance, the common eddy parameterization of Gent and McWilliams (1990) assumes that K_b has a constant value, usually 1000 m^2 s^{-1}; this parameterization has been demonstrated to make a substantial improvement to ocean models (Danabasoglu and McWilliams, 1995). However, this closure is not based on a variance budget, and in general there is no reason to assume that K_b is positive.

We can see that the diffusivities for QGPV and buoyancy are related by (Smith and Marshall, 2009)

$$K_q \left(\frac{\partial s}{\partial z} + \frac{\overline{u}_{yy} - \beta}{f} \right) = \frac{\partial}{\partial z}(K_b s) \ . \tag{1.21}$$

If K_b is constant in the vertical (as assumed in the Gent-McWilliams parameterization), and if the β and $\overline{u}_{yy}$ terms on the left are small compared to the slope term, then the two diffusivities are equal. But when the diffusivities vary in z, a central focus of Chapter 2, one must be clear about whether the eddy diffusivity in question applies to QGPV or buoyancy. We will make use of diffusive closures for both buoyancy and QGPV at various points in this thesis, as each has its own distinct advantages.

This brief review of eddy-mean-flow interaction shows how mesoscale eddies can

play an important role in both the momentum and buoyancy budgets of the ocean, primarily through the effect of an eddy-driven circulation Ψ^*. The strength of this circulation can be related to eddy fluxes of buoyancy and potential vorticity. These fluxes, in turn, can be related to the large-scale gradients through diffusive closures. When expressed in this form, the main challenge in understanding the eddy behavior lies in determining the eddy diffusivities, i.e. the mixing rates.

1.3   Baroclinic Instability

The eddy-mean-flow interaction framework just described focuses on how eddies can influence the large scale circulation in an idealized channel flow. Linear baroclinic instability analysis allows us to consider the converse problem—how does the large scale background state lead to the formation of eddies? The concept of baroclinic instability first arose in atmospheric science to explain the origin of mid-latitude weather systems. Charney (1947) and Eady (1949) independently developed analytical models, based on idealized, zonally-symmetric background states representative of the atmosphere, which predicted the rapid growth of unstable waves. The most unstable waves in these models have scales around the first baroclinic deformation radius, $L_d = NH/f$, where N is the background stratification, H the depth, and f the coriolis parameter. Lorenz (1955) gave an elegant interpretation of baroclinic instability in terms of the energy cycle: the baroclinic instability process converts *available potential energy* (APE) of the background density distribution into eddy kinetic energy (EKE).

The seminal work of Gill et al. (1974, henceforth GGS) recognized baroclinic instability to be the source of energy for ocean mesoscale eddies as well. The basic energy cycle described by GGS is still accepted today, albeit with more complexities (Wunsch and Ferrari, 2004; Cessi et al., 2006): winds create potential energy on the large scale through Ekman pumping, causing the contours of density (isopycnals) to slope in the bowl-shaped pycnocline of the mid-latitude gyres; this density configuration is generally unstable to deformation-scale perturbations, which grow in to mesoscale eddies;

33

the eddies dissipate energy when they come into contact with frictional boundary layers. Thus the large scale ocean exists in a state of *forced-dissipative equilibrium*, with eddies playing an important role in the energy cycle.

GGS restricted their stability analysis to a few characteristic hydrographic profiles, but Smith (2007) recently performed a similar analysis globally to construct a comprehensive atlas of baroclinic instability, revealing strong correlations between instability and eddy energy. Here will review some of the important, basic results of baroclinic instability theory in the context of the idealized channel flow described above.

1.3.1   The Stability Problem

Linear QG theory requires the specification of a background stratification and shear (Pedlosky, 1987). The stratification is expressed as a BruntVäisälä frequency $N^2(z) = \partial B/\partial z$. The background mean flow is in thermal wind balance with the meridional gradient in buoyancy: $f\partial U(z)/\partial z = -\partial B/\partial y$. (Any depth-independent mean U can be removed with a Galliean transform without affecting the results of the stability analysis.) These background states can be viewed as representative of a particular latitude y in the zonally-averaged model described in the previous section, with B analogous to $\bar{b}$. Together, the specification of $N(z)$ and $U(z)$, along with β, the planetary vorticity gradient, defines a background potential-vorticity gradient

$$Q_y = \beta - f\frac{\partial s}{\partial z} \tag{1.22}$$

where $s = -(\partial B/\partial y)/(\partial B/\partial z)$ is the large-scale isopycnal slope.

The evolution of eddy quasigeostrophic PV (QGPV) governs the whole system. The eddy QGPV is defined as

$$q = \nabla^2\psi + \frac{\partial}{\partial z}\left(\frac{f^2}{N^2}\frac{\partial \psi}{\partial z}\right) \tag{1.23}$$

where ψ is the streamfunction for the eddy flow, such that $u = -\partial\psi/\partial y$, $v = \partial\psi/\partial x$.

The evolution of q for a flat-bottomed ocean of depth H is governed by the linearized equations

$$\frac{\partial q}{\partial t} + U\frac{\partial q}{\partial x} + \frac{\partial \psi}{\partial x}Q_y = 0 \qquad\qquad -H < z < 0 \qquad (1.24)$$

$$\frac{\partial b}{\partial t} + U\frac{\partial b}{\partial x} + \frac{\partial \psi}{\partial x}B_y = 0 \qquad\qquad z = -H,\ z = 0 \qquad (1.25)$$

where $b = f\partial\psi/\partial z$ is the eddy buoyancy anomaly. Assuming wavelike solutions for ψ, such that $\psi = \mathcal{R}e[\hat{\psi}(z)\exp[i(kx + \ell y - \omega t)]]$, the governing equations reduce to a linear eigenvalue problem for $\hat{\psi}(z)$, the complex amplitude:

$$(U - c)\left[-K^2 + \frac{d}{dz}\left(\frac{f^2}{N^2}\frac{d}{dz}\right)\right]\hat{\psi} = -Q_y\hat{\psi} \qquad\qquad -H < z < 0 \qquad (1.26)$$

$$(U - c)\frac{\partial}{\partial z}\hat{\psi} = -\frac{1}{f}B_y\hat{\psi} \qquad z = -H,\ z = 0 \qquad (1.27)$$

where $c = \omega/k = c_r + ic_i$ is the complex phase speed and $K^2 = k^2 + \ell^2$.

The problem specified in (1.26) & (1.27) can be solved analytically for simple profiles of $N^2(z)$ and $U(z)$, or numerically for arbitrary profiles. The solution consists of a set of vertical normal modes $\hat{\psi}$, which describe the vertical structure of the perturbations, and a complex phase speed c for each k. If c is purely real, the perturbations are stable waves, equivalent to Rossby waves or Eady edge waves for boundary-trapped modes. If c contains an imaginary component, the perturbations grow exponentially at the growth rate $\sigma = kc_i$.

1.3.2   Conditions for Instability

From this general instability problem, Charney and Stern (1962) derived a very useful criteria for when unstable modes can occur. If we multiply (1.26) by $\hat{\psi}^*$ (the complex conjugate), integrate in z from $-H$ to 0, and use (1.27) for the boundary values, we find

$$\int_{-H}^{0}\left(\frac{f^2}{N^2}|\frac{\partial\hat{\psi}}{\partial z}|^2 - K^2|\hat{\psi}|^2\right)dz = -\int_{-H}^{0}\frac{Q_y}{U - c}dz - \frac{f}{N^2}\left[\frac{B_y}{U - c}\right]_{-H}^{0} \qquad (1.28)$$

35

The left-hand side of the equation is purely real, and consequently the imaginary part on the right must be zero. This imaginary part can be written as

$$c_i \left\{ \int_{-H}^{0} \frac{Q_y}{(U - c_r)^2 + c_i^2} dz - \frac{f}{N^2} \left[\frac{B_y}{(U - c_r)^2 + c_i^2} \right]_{-H}^{0} \right\} = 0 \ . \qquad (1.29)$$

This equation reveals the famous *Charney-Stern criteria* for baroclinic instability. For c_i to be non-zero, the expression in brackets must vanish: this can be accomplished through a reversal of the interior PV gradient, by cancellation between the surface and bottom buoyancy gradients, or some combination. The relationship between PV gradients and eddy mixing rates will be taken up in Chapter 2.

1.3.3 Linear QGPV Diffusivity

A bridge between this discussion of linear baroclinic instability and the eddy-mean-flow interaction problem in the previous section can be built by considering the eddy flux of QGPV $\overline{v'q'}$. Recall that this expression appeared as a force in the TEM momentum equation. Linear theory offers a prediction for its general form, but not its magnitude (Green, 1970; Marshall, 1981; Killworth, 1997; Smith and Marshall, 2009). Specifically, we find

$$\overline{v'q'} = \frac{1}{2} \mathcal{R}e \left\{ \frac{\partial \psi}{\partial x} q^* \right\} = -\frac{k c_i}{2} |\hat{\psi}|^2 \frac{Q_y}{c_i^2 + (U - c_r)^2} \qquad (1.30)$$

The QGPV flux is everywhere down the mean gradient Q_y, a result expected more generally from quasi-geostrophic turbulence theory (Rhines and Young, 1982; Rhines, 1979). The implied diffusivity is

$$K_q = -\frac{\overline{v'q'}}{Q_y} = \frac{1}{2} \frac{k c_i |\hat{\psi}|^2}{c_i^2 + (U - c_r)^2} \ . \qquad (1.31)$$

The magnitude of the diffusivity, proportional to the growth rate, reflects a fundamental limitation of linear theory: the inability to predict the finite-amplitude equilibrated strength of the eddies. However, its vertical structure provides a useful

36

reference point for interpreting diffusivities inferred by other means. Notably (1.31) predicts a diffusivity with a vertical structure which is enhanced at a *critical level* z_c, where $U(z_c) = c_r$. That is, the mixing of PV is enhanced where the real part of the phase speed, which represents propogation, is equal to the ambient mean flow speed. The notion of critical layer-enhancement is also quite general and can be derived from basic kinematics (Plumb, 2007). The concept of critical layers and their effect on mixing is an important theme in Chapters 2 and 3.

1.4   Research Orientation

When linear quasigeostrophic stability analysis was first applied to geophysical fluid dynamics, it represented perhaps the only route to understanding eddy behavior in the ocean and led to great insights. Since then, two developments have open new methods of inquiry: (1) the advent of satellite observations, which permit a synoptic scale view of ocean eddies and their statistics, at least at the sea surface, and (2) great advances in numerical modeling, enabling very detailed simulation of eddy behavior. We take advantage of both of these developments in this thesis.

The first two chapters are primarily concerned with diagnosing mixing rates using tracer-based methods. Chapter 2, *Enhancement of Mesoscale Eddy Stirring at Steering Levels in the Southern Ocean*, makes use of the Southern Ocean State Estimate (Mazloff et al., 2009), a sophisticated, high-resolution numerical model that has been constrained by a wide range of observational data. We use the velocity field from the state estimate to simulate the evolution of passive tracers, and analyze the resulting tracer patterns to infer mixing rates. A key advantage gained by using this model is that it provides velocities at every depth, permitting us to study how mixing varies with both latitude *and depth*. The resulting mixing rates are interpreted in terms of wave propagation and mean flow speed. We also apply the mixing diagnostics to infer eddy-induced velocities.

Chapter 3, *Global Eddy Mixing Rates Inferred from Satellite Altimetry*, seeks to quantify the global geography of mesoscale eddy mixing. Because the source for the

velocity fields is from satellite data, the study is limited to the surface flow. Also, because of the complex geometry of the flow outside of the Southern Ocean, new diagnostic methods are explored which are better suited to the problem. The results, derived from over 20 years of global observations, indicate intense mixing in the tropics and western-boundary-current regions, with mean flows acting to both enhance and suppress mixing rates depending on the region. Using this global map of mixing, we estimate the eddy stress due to the eddy QGPV flux and find magnitudes comparable to the wind stress in large regions of the ocean.

In Chapter 4, *The Dependence of Southern Ocean Meridional Overturning on Wind Stress*, we examine the role of eddies in more idealized context. We construct a high-resolution, eddy-resolving numerical model of a Southern-Ocean-like domain with simplified forcing and bathymetry and investigate the response of the residual overturning circulation to changes in wind forcing. This problem is intimately tied to eddy mixing because of the central role of the eddy-induced overturning Ψ^*. The mixing rates are themselves related to the wind via the energy budget, enabling a closed theory for the overturning sensitivity to be constructed. The behavior of the model illustrates the importance of correctly capturing the physics of eddy mixing rates for large-scale climate problems.

The chapters of the thesis do not represent the chronological order in which the research was performed; rather, the topics have been grouped thematically. Chapters 2 and 4 have both already been published in the Journal of Physical Oceanography; the material in Chapter 2 in Abernathey et al. (2010) and the material in Chapter 4 in Abernathey et al. (2011). Chapter 3 contains the most recent results and has not been published.

Chapter 2

Enhancement of Mesoscale Eddy Stirring at Steering Levels in the Southern Ocean

2.1 Introduction

The Southern Ocean is a place of both strong eddy activity and strong mean flows. On one hand, we expect vigorous eddies to be very efficient at mixing tracers. On the other hand, the strong jets common in geophysical fluid flows can inhibit transport across their axes. In fact, spatially inhomogeneous mixing and the jet-formation mechanism appear to be fundamentally linked through potential-vorticity dynamics (Haynes et al., 2007; Dritschel and McIntyre, 2008). Furthermore, baroclinic currents can have different transport properties at different vertical levels. These vertical variations in eddy mixing in the troposphere and stratosphere have been investigated by Haynes and Shuckburgh (2000a,b), and also recently in more idealized models of baroclinic jets by, for instance, Greenslade and Haynes (2008); Esler (2008b,a). In an ocean context, Bower et al. (1985) suggested the Gulf Stream acts as a transport barrier near the surface but mixes strongly across the front at depth. This observation was followed by numerous Lagrangian studies that confirmed the general picture.

(Bower and Rossby, 1989; Bower, 1991; Rogerson et al., 1999; Yuan et al., 2002). Here we investigate the meridional and vertical variations of mesoscale eddy mixing in the Southern Ocean using a tracer-based approach.

Our work builds on the paper of Marshall et al. (2006, henceforth MSJH), who drove an advection-diffusion model with surface velocities computed from satellite altimetry. In their study, an initial tracer distribution with a prescribed monotonic gradient across the Antarctic Circumpolar Current (ACC) was stirred and mixed by the two-dimensional eddying flow. The theoretical framework set out by Nakamura (1996) was then applied to the tracer distribution. The resulting "effective diffusivity," K_{eff}, characterizes the rate of mixing by eddies acting laterally at the sea surface. An interesting meridional structure emerged, with enhanced mixing rates ($\sim$2000 m^2 s^{-1}) on the equatorial flank and evidence of suppressed mixing ($\sim$500 m^2 s^{-1}) near the core of the ACC. This result was consistent with the notion that the mean flow was acting to suppress mixing.

Smith and Marshall (2009, henceforth SM), echoing earlier work by Treguier (1999), suggested that although K_{eff} is small in the core of the ACC at the sea surface, it might be expected to be enhanced near the depth of the steering level of baroclinic waves growing on the thermal wind shear of the ACC. Employing a linear quasi-geostrophic stability analysis of a hydrographic climatology of the Southern Ocean, SM showed that the steering level of the fastest growing unstable modes resides at a depth of order 1.5 km and is roughly coincident with the level at which the meridional quasi-geostrophic potential vorticity (QGPV) gradient changes sign. Linear theory (Green, 1970; Marshall, 1981; Killworth, 1997) suggests that the eddy diffusivity of a growing baroclinic wave has a maximum at the steering level. Moreover, in calculations with a non-linear stacked QG model, SM confirmed that this linear result survives in the nonlinear regime. They also presented observational evidence that the phase speed of surface altimetric signals, the surface signature of interior baroclinic instability, propagate downstream at roughly 2 cm s^{-1}, the speed of the mean current at a depth of 1.5 km or so, and much slower than the 10 cm s^{-1} mean surface current.

40

Here our goal is to map the meridional *and depth* structure of K_{eff} in the Southern Ocean using the effective-diffusivity methodology set out by Nakamura (1996). In the absence of observed three-dimensional velocity fields, we make use of an eddying numerical state-estimate of the Southern Ocean tightly constrained by observations, and we diagnose K_{eff} from the tracer distribution on isopycnal surfaces. The resulting effective-diffusivity cross sections support the notion of intensified mixing at depth and also reveal that deep mixing below the ACC connects with the heightened surface mixing found by MSJH on the equatorward flank. The structure of K_{eff} contains the signature of a critical layer, wherein the interplay between upstream-propagating waves and eastward mean flow determines where mixing is enhanced and suppressed.

Our paper is organized in the following way. Section 2 contains a description of the state estimate and the machinery used to calculate effective diffusivity. The results of the calculation and a discussion of the mixing patterns observed, along with some regional calculations, comprise Section 3. In Section 4, we discuss the relationship between the effective diffusivity and the mean potential vorticity field. We also use K_{eff} in conjunction with the potential vorticity field to infer the eddy-driven transport in the ACC region. A discussion of our findings and conclusions are given in Section 5.

2.2   Numerical Simulation of Tracer Transport

2.2.1   Southern Ocean State Estimate

This study takes advantage of a new, high-resolution ECCO[1] product called the Southern Ocean State Estimate (a.k.a. SOSE, Mazloff, 2008). Oceanic state estimation (described, for example, by Wunsch and Heimbach, 2006) rigorously synthesizes diverse observations in a dynamically consistent manner. This is accomplished through minimization of the misfit between the observations and a numerical model, in this case the MITgcm (Marshall et al., 1997a,b). The observations used to con-

---

[1]Estimating the Circulation and Climate of the Ocean. Information available online at http://www.ecco-group.org .

41

strain SOSE include Argo subsurface floats, satellite measurements of sea-surface temperature and sea-surface height, GRACE satellite data, in-situ data from CTD and XBT casts, and NCEP re-analysis atmospheric data. The model has resolution of 1/6 degree, permitting mesoscale eddies to form, and spans a two year period from 2005 through 2006. During this time-period, SOSE is found to be more consistent with the data than optimally interpolated global climalotogical data products such as NOAA's World Ocean Atlas (Stephens et al., 2001) or Gourestski and Kolterman (2004). We use the velocity fields from SOSE to model the evolution of a passive numerical tracer. We also use the mean hydrographic fields to describe the climatological state of the Southern Ocean and to compute potential vorticity. A snapshot of the surface velocity field, revealing SOSE's rich mesoscale structure, is shown in Fig. 2-1a.

2.2.2 Tracer Advection

We characterize the eddy mixing by studying the evolution of a tracer governed by an advection-diffusion equation. The eddies stir the tracer, lengthening its contours and thereby enhancing the effect of small-scale diffusion. Nakamura (1996) developed a method to quantify this process by formulating the tracer equation in terms of a quasi-Lagrangian tracer-area coordinate, in which all transport is diffusive, making it possible to diagnose an effective eddy diffusivity using only a snapshot of the tracer field. Here we use the form given by MSJH, in which the effective diffusivity is written as:

$$K_{eff} = \kappa \frac{L_{eq}^2}{L_{min}^2} \qquad (2.1)$$

where κ represents the small-scale diffusion that halts the cascade of tracer variance, L_{min} represents the length of an unstrained contour, and L_{eq}, the equivalent length, can be thought of as the length of the stretched contour. This equivalent length can be computed from an instantaneous snapshot of the tracer field as

$$L_{eq}^2 = \frac{\frac{\partial}{\partial A} \int |\nabla q|^2 dA}{(\frac{\partial q}{\partial A})^2} \; . \qquad (2.2)$$

We have included this expression for completeness, but we refer the reader to the Appendix of MSJH for its derivation.

The effective diffusivity formalism is rigorously defined for advection-diffusion of a tracer in two dimensions. However, we wish to obtain information about the vertical and meridional distribution of K_{eff}. We therefore first employ the SOSE eddying velocity fields $\mathbf{v} = (u, v, w)$ to advect a passive tracer q according to the 3D advection-diffusion equation

$$\frac{\partial q}{\partial t} + \mathbf{v} \cdot \nabla q = \kappa_h \nabla_h^2 q + k_v \frac{\partial^2 q}{\partial z^2} \tag{2.3}$$

where κ_h and k_v are the horizontal and vertical diffusion coefficients and ∇_h^2 is the horizontal Laplacian. In a second step, the tracer field is then mapped onto two-dimensional neutral surfaces in the interior and K_{eff} evaluated from (2.1) using an appropriate choice of κ_h, as described below.

Following MSJH, we chose an initial tracer distribution approximately aligned with the streamlines of the ACC. As in Karsten and Marshall (2002a), a single streamline of the time-mean vertically-integrated-transport streamfunction was chosen from the core of the ACC. This was used as a reference to initialize tracer concentrations ranging from 0 to 1 along lines running parallel to this reference contour, as shown in Fig. 2-1b. The same initial concentration was used on each vertical level. This choice leads to a rapid equilibration of the L_{eq} tracer contours, but any initial tracer gradient roughly perpendicular to the ACC would result in a reliable calculation. (This was confirmed by repeating our calculations with the initial tracer contours simply aligned with latitude circles; the resulting L_{eq} was not significantly different from the results presented here.) We also employ the contours of this initial tracer field to define an approximate "streamwise average."

We performed the tracer advection on the same numerical grid as the original SOSE model, using the offline capability of the MITgcm. With grid points every 1/6th of a degree, the maximum grid spacing was approximately 18 km. Several experiments were carried out in which κ_h was set to, respectively, 50, 100, 200, and 400 m^2 s^{-1}. In all cases the vertical diffusion is set to $\kappa_v = 1 \times 10^{-5}$ m^2 s^{-1}, roughly
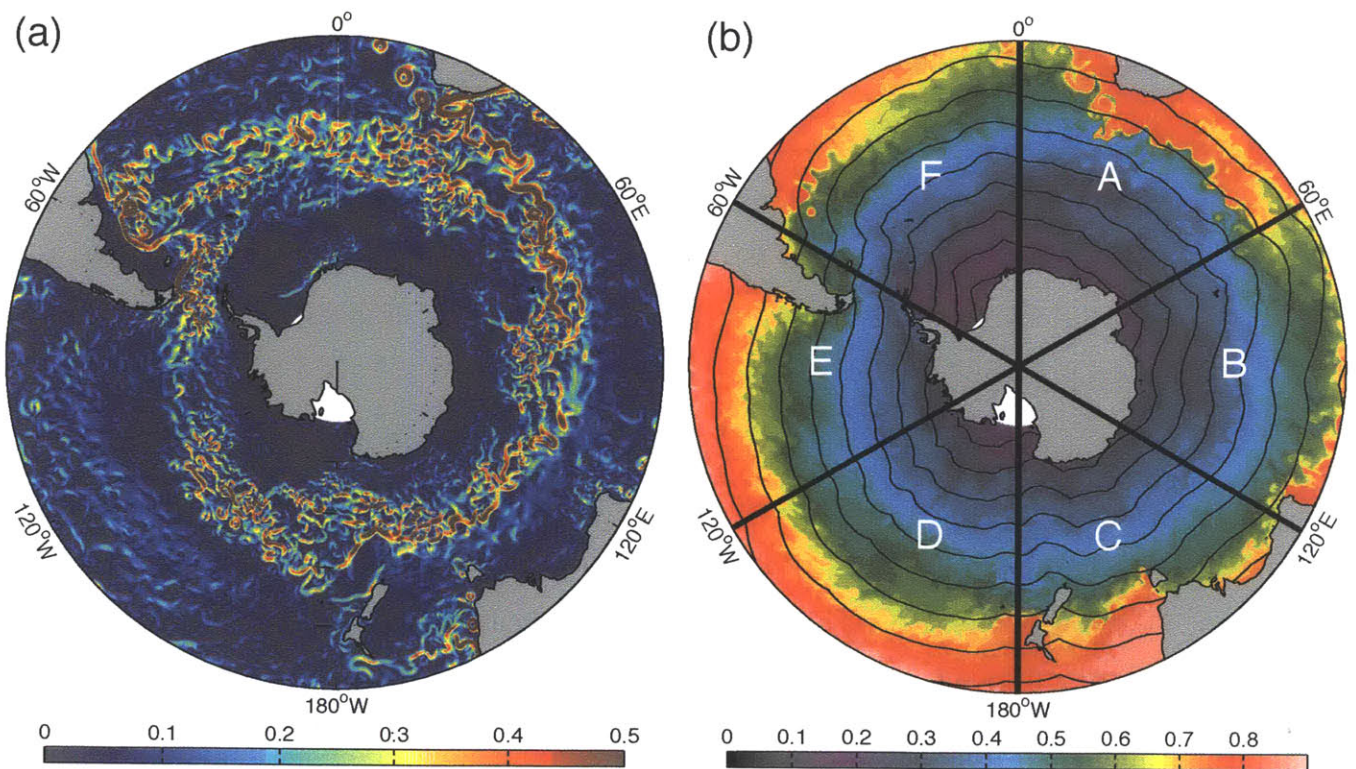
Figure 2-1: (a) Snapshot of surface current speed from SOSE. The color scale ranges from 0 to 0.5 m s^{-1}. (b) Tracer concentration after one year of advection-diffusion using $\kappa_h = 50$ m^2 s^{-1}. The black contours show the initial tracer distribution, which was also used to define a meridional coordinate for pseudo-streamwise averaging. The six sectors highlighted indicate the different regions for the regional effective diffusivity calculations.

consistent with observed diapycnal mixing rates in the thermocline.

The role of diffusive processes inherent in the numerical implementation, together with the overall impact of horizontal versus vertical diffusion, can be assessed by considering the globally-averaged tracer variance equation:

$$\frac{1}{2}\frac{\partial \langle q^2 \rangle}{\partial t} = -\kappa_h^{(num)} \langle |\nabla_h q|^2 \rangle - \kappa_v^{(num)} \langle q_z^2 \rangle , \qquad (2.4)$$

where $\langle \ \rangle$ indicates a volume-weighted average over the whole domain. Here $\kappa_h^{(num)}$ and $\kappa_v^{(num)}$ represent the diffusivities required to bring the observed decay in q^2 in to consistency with the above variance equation. For all values of κ_h in our experiments, the vertical term was at least an order of magnitude smaller than the horizontal, indicating that horizontal diffusion, rather than vertical, is responsible for dissipating tracer variance at small scales. More detailed analysis of the variance equation indicates that, for values of κ_h below 200 m^2 s^{-1}, implicit numerical diffusion augments the explicit value of κ_h by up to 60%, a finding consistent with incomplete resolution of the Batchelor scale. In particular, using $\kappa_h = 50$ m^2 s^{-1} gave $\kappa_h^{(num)} = 83$ m^2 s^{-1} while $\kappa_h = 100$ m^2 s^{-1} gave $\kappa_h^{(num)} = 128$ m^2 s^{-1}. In these cases, we use the estimated numerical value of κ_h in calculating K_{eff}. Higher values of κ_h did not generate significant spurious diffusion.

Before calculating K_{eff}, we allowed the tracer to evolve for one year. A sample tracer field after one year of stirring using $\kappa_h = 50$ m^2 s^{-1} is shown in Fig. 2-1b. Visual inspection reveals plausible tracer patterns and no evidence of grid-scale aliasing, despite the rather low value of diffusivity employed. Such levels of explicit diffusivity were also found to be appropriate in the study of MSJH, where altimetric fields were used to drive the tracer evolution rather than, as here, model fields constrained by observations.

2.2.3   Isopycnal Projection

The effect of mesoscale eddies acting in the "surface diabatic layer", where isopycnals outcrop, differs fundamentally from their role in the adiabatic interior of the ocean

45

(Held and Schneider, 1999; Kuo et al., 2005). In the surface layer, eddies transport buoyancy horizontally across isopycnals. In the interior, eddies stir primarily along tilted neutral surfaces, mixing potential vorticity and other tracers isopycnally. Here we attempt to characterize these two regions separately, diagnosing a horizontal K_{eff} near the sea surface and an isopycnal $K_{eff}^{(i)}$ in the interior.

An individual effective diffusivity calculation requires a two-dimensional tracer field: a slice taken at constant depth for K_{eff}, or a slice at constant neutral density for $K_{eff}^{(i)}$. Cross-sections can be built by stacking the results from many such slices, as described, for example, in Nakamura and Ma (1997) and Haynes and Shuck-burgh (2000a), who used isentropic surfaces in the atmosphere, or Cerovecki et al. (2009), who employed the same neutral-surface-projection technique described here. Constant-depth tracer fields, for computing K_{eff} are trivial to extract from the model output, since it uses depth coordinates intrinsically. The neutral-surface projection for $K_{eff}^{(i)}$ requires more care. We first calculated neutral density γ^n from the instantaneous SOSE temperature and salinity fields using the algorithm of Jackett and McDougall (1997). We chose 35 discrete values of γ^n to define a new density-based vertical coordinate. The tracer profile at each point was then interpolated onto these values of γ^n and the resulting two-dimensional tracer surfaces analyzed to determine $K_{eff}^{(i)}$, as described in the next section.

2.3 Cross-Sections of Effective Diffusivity in the Meridional Plane

Both the theoretical framework for deriving K_{eff} in terms of the modified-Lagrangian-mean tracer equation and the numerical technique for its computation are well documented (Nakamura, 1996; Nakamura and Ma, 1997; Shuckburgh and Haynes, 2003, MSJH) and so are not repeated here. We calculated L_{eq}^2 as defined in (2.2) using a MATLAB code. L_{eq}^2 was calculated on both horizontal and isopycnal tracer surfaces from simulations using κ_h values of 50, 100, 200, and 400 m^2 s^{-1}, yielding a total of

eight cross-sections. To calculate L_{min}^2, the minimum possible length of a tracer contour was inferred by performing an experiment using $\kappa_h = 4 \times 10^4$ m^2 s^{-1}. This very large value of diffusivity decreases the Péclet number to the extent that explicit diffusion rather than advection dominates the tracer evolution. MSJH showed that in this regime, the resulting contour lengths, again calculated from (2.2), tend to L_{min}. K_{eff} was then computed from (2.1). As described earlier, the level of mixing experienced by the numerical tracer, $\kappa_h^{(num)}$, was diagnosed from the tracer variance equation. A cutoff minimum was imposed on L_{min} of 10,000 km, chosen to prevent small values of L_{min} (caused by the surface outcropping of isopycnals or by the intersection of topography) from unrealistically inflating K_{eff}.

Both L_{eq} and L_{min} are defined as functions of the area A enclosed by a tracer contour. A mapping exists between A and an equivalent latitude ϕ_e. In the atmosphere, in the absence of topography, this mapping simply identifies the latitude circle which encloses the given area. But here we must account for basin geometry as well as isopycnal outcrops. We can define the area enclosed by a latitude circle ϕ_e on a neutral surface γ^n as

$$A_{\gamma^n}(\phi_e) = \int \int_{90°S}^{\phi_e} g(\lambda, \phi) dA \qquad (2.5)$$

where $g(\lambda, \phi) = 0$ for all locations not in the water, i.e. inside topography or beyond isopycnal outcrops, and $g = 1$ otherwise. We evaluated this expression numerically in the SOSE domain and used it to map L_{eq} and L_{min} to positions in latitude.

2.3.1 Global Cross-Section

The results of our calculations for different values of κ_h are shown as meridional cross-sections in Fig. 2-2. (The isopycnal calculations were mapped back to depth coordinates using the average depth of the neutral surfaces at each latitude.) The horizontal and isopycnal diffusivities share certain characteristics. Each panel in Fig. 2-2 indicates a region of intense mixing deep beneath the ACC (centered around 54° S) which becomes shallower moving equatorward. The greatest differences between them occur, unsurprisingly, near the surface. The horizontal diffusivities tend to intensify

47

near the surface, at least equatorward of the ACC region, while the isopycnal diffusivities uniformly decrease at depths shallower than 200 m because the sea surface acts to suppress isopycnal stirring on tilted neutral surfaces. The high horizontal effective diffusivities close to the bottom are not the result of enhanced stirring increasing L_{eq}, but rather result from the intrusion of topography, which causes small values of L_{min} to inflate K_{eff}. The isopycnal projections do not suffer from this problem, and these will be our primary focus.

From Fig. 2-2, we see that increasing the value of κ_h blurs the structure of K_{eff} somewhat. Indeed, visual inspection of the tracer fields reveals that (not surprisingly) they become increasingly smooth and less complex as κ_h is increased. Fig. 2-3 plots horizontal K_{eff} at the base of the mixed layer for various choices of κ_h, along with the K_{eff} profile obtained by MSJH directly using altimetry. We clearly see that the distributions of K_{eff} obtained here using $\kappa_h = 50$ and 100 m^2 s^{-1} are very close to those of MSJH, while those obtained using larger values if κ_h are considerably greater in magnitude. Since either of the lower values produces a result consistent with the earlier study, we choose to analyze the $\kappa_h = 100$ m^2 s^{-1} case, because the numerical diffusion ($\kappa_h^{(num)}$, diagnosed in the previous section) is smaller in proportion to the explicit diffusion. This choice is also supported on consideration of the (Pe, Nu) plot presented in MSJH, where Pe is the Péclet number and $Nu = K_{eff}/\kappa_h$ is the Nusselt number. For sufficiently large Pe, (i.e. sufficiently small κ_h) the slope of the line in (Pe, Nu) space is order unity, in which case K_{eff} becomes independent of the small scale value of κ_h (MSJH, Shuckburgh and Haynes, 2003). This decreasing sensitivity can be clearly seen in Fig. 2-2 as κ_h is reduced.

Since K_{eff}, the horizontal diffusivity, applies more readily to eddy buoyancy fluxes in the surface diabatic layer, while $K_{eff}^{(i)}$ is more appropriate for isopycnal mixing in the interior, in Fig. 2-4 we present a composite of these two quantities. We have chosen to separate the regions at 100m depth, a typical mixed-layer depth for this region.[2] Contours of the streamwise-averaged zonal velocity are also shown in Fig. 2-4,

---

[2]The mixed-layer depth (MLD) provides a reasonable estimate of the actual depth of the surface diabatic layer, since mixed-layer waters are subject to convection and thereby exposed to diabatic forcing near the surface. Dong et al. (2008) recently performed a detailed diagnosis of the MLD in
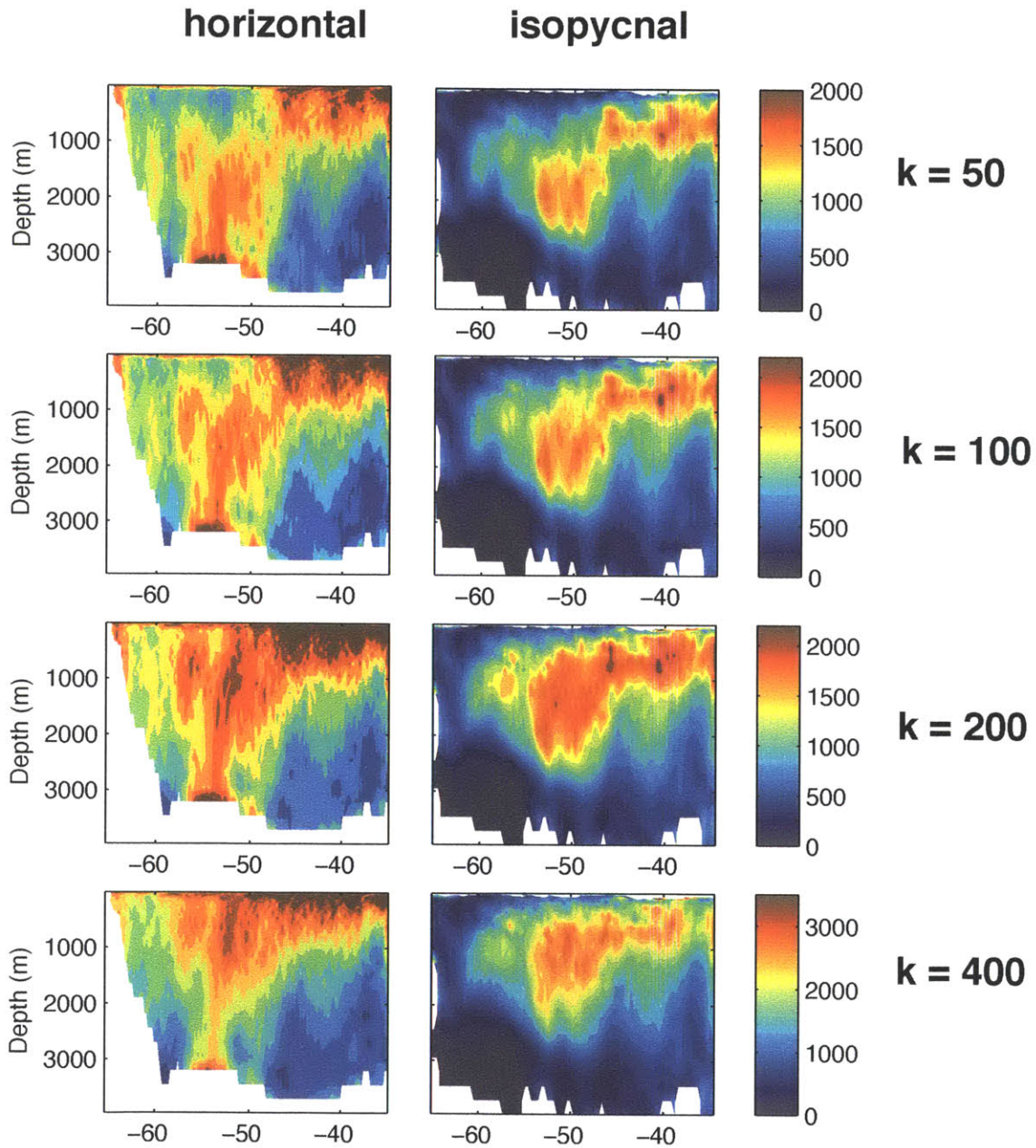
Figure 2-2: Comparison of different effective diffusivity calculations. The "horizontal" diffusivities were computed on surfaces of constant height and the isopycnal diffusivities on surfaces of constant neutral density. The same color scale, in m^2 s^{-1} is used for each value of κ_h indicated at right, also in m^2 s^{-1}. Note that the color scaling changes significantly for $\kappa_h = 400$.
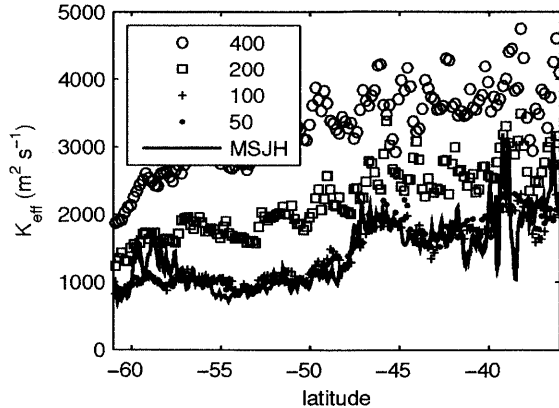
Figure 2-3: Comparison of effective diffusivity values with those found by MSJH. The markers show horizontal K_{eff} at 100 m depth, roughly at the base of the mixed layer, from our experiments with $\kappa_h = 400, 200, 100$, and 50 m^2 s^{-1}. The solid line is K_{eff} from MSJH.

indicating the mean position of the ACC. Although the time- and spatial average blurs the fine structure and multiple jets of the current, a strong mean flow is still apparent. A striking feature is that, in both the surface layer and the interior, effective diffusivity is significantly reduced where the mean flow is strongest. Mixing is enhanced between the 2 and 4 cm s^{-1} contours, particularly on the equatorward side of the jet: the surface of maximum K_{eff} is at a depth of order 1500 m beneath the core of the ACC and shoals on the equatorial flank.

SM anticipated this general form for K_{eff}, drawing on insights from linear baroclinic instability theory. In the analysis of a growing baroclinic disturbance (see, for example Green, 1970; Marshall, 1981; Killworth, 1997), the diffusivity of quasigeostrophic potential vorticity takes the form

$$K_q = \frac{c_i}{k} \frac{\frac{1}{2}v'^2}{(U - c_r)^2} \tag{2.6}$$

where U is the mean zonal current, c_r is the real part of the phase speed, c_i is the imaginary part (the growth rate), k is the zonal wavenumber, and $\frac{1}{2}v'^2$ is the eddy

the Southern Ocean from ARGO data. They found substantial spatial and seasonal MLD variability, with MLDs reaching over 400 m in the winter just north of the Subantarctic Front.

50
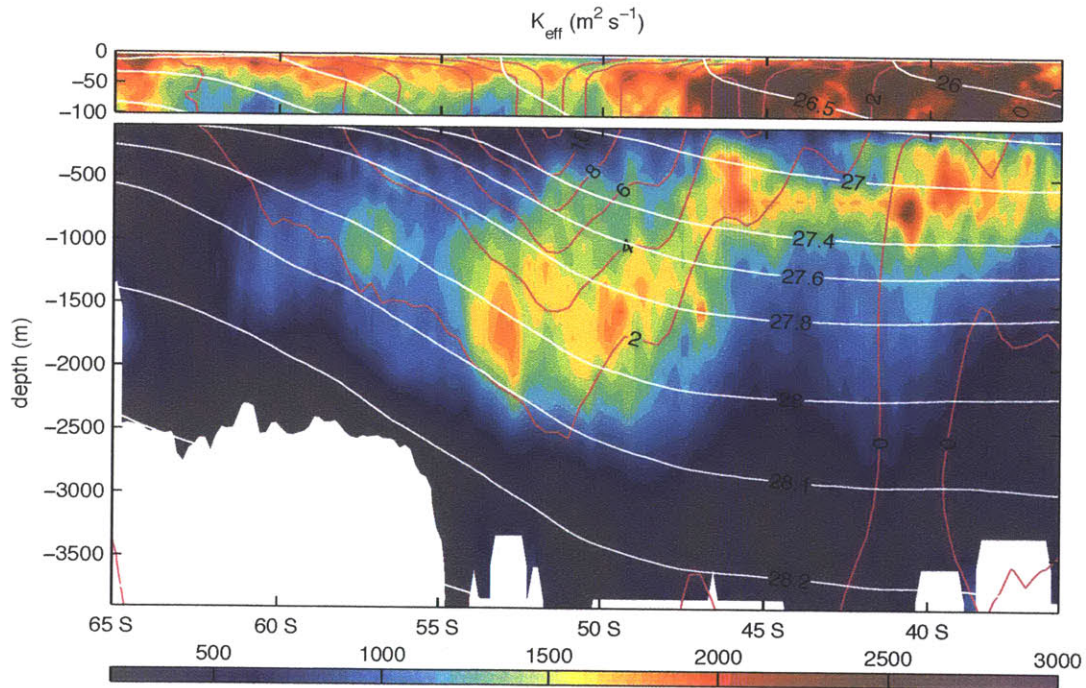
Figure 2-4: Effective diffusivity K_{eff} in m^2 s^{-1}. The upper panel shows horizontal effective diffusivity in the upper 100 m. In this region the diffusivity can be interpreted as a horizontal eddy mixing in the mixed layer. The lower panel shows *isopycnal* effective diffusivity, which characterizes the mixing of passive tracers such as potential vorticity in the ocean interior. The magenta contour lines show the streamwise-averaged zonal velocity, indicating the position of the mean jet of the ACC, and mean isopycnals appear in white. The velocity contour interval is 2 cm s.$^{-1}$.

kinetic energy. At finite amplitude, the general dependence of the diffusivity on the eddy kinetic energy, the phase speed, and the mean flow can be expected to hold, since the form of the diffusivity is related to the kinematics of particle displacement. SM noted that the observed zonal propagation speed of altimetric signals in the ACC was roughly 2 cm s^{-1}, significantly smaller than mean surface zonal currents, typically 10 cm s^{-1} (shown, for example, in Fig. 2-4). At depth, however, where mean flow advection and wave propagation speeds are much more closely in sync, the wave can "keep up" with the mean flow and achieve large meridional excursions of fluid parcels, promoting mixing. SM followed up these linear arguments with detailed, fully turbulent calculations with a stacked quasi-geogstrophic model, which was relaxed back to observed hydrography on the large scale. They confirmed that intensified mixing of potential vorticity occurred at depth, near the steering level predicted by linear theory where $U = c$. The depth where $U = c$ is also frequently referred to as a "critical level" or "critical layer" (Bretherton, 1966; Boss and Thompson, 1999). The findings reported here, which make use a much more realistic eddying model constrained to be close to observations, support the idea that critical-layer enhancement occurs in the region of the ACC. The numerical studies of Treguier (1999) and Cerovecki et al. (2009) also provide clear evidence of intensified mixing in the critical layer of a baroclinically unstable jet. Treguier (1999) in particular diagnoses mixing coefficients based on flux-gradient inversions of both quasi-geostrophic potential vorticity in the horizontal and Ertel potential vorticity along isopycnals. The resulting vertical diffusivity profile (her Fig. 9) is remarkably similar to our vertical profile of $K_{eff}^{(i)}$ in the jet axis, reaching a peak of 1600 m^2 s^{-1} at 1500 m depth.

If steering-level effects are responsible for the enhanced diffusivity at depth, we might expect to observe eddies propagating eastward at a speed slower than the surface mean flow in SOSE. The phase speeds can be calculated using Radon transforms, as done in SM, but here we opt for the simpler approach of constructing Hovmöller diagrams. We examined the SOSE sea-surface height anomaly in a sector in the Pacific between 165° W and 135° W. Fig. 2-5 shows two Hovmöller diagrams, one at 53° S, near the mean zonal flow maximum in this region, and one at 47° S. It is encouraging

to see that $c \simeq 2$ cm s^{-1} in the ACC, since this places the steering level around 2000 m deep, in agreement with the structure of K_{eff} in Fig. 2-4. North of the jet at 47° S, the anomalies propagate westward at approximately 1 cm s^{-1}. These numbers are in agreement with those of SM.
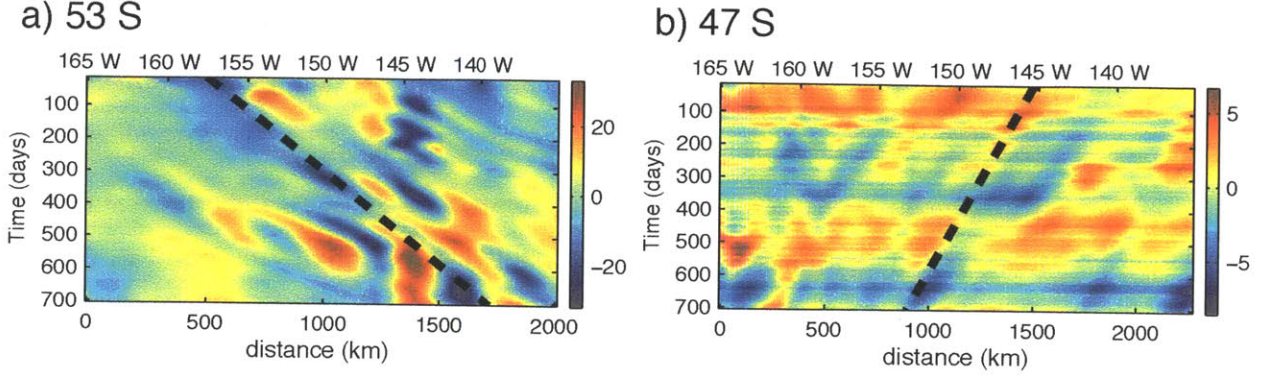
Figure 2-5: Hovmöller diagrams of SOSE sea surface height anomaly (in cm) in the Pacific. (a) At 53° S, a latitude where the ACC is strong in this sector, the anomalies appear to propagate east, downstream. The dotted black line in this figure denotes an eastward phase speed of 2 cm s^{-1}. (b) At 47° S, north of the the ACC, the anomalies propagate west, as expected of Rossby waves in the absence of a strong mean zonal flow. The dotted line here indicates a westward phase speed of 1 cm s^{-1}. Note that the anomalies in the northern region are much weaker than those in the ACC, and consequently, variability on short time scales is visible in (b) that is not noticeable in (a) due to the difference in color scales.

2.3.2   Regional Cross-Sections

While the global cross-section of effective diffusivity seems to offer a picture consistent with the global streamwise-average mean fields, the Southern Ocean contains large zonal asymmetries in bathymetry, circulation, and eddy activity. To address the zonal variations in mixing, we split the domain into six sectors and repeated the calculation on each sector. Shuckburgh et al. (2009b) have shown how this procedure, while not formally permitted in Nakamura's construction, still gives meaningful values of K_{eff} in the truncated domain. The cross sections of the isopycnal diffusivity $(K_{eff}^{(i)})$ are shown in Fig. 2-6, along with zonally-averaged zonal velocity and isopycnals. Again we imposed a minimum on L_{min}, requiring $L_{min} > 2200$ km in each sector. Where

53

L_{min} does not meet this criteria, no value is plotted in Fig. 2-6, leading to the irregular white patches near the surface and bottom. Outcropping isopycnals or the intersection of neutral surfaces with bottom topography can lead to very small values of L_{min}, but this effect does not truly reflect an enhanced effective diffusivity. The cutoff procedure focuses attention on variations in K_{eff} due to variation in L_{eq}.

Intensified mixing at depth is clearly present on the flanks of the jet maxima in most sectors, the location in latitude varying with the local flow. Other regions of enhanced mixing in each sector can also be related to the local current system. In particular, as noted by Shuckburgh et al. (2009b), strong mixing is found in regions where eddies are generated in association with topographic features in regions of weak zonal mean flow. In Fig. 2-6a, the region south of Africa between the Atlantic and Pacific, the mixing in the ACC is concentrated in a narrow region below and equatorward of the jet. Another surface-intensified mixing region appears north of 40° S. Movies of the tracer evolution suggest that this mixing is associated with the intense eddies of the Agulhas rings. The Indian Ocean sector, Fig. 2-6b, shows very strong mixing on both sides of the jet as well as below. This sector contains the Kerguelen Plateau, a large topographic feature that generates strong eddy activity as the flow passes over and around it. South of Australia, Fig. 2-6c, the only strong mixing occurs in a deep, narrow band between 1000 and 2000 m depth. Fig. 2-6d is the south-west Pacific, the region in which the Hovmöller diagrams of Fig. 2-5 were constructed. In agreement with our steering-level hypothesis, enhanced mixing at depth is observed at around 53° S below the jet where the zonal velocity is 2 cm s^{-1}. This sector also shows the clearest multiple-jet structure, both in the mean-flow field and in the bands of high and low K_{eff}. In Fig. 2-6e, the southeast Pacific, K_{eff} seems quite weak, consistent with the low eddy kinetic energy in this region and with the results of Shuckburgh et al. (2009b). However, it still shows intensification with depth. Finally, downstream of Drake Passage (Fig. 2-6f), intense mixing appears very widespread. It is likely that much of the mixing north of 45° S is the result of eddies spawned by the Falkland current. In general, the regional plots suggest that much of the strong mixing visible in Fig. 2-4 north of 45° S, where the mean flow is very
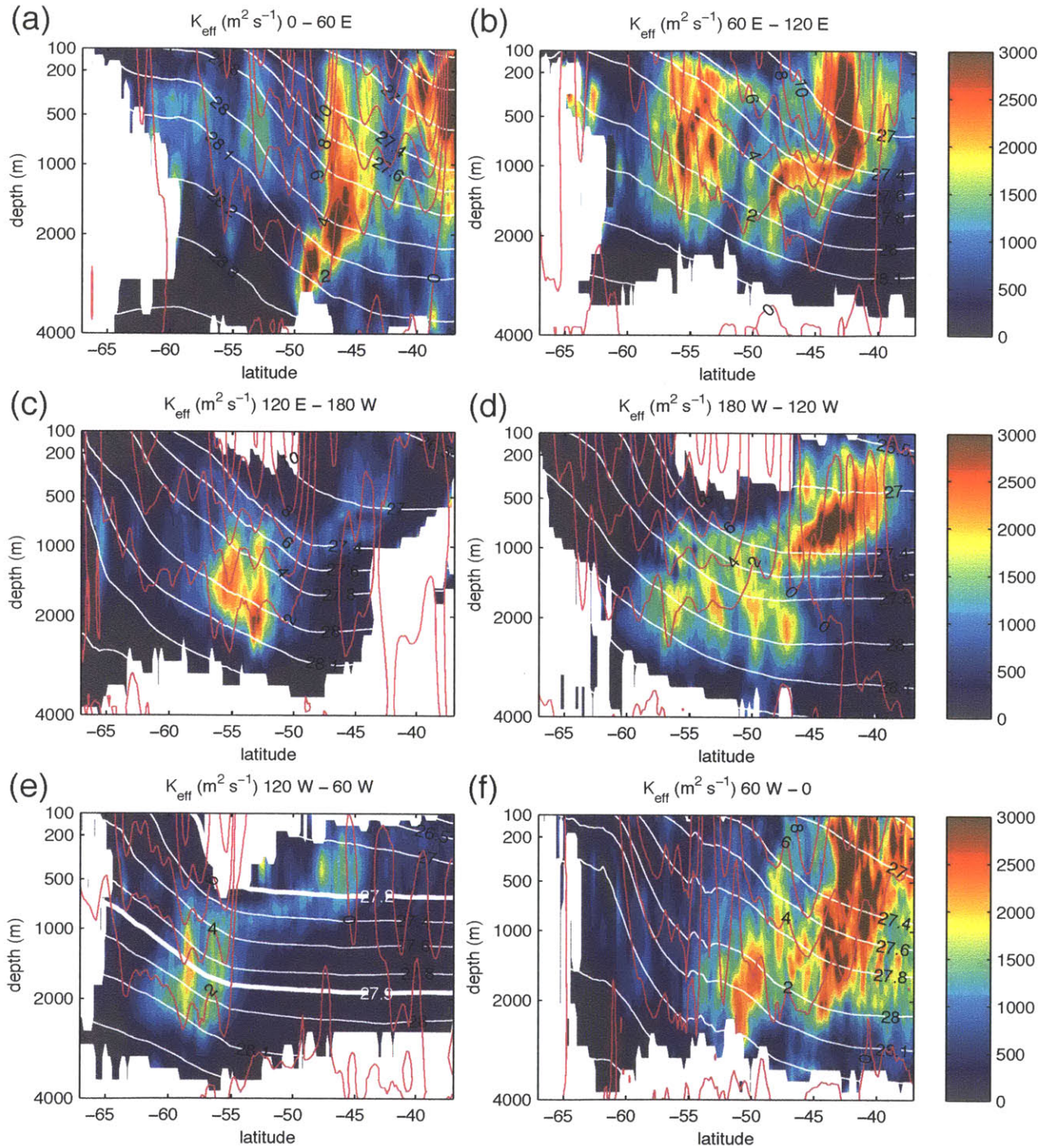
Figure 2-6: Regional cross-sections of isopycnal K_{eff}. The magenta contour lines show the zonally-averaged zonal flow, with a contour interval of 2 cm s^{-1}. The mean isopycnals appear in white. The sectors are (a) 0 - 60° E, (b) 60° E - 120° E, (c) 120° E to 180°, (d) 180° to 120° W, (e) 120° W to 60° W, and (f) 60° W to 0. The DIMES experiment will take place mostly in (e).

55

weak, is the result of interaction with the continents rather than frontal dynamics.

The Diapycnal and Isopycnal Mixing Experiment in the Southern Ocean (DIMES, Gille et al., 2007) is ongoing (2009 to 2012). The goal of the experiment is to measure mixing rates in the region upstream of the Drake Passage using RAFOS floats and a patch of chemical tracer. Our results predict that isopycnal mixing rates vary considerably with latitude and depth. In order to gain some insight into the locations of intensified mixing in the DIMES region, we can map the effective diffusivity *back* onto tracer contours from the tracer snapshot used in the K_{eff} calcuation, since $K_{eff} = K_{eff}(A) = K_{eff}(q)$. We have constructed such maps on the two DIMES target isopycnals, $\gamma^n = 27.2$ and $\gamma^n = 27.9$, and near the surface, in Fig. 2-7. (These isopycnals are also highlighted in Fig. 2-6e, the sector containing the DIMES region.) Satellite altimetric data is available to the DIMES investigators in real time during the deployment of floats and tracer. With this in mind, we have included contours of the instantaneous sea-surface height from SOSE in Fig. 2-7, which suggest the position of the ACC fronts. This presentation highlights the fact that isopycnal mixing on the deeper surface is strongest directly at the front, while on the shallower surface the mixing is weak right at the front, but stronger to the north.

2.4   Potential Vorticity Mixing

The meridional overturning circulation cannot be measured directly and must be inferred. One approach in the Southern Ocean, where eddies are suspected to contribute significantly to the meridional transport, has been to deduce the eddy mass transport by assuming the downgradient transfer of potential vorticity (PV) by eddies. For instance, Marshall et al. (1993), Speer et al. (2000), and Karsten and Marshall (2002a) have all employed some version of this technique. To use this approach, a diffusion coefficient of PV must be specified; in many cases, this coefficient is assumed to be constant. We have found, however, that isopycnal mixing is highly nonuniform in space. In this section we explore some of the consequences of spatial variations in effective diffusivity. Note that we do not attempt to directly diagnose the eddy PV

Figure 2-7: Maps of effective diffusivity in the region of the DIMES experiment. (a) Horizontal effective diffusivity at 100 m depth; isopycnal effective diffusivity on neutral surfaces (b) $\gamma^n = 27.2$ and (c) $\gamma^n = 27.9$. A snapshot of sea-surface height from SOSE from the same time is overlaid, with contour levels of 10 cm.

flux or flux-gradient relationships from SOSE because the computation of stable eddy statistics demands long timeseries (only 2 years are available from SOSE) and because the local fluxes are dominated by rotational components (Marshall and Shutts, 1981).

2.4.1   The Potential Vorticity Field

We diagnosed the potential vorticity distribution using the time-mean SOSE fields. The following form is computed appropriate to the large-scale:

$$P = f\frac{\partial b}{\partial z} \tag{2.7}$$

where b is the buoyancy and f the Coriolis parameter. The relative vorticity has been neglected because the Rossby number is small on the large scales. Using the same isopycnal transformation described in Section 2, we computed P and took its streamwise average in buoyancy space, i.e. following streamlines *and* isopycnals. The result is plotted, transformed back to depth coordinates, in Fig. 2-8a. We see that surfaces of constant b and surfaces of constant P align with one another over much of the domain, especially for isopycnals that do not outcrop. This is confirmed by the plot of the isopycnal gradient of P shown in Fig. 2-8b, which is small in much of the interior. Notably, PV gradients become very large near the surface in the southern ACC region, just where we observe reduced effective diffusivites. To examine this more closely, in Fig. 2-9 we plot the PV gradient along with $K_{eff}^{(i)}$ on several different isopycnals. We do indeed find consistently low values of $K_{eff}^{(i)}$ where PV gradients are low. The PV gradients are high in the core of the jet, consistent with the invertibility principle, and in this region the effective diffusivity is smaller. Where the PV gradient is very weak, no amount of mixing can lead to a PV flux. But there does appear to be a transition zone, where both $(\partial P/\partial y)_b$ and K_{eff} are nonzero. This suggests a nonzero eddy flux of PV.
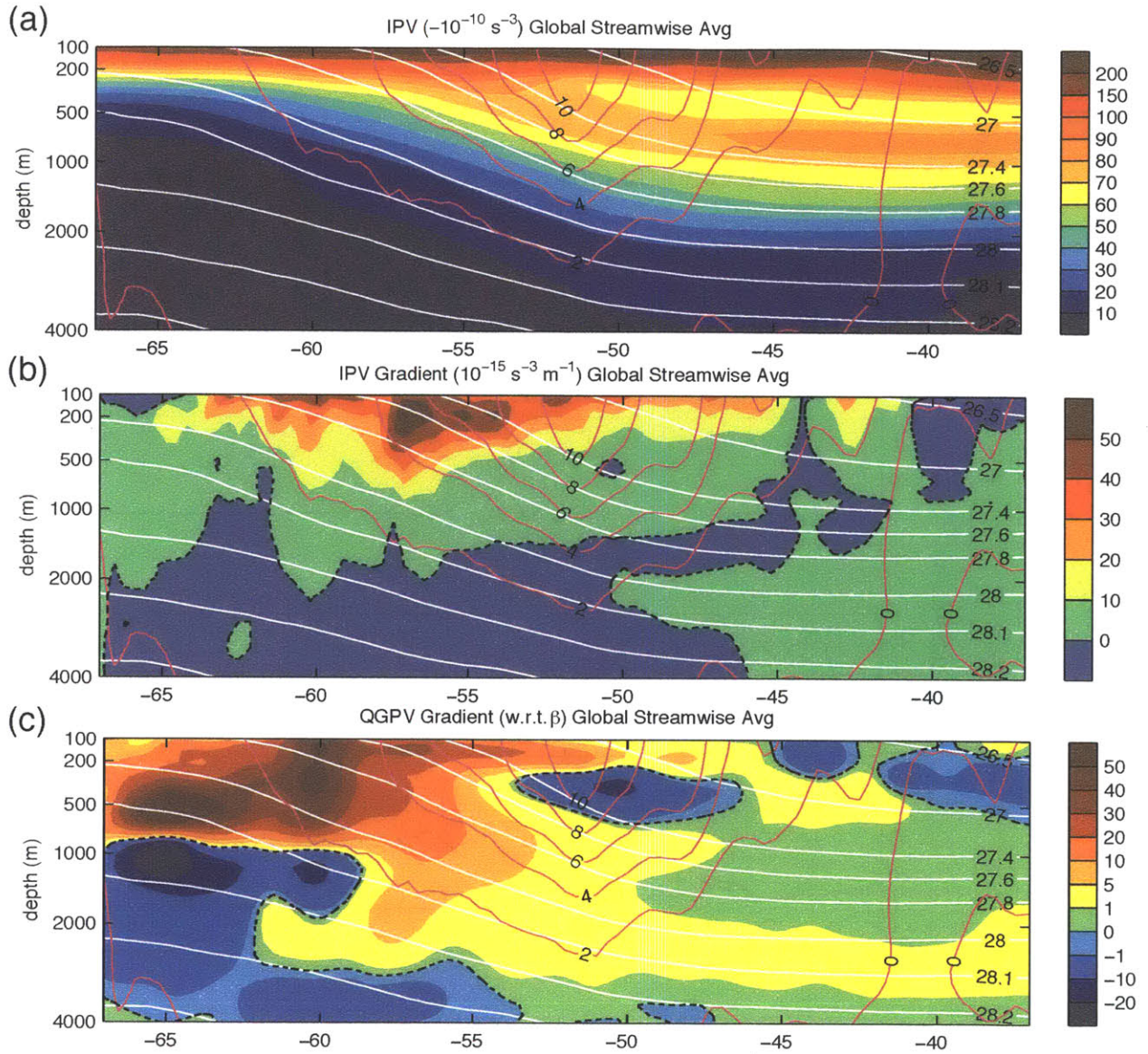
Figure 2-8: (a) Streamwise-averaged isentropic potential vorticity (IPV) as defined by (2.7). The units are -10^{10} s^{-3}. (The PV is everywhere negative, but we have reversed the sign for clarity.) The magenta contours (interval 2 cm s^{-1}) show the streamwise-averaged zonal flow, denoting the mean position of the ACC. (b) Streamwise-averaged isentropic potential vorticity gradient (IPVG), units $10^{-15} s^{-3} m^{-1}$. (c) Streamwise-averaged QGPV gradient, as defined by (2.12), normalized with respect to the mean value of β in the domain.

IPV Gradient (solid) vs. K_{eff} (dashed) on neutral surfaces
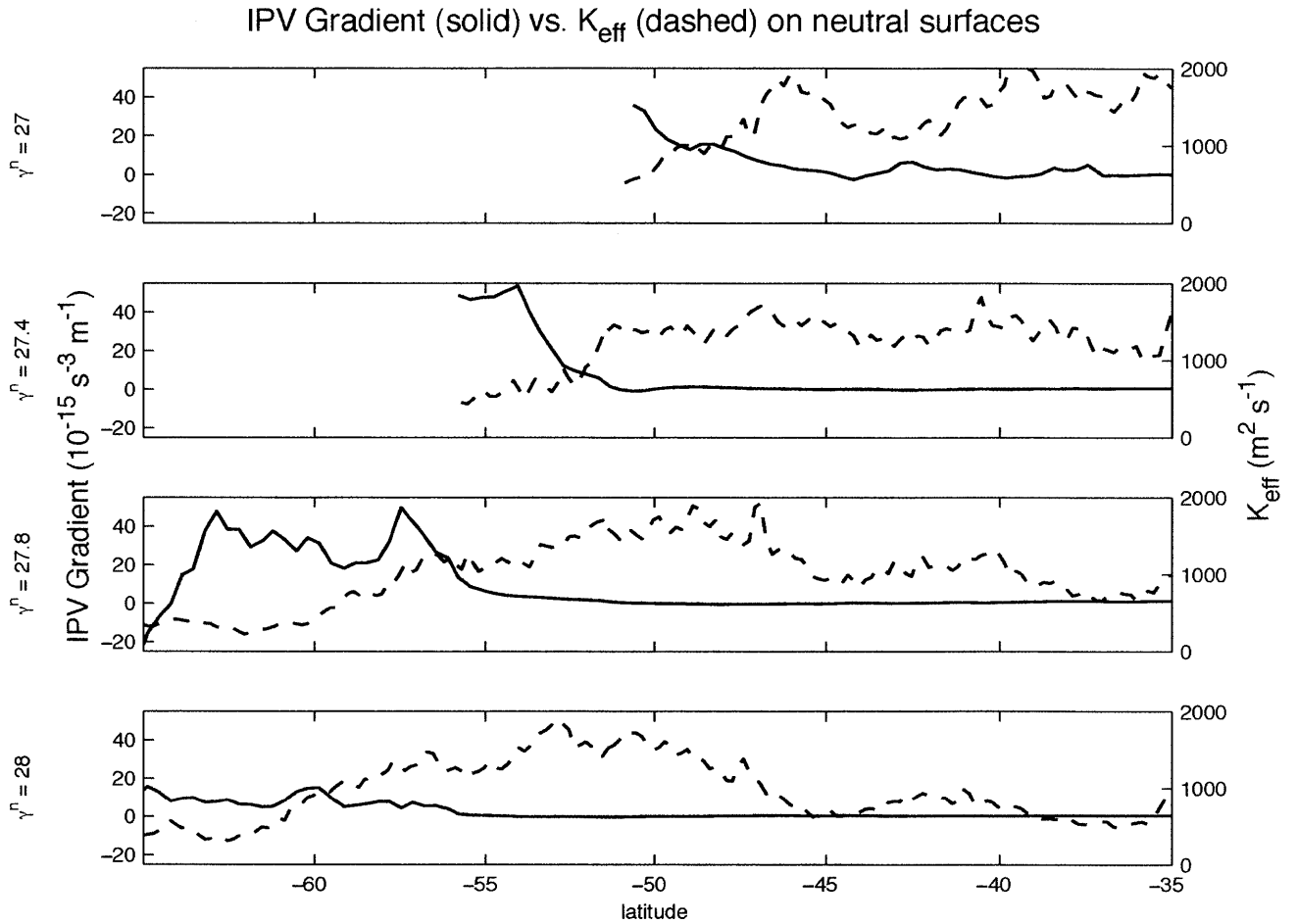
Figure 2-9: The effective isopycnal diffusivity ($K_{eff}^{(i)}$, solid lines) and the IPV gradient (dashed lines) on several different neutral surfaces. Only values where the mean isopycnal depth is greater than 100 m have been plotted. Weaker interior IPV gradients correspond with higher effective diffusivities and vice-versa.

2.4.2 Parameterized Eddy Forcing

We consider the streamwise- and time-average momentum balance of the large-scale flow through the Transformed Eulerian Mean (TEM) zonal momentum equation (see, e.g. Andrews et al. (1987); Ferreira et al. (2005))

$$- f v_{res} = - \frac{1}{\rho_0} \frac{\partial \overline{p}}{\partial x} + \overline{v'q'} + \frac{1}{\rho_0} \frac{\partial \overline{\tau}_x^w}{\partial x} \ , \qquad (2.8)$$

where v_{res} is the residual meridional velocity, a sum of eddy and mean contributions, $\overline{v'q'}$ is the zonal- or streamwise-average meridional eddy quasi-geostrophic potential vorticity (QGPV) flux, and τ_x^w is the wind stress. It is common to define an "eddy velocity" v^* as the ageostrophic part explicitly balanced by the PV flux:

$$- f v^* = \overline{v'q'} \ . \qquad (2.9)$$

The quantity v^* is often referred to as the bolus velocity, and is also related to the "gyroscopic pump" described by Dritschel and McIntyre (2008).

Following, for example, Green (1970); Rhines and Young (1982); Killworth (1997); Visbeck et al. (1997); Treguier et al. (1997), etc., we assume $\overline{v'q'}$ is transferred down the mean gradient $\overline{q}_y$ with our isopycnal effective diffusivity thus:

$$\overline{v'q'} = - K_{eff}^{(i)} \frac{\partial \overline{q}}{\partial y} \ . \qquad (2.10)$$

Note that the isopycnal effective diffusivity is used in Eq.(2.10) and is worthy of comment. As shown by Plumb and Ferrari (2005), in the limit that relative vorticity can be neglected, the *residual* meridional isentropic eddy flux of Ertel PV is proportional to the horizontal meridional eddy flux of QGPV. Indeed we note in passing that, under quasigeostrophic scaling, the meridional gradient of QGPV at constant z is equal to the meridional gradient of Ertel potential vorticity P along isopycnals: i.e.

$$\left(\frac{\partial q}{\partial y} \right)_z \simeq \frac{1}{N^2} \left(\frac{\partial P}{\partial y} \right)_b \ . \qquad (2.11)$$

61

We checked this relation in SOSE and found it to hold well everywhere outside of the mixed layer. Thus (2.8) and (2.10), written in height coordinates, are not as restrictive as they may seem: they are isomorphic, both mathematically and physically, to analogous expressions in isopycnal coordinates. Since our isopycnal effective diffusivities most closely describe the transport of a conserved tracer (like Ertel PV) along isopycnals, $K_{eff}^{(i)}$ is the more appropriate choice to capture the horizontal eddy mixing of QGPV.

The mean QGPV gradient was computed at each latitude. Neglecting the relative vorticity gradient, which is very small compared to the other terms, the gradient takes the form

$$\frac{\partial \overline{q}}{\partial y} = \frac{\partial}{\partial y} \left[f_0 + \beta y + \frac{\partial}{\partial z} \left(\frac{f_0}{N^2} \overline{b} \right) \right] = \beta - f_0 \frac{\partial s}{\partial z}, \qquad (2.12)$$

where $s = -\overline{b}_y / N^2$ is the mean isopycnal slope. We allow β and f_0 to take on local values at each latitude, assuming the scaling assumptions of QG theory to be locally valid, as in, for example, Smith (2007). Numerical implementation requires much differentiation and can lead to noise on the grid-scale which was removed using a Shapiro filter. The streamwise-averaged $\overline{q}_y$ is shown in Fig. 2-8c. Its general structure—the large positive gradient south of the ACC near the surface, and the locations of negative gradients—is similar to the IPV gradient, as expected.

We can use the parameterization of (2.10), along with (2.9) to estimate the eddy velocity v^*. We can then compare this estimate with one based on a constant diffusivity $K = 1000$ m^2 s^{-1}, similar to the conventional Gent-McWilliams parameterization. The results of such an estimate are shown in Fig. 2-10 at two different latitudes in the ACC. In general, the profiles show southward eddy transport above 1000 m and, in some cases, weaker northward transport at depths. This circulation is consistent with the effort by the eddies to flatten the sloping isopycnals, releasing potential energy. Below 1000 m depth, where the PV gradients are weaker and K_{eff} is relatively high, the two methods of estimating v^* yield very similar estimates. But at shallower depths, the constant-K parameterization produces a much greater estimate of the southward eddy transport in the density classes corresponding to upper-circumpolar

deep water ($27.5 < \gamma^n < 28.0$). From this we conclude that one potential consequence of the diminished mixing in the jet core is the suppression of the eddy component of the meridional overturning circulation.
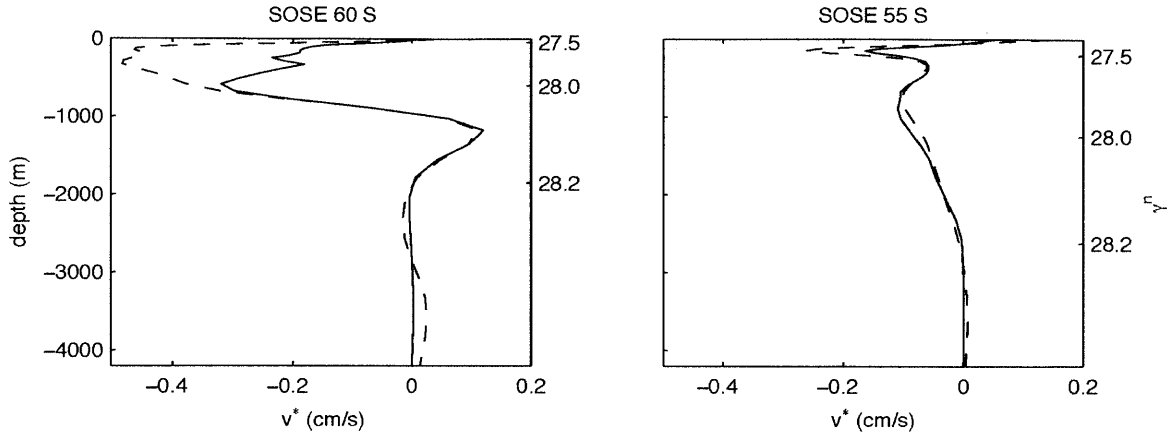
Figure 2-10: Estimated eddy-induced velocities, v^*, based on (2.9) and (2.10) at two different latitudes in the ACC derived from the SOSE mean fields. The solid lines indicate $K_{eff}^{(i)}$ was used as the QGPV diffusivity, while the dashed lines are for a constant diffusivity $K = 1000$ m^2 s^{-1}. Isopycnals depths for each profile are indicated on the right of each graph.

2.5 Discussion and Conclusions

This study has used a tracer-based approach, together with a model of the Southern Ocean constrained by observations, to quantify mesoscale eddy stirring in the Southern Ocean. The foremost result we wish to highlight is the presence of enhanced eddy effective diffusivity well below 1000 m depth in the Southern Ocean. Overall, a structure is observed of reduced eddy diffusivity at the core of the ACC, with enhanced values on its flanks and at depth where the zonal velocity is in the range of 2-4 cm s^{-1}. We suggest that this is strongly indicative of mixing at a critical layer. These findings are consistent with the quasi-geostrophic analysis of SM and the idealized models of Cerovecki et al. (2009) and Treguier (1999), with theoretical considerations based on the observed reversal of potential vorticity gradients and the steering level of linear baroclinic modes, and with basic kinematics. While we have focused on the

63

mixing of PV, it is important to keep in mind that the effective diffusivities diagnosed here apply to the mixing of any tracer, be it chemical or biological.

Shuckburgh et al. (2009a) and Sallée et al. (2008) noted that at the surface, assessments of eddy mixing based on particle dispersion do not indicate a minimum at the core of the ACC. Finite-time Lyapunov exponents, another possible measurement of eddy stirring, correlate closely with eddy kinetic energy but do not seem to be diminished by strong mean flow, reaching their highest values in the western boundary currents and ACC (Waugh and Abraham, 2008; Shuckburgh et al., 2009a,b). Similarly, particle-based results do not seem to indicate enhanced mixing below the ACC at depth (Griesel et al. 2009, manuscript in preparation). In light of the upcoming DIMES experiments, it is important to reconcile these view of eddy mixing. Some progress has been made on this front by d'Ovidio et al. (2009).

We argue that effective diffusivity is a useful metric because of the dynamically consistent relationship it holds with the IPV gradient. The strong IPV gradient in the core of the ACC acts as a barrier to wave propagation—baroclinically unstable waves propagating in the steering level on the edge of this gradient break, form closed eddies, and homogenize the low-PV region equatorward of the jet. This conceptual picture bears a close resemblance to the winter stratosphere, where high effective diffusivities in the "surf zone" outside the polar vortex are indicative of breaking planetary waves (Haynes and Shuckburgh, 2000a). However, several important distinctions complicate this interpretation. The size of mesoscale eddies in the Southern Ocean is far below the planetary scale. Indeed, the streamwise-averaged view necessarily obscures localized eddy processes such as interactions with particular topographical features (e.g. the Kerguelen plateau). This point is underscored by the wide variations seen in the effective-diffusivity patterns between sectors. Secondly, planetary waves in the stratosphere are generally thought to propagate up from the troposphere (McIntyre and Palmer, 1983), far below the critical layer they encounter in the stratosphere. There is no such spatial separation in the ACC. The eddies arise as a result of baroclinic instability and interact with the critical layer in the same region. Perhaps a better atmospheric analogy is the midlatitude troposphere, where intense mixing at

the steering level homogenizes PV and brings the mean state closer to neutrality. This processes has been studied in the context of baroclinic adjustment (Stone, 1978; Zurita-Gotor and Lindzen, 2004a,b). Another open question is the relationship between this large-scale mixing structure and the smaller-scale multiple jets of the ACC. Thompson (2009, manuscript submitted to *J. Phys. Oceangr.*) recently conducted an analysis of mixing and multiple-jet formation over topography with an eye to the ACC; he found regions of enhanced mixing between each of the small-scale jets. How these small-scale mixing patterns influence the large-scale is an important question for future investigation.

We have used effective diffusivity profiles to estimate eddy-induced meridional velocities by parameterizing the eddy QGPV flux. This produced a reasonable picture; the sense and magnitude of the circulation were consistent with other inferences and models. The parameterization using effective diffusivity was compared to a constant diffusivity assumption, as in the Gent-McWillams parameterization. We found the greatest differences to arise from the low values of K_{eff} in the ACC core and on its poleward flank, rather than from the high values of K_{eff} found near the steering level, where weak PV gradients dominate. While not quantitatively rigorous, these estimates show how the transport barrier in the core of the jet could potentially affect the strength of the meridional overturning circulation. We conclude that the consequences of the variations of the effective diffusivity for the large-scale overturning circulation merit further study.

Chapter 3

Global Eddy Mixing Rates Inferred from Satellite Altimetry

3.1   Introduction

A large amount of the ocean's kinetic energy resides at the mesoscale, a consequence of ubiquitous baroclinic instability in the large-scale density distribution(Gill et al., 1974; Ferrari and Wunsch, 2009). The advent of satellite altimetry permitted global mapping of surface eddy kinetic energy (EKE), whose spatial distribution is well correlated with local baroclinic instability (Stammer, 1998; Tulloch et al., 2009). The question of how to best use such observations to infer eddy mixing rates is a long-standing problem in physical oceanography.

A common approach has been to frame the problem in terms of "mixing length" from turbulence theory, which assumes the eddy diffusivity is given by $K = \alpha V_e L_{mix}$, where V_e is a characteristic eddy velocity, L_{mix} the mixing length and α a constant of proportionality (Prandtl, 1925). Determining these factors in geostrophic turbulence from purely theoretical arguments is a problem with a long history (Green, 1970; Stone, 1972; Larichev and Held, 1995; Held and Larichev, 1996; Visbeck et al., 1997; Thompson and Young, 2006, 2007). Estimating them from satellite data is a somewhat easier problem, but still challenging. Satellite observations directly yield the eddy velocity V_e in straightforward way; however, theoretical closures must be still

be employed to determine L_{mix} from observable properties.

The first such closure theory was by Holloway (1986), who assumed that $V_e L_{mix} \simeq g\overline{h'^2}^{1/2}/f$, where $\overline{h'^2}^{1/2}$ is the rms sea surface height (SSH) anomaly (see also Keffer and Holloway, 1988). The rationale for this closure is that gh'/f provides a streamfunction for eddy the surface flow; its spatial derivatives give the eddy velocities, so the streamfunction can be considered the product of the eddy velocity and a length scale, which Holloway (1986) associated with L_{mix}. This idea was tested by Kushner and Held (1998) in an atmospheric context, who concluded it was adequate. Stammer (1998) proposed a variant of the idea in which the mixing length was related to the local Eady timescale. These works provided great insight into the spatial patterns of mixing. However, the presence of the unknown constant α complicates the interpretation of such results, allowing them to be tuned to give plausible diffusivities. Thompson and Young (2007) recently showed, through an exhaustive suite of numerical simulations of geostrophic turbulence, that α itself is not a universal constant but rather varies with parameters of the turbulence, in particular, with frictional damping. Since ocean mesoscale turbulence itself spans a wide range of parameter regimes and dissipation mechanisms, there is no guarantee that a constant α is appropriate. Moreover, the formula of Holloway (1986) has recently been demonstrated to over-estimate the diffusivity in the Southern Ocean, where strong mean flows suppress mixing by decreasing the mixing length (Marshall et al., 2006; Ferrari and Nikurashin, 2010). A more sophisticated variant of the mixing-length theory, developed by Ferrari and Nikurashin (2010) and further explored by Klocker et al. (2011a), shows improved skill by accounting for the mean flow; however, this modified formula contains not one but two tuning parameters that are not trivial to infer from the observations.

An alternative approach is to directly model the evolution of a tracer using the satellite-derived velocity fields, bypassing the need for a theoretical closure for the mixing length. Inspired by the use of this technique in the atmospheric literature (Haynes and Shuckburgh, 2000a,b), Marshall et al. (2006) simulated the passive advection of a tracer in the Southern Ocean and used the resulting tracer distributions to calculate "effective diffusivity" (Nakamura, 1996; Winters and D'Asaro, 1996). The

effective diffusivity directly measures the enhancement of mixing due to the stretching of tracer contours by eddies. A great advantage of this method is that, in the limit of large Péclet number, and if the Bachelor scale is resolved by the numerics, the resulting diffusivities are independent of any unknown tuning parameters, including the small-scale diffusivitiy (Shuckburgh and Haynes, 2003; Marshall et al., 2006). A disadvantage of the effective-diffusivity methods is that it produces only contour-averaged diffusivities, rather than two-dimensional maps.

The effective-diffusivity method has thus far only been applied to the Southern Ocean, for two reasons: (1) eddy fluxes are known to be important there (de Szoeke and Levine, 1981), and (2), the geometry of the flow is well suited to the method. Effective diffusivity requires a monotonic tracer gradient in order to work—in flows with no coherent tracer gradient, it is impossible to map the diffusivities to a particular location in space. The strong fronts of the ACC have clearly defined, consistent gradients in density, temperature, and salinity. Thus the mixing inferred from the effective diffusivity technique is readily interpreted as applicable to meridional eddy fluxes. Furthermore, the mean flow of the ACC is aligned with these tracer contours, making the monotonic gradient easy to maintain.

The goal of this study is to use satellite-derived velocities and tracer-based methods to estimate mixing rates *globally*, not just in the Southern Ocean. Towards this end, in Section 3 we first study a "channelized" version of the East Pacific, in which the mean flow is forced to be completely zonal and the domain is made re-entrant. This allows us to compute effective diffusivity at all latitudes using the same methods as Marshall et al. (2006), providing a useful starting point and connection to previous studies. We show that the mean flow has a strong role in shaping the mixing rates at all latitudes, not just in the Southern Ocean.

Adapting effective diffusivity to work outside of this simplified geometry, in realistic ocean basins, presents more of a challenge: there is no obvious monotonic tracer gradient to use. Sea-surface temperature (SST), for example, peaks near the equator and has very weak gradients in much of the tropical ocean. Furthermore, it contains local extrema in various location. A global effective diffusivity calculation could de-

liver, for instance, an average diffusivity associated with the 18° surface isotherm, but this isotherm outcrops in so many different regions of the ocean that such an average value would be almost meaningless. To overcome these difficulties, we turn to a different diagnostic in Section 3: the Osborn and Cox (1972) diffusivity, also developed by Nakamura (2001), which provides information about the local rate of irreversible mixing based on the tracer variance budget in; unlike effective diffusivity, this diagnostic can be applied in two dimensions. We introduce this diagnostic in steps, first in the context of the the Pacific channel, and then globally. We should how the Osborn-Cox diffusivity provides a complete picture of cross-gradient mixing if the variance budget is local and steady, but that in general other fluxes can be present that are not represented by the Osborn-Cox diffusivity. By diagnosing the variance budget from global simulations, we should that the variance budget is approximately local on large scales.

We then calculate Osborn-Cox diffusivities from the global tracer advection experiment, producing a map of irreversible mixing rates for the whole ocean. We perform these experiments with and without mean flows, finding not only suppression of mixing by the mean flow (as in the Southern Ocean studies previously mentioned) but also enhancement at lower latitudes. Finally, in Section 4 we apply the mixing rates to estimate the eddy stress in the surface layer due to the eddy flux of quasi-geostrophic potential vorticity.

3.2   Data and Numerical Advection Model

3.2.1   AVISO Geostrophic Velocity Data

The satellite data used in this study are from the AVISO archive.[1] Specifically we use the geostrophic velocities derived from the gridded, delayed-time, reference, merged sea-level anomaly fields (known as *dt_ref_global_merged_msla_uv* in AVISO parlance.) We choose to use the pre-computed geostrophic velocities, rather than computing

---

[1]AVISO stands for Archiving, Validation and Interpretation of Satellite Oceanographic data. http://www.aviso.oceanobs.com/

our own from the sea-level anomaly for two reasons: (1) to facilitate easy replication of our results, and (2) to take advantage of the sophisticated treatment employed by AVISO computing velocities near the equator. The velocity fields are available on a 1/3° Mercator grid every seven days. We use 17 years worth of observations, beginning with Jan. 6, 1993.

The altimeter measures the anomaly of sea-surface height (SSH), which we will call h', from its mean height, and thus captures mesoscale variability. The geostrophic velocities associated with the SSH anomalies are

$$u'_{AV}, \ v'_{AV} = \frac{g}{f} \left(-\frac{\partial h'}{\partial y}, \frac{\partial h'}{\partial x} \right) \tag{3.1}$$

where $g = 9.8$ m^2 s^{-1} and f is the local Coriolis parameter. (We use Cartesian coordinates here for notational simplicity, but in practice all derivatives are computed appropriately for spherical geometry.) At the scales under consideration here, the Rossby number is very low and consequently the geostrophic flow can be expected to dominate the overall flow field, with Ekman transports and other ageostrophic motions making only a second-order contribution.

Geostrophic balance does not hold at the equator, but the altimetry data can still be used to infer velocities there, albeit with less confidence. The AVISO dataset implements the method of Lagerloef et al. (1999) between ±5°. The basic balance underlying this method is the y-derivative of the meridional geostrophic balance at the equator: $\beta u' = -gh'_{yy}$ (Picaut et al., 1989). The Lagerloef et al. (1999) method is essentially a way of matching this regime with the geostrophic regime away from the equator. The method has been validated with drifter data and has been demonstrated to capture the major features and variability of the equatorial circulation. Regardless, we must maintain some skepticism of our results right at the equator.

3.2.2 Interpolation and Divergence Correction

In order to resolve fine-scale filaments in the tracer field, we model the tracer advection at finer resolution than the original AVISO grid. The raw AVISO velocity fields are

linearly interpolated to a $1/10°$ lat-lon grid. The bathymetry for the fine resolution grid is derived from the General Bathymetric Chart of the Oceans (GEBCO) 1-arc-minute gridded data, distributed by the British Oceanographic Data Service.[2]

To conserve tracer under two-dimensional advection, the advecting velocity fields must be non-divergent and must have no flow normal to the boundary. However, divergence is present in the AVISO-derived velocities for several reasons: (1) the variation of f with latitude, (2) the algorithm used at the equator, and (3) the interpolation to a finer grid. Furthermore, the normal flows are also not guaranteed to vanish at the boundaries. We therefore derive non-divergent velocities from the AVISO fields following the procedure of Marshall et al. (2006). Via a Helmholtz decomposition, the full AVISO field can be written as the sum of a non-divergent streamfunction component and a velocity potential component:

$$\boldsymbol{v}'_{AV} = \nabla \times \psi + \nabla \chi \ . \tag{3.2}$$

The "corrected", divergence-free field is

$$\boldsymbol{v}' = \boldsymbol{v}'_{AV} - \nabla \chi. \tag{3.3}$$

To determine χ we solve the elliptic problem

$$\nabla \cdot \boldsymbol{v}'_{AV} = \nabla^2 \chi \tag{3.4}$$

subject to the boundary condition $\nabla \chi = \boldsymbol{v}'_{AV} \cdot \hat{\boldsymbol{n}}$ to eliminate flow normal to the boundary.

The RMS eddy velocity $|\boldsymbol{v}'|$, the RMS correction velocity $|\nabla \chi|$, and the ratio of these two terms are all plotted in Fig. 3-1. Over most of the ocean, the correction term is $O(0.1)$ or less when compared to the eddy velocities. The magnitude of the correction term appears substantially larger near the equator; however, since the eddy velocities are also large in this region, the ratio of the terms remains small,

---

[2]http://www.gebco.net/

72

generally < 0.3 even at the equator. The ratio only exceeds 0.5 near boundaries in the equatorial region.

3.2.3   Mean Flow

The presence of mean flows can fundamentally alter mixing rates, and quantifying this effect on a global scale is a central goal of our study. Satellite altimetry measures only sea-level *anomaly*, not absolute sea-level, and therefore does not provide information about the mean flow. The best possible estimates of long-term mean flows are produced by ocean state estimation, in which all available observations, including those from the satellites in the AVISO archive, are assimilated in a physically consistent manner via an ocean model (Wunsch and Heimbach, 2009). We use the time-averaged flow at 10m depth from the ECCO-GODAE v3.73 state estimate, on a 1° grid, to define our mean flow. To make this flow non-divegent, it was also interpolated and corrected in the manner described above. Experiments are performed both with and without the mean flow.

The AVISO archive also provides an "absolute dynamic topography" product that includes a mean flow at the surface. This mean flow product is referred to as *CNES-CLS09_v1*. We performed experiments using this mean flow and found minimal differences in results. The AVISO mean flow, on a 1/3° grid, contains narrower jets and other finer-scale features, but does not differ greatly from the ECCO mean flow. Since the AVISO mean flow is also derived using data assimilation techniques, rather than "directly" observed, we prefer to use the ECCO product, which is proven to be an optimal fit to the observations.

3.2.4   Advection / Diffusion Model

To perform the tracer advection, we make use of the MITgcm framework (Marshall et al., 1997a,b). We employ the model in "offline" mode, where the dynamical core is disabled and the velocity fields are loaded from the AVISO data. The code simply

(a)

RMS Eddy Velocity (cm/s)

(b)

RMS Velocity Correction (cm/s)

(c)

Correction Velocity / Eddy Velocity
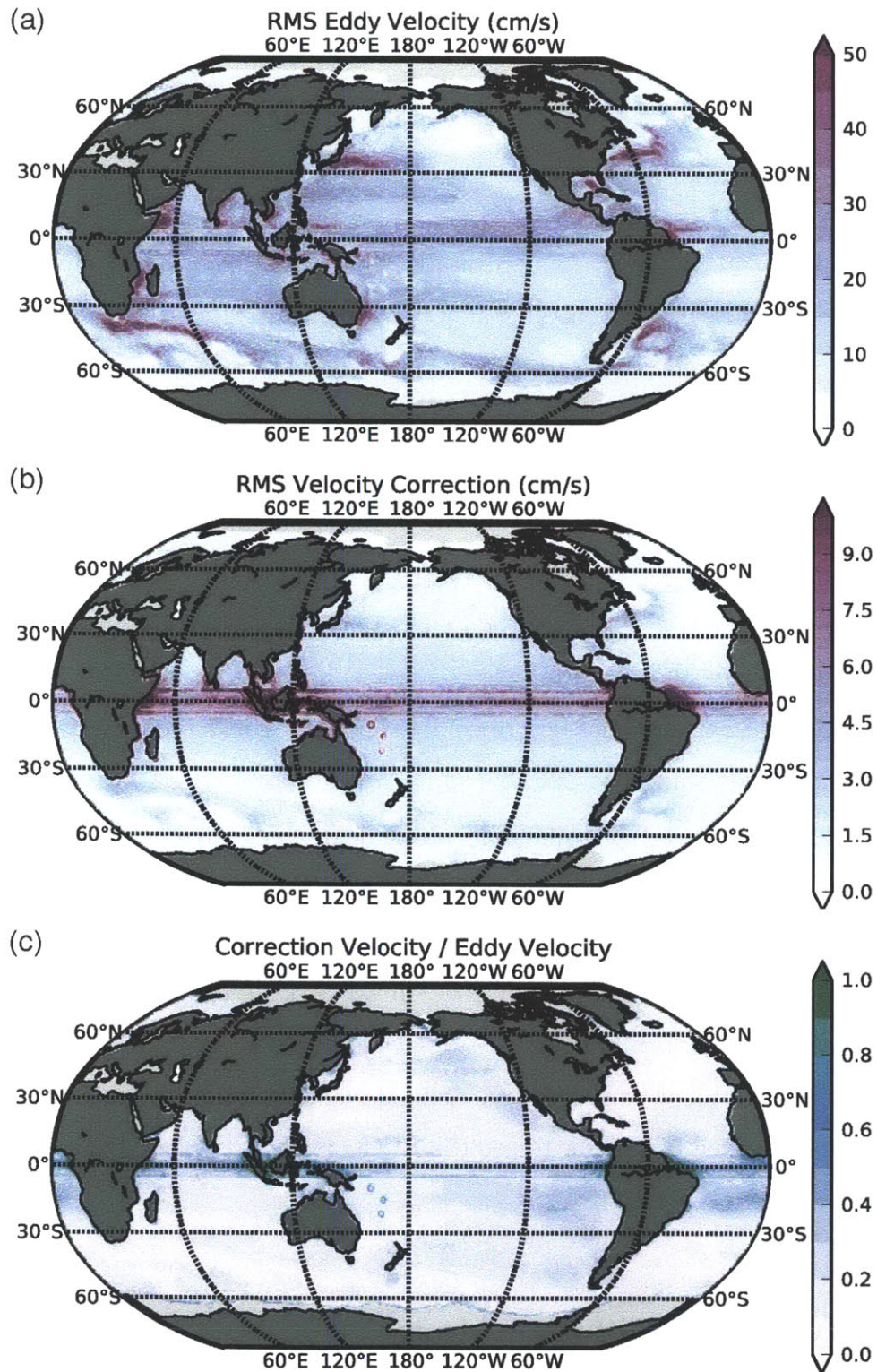
Figure 3-1: (a) RMS eddy velocity $|\boldsymbol{v}'|$. (b) RMS correction velocity $|\nabla \chi|$. (c) The ratio of the two.

solves the two-dimensional advection diffusion equation

$$\frac{\partial q}{\partial t} + \boldsymbol{v} \cdot \nabla q = \kappa \nabla^2 q \tag{3.5}$$

where κ is a horizontal diffusivity. Many different numerical schemes exists for solving this equation; we experimented with the standard second-order centered difference scheme and also a second-order scheme with a flux limiter. Both schemes performed reasonably. However, the second-order scheme without limiter sometimes introduced spurious extreme values of q, far outside its expected range, in regions of high mixing. These extreme values result in inflated ∇q, which corrupts the mixing diagnostics. For this reason, we opted to use the the flux-limiting scheme.

The small-scale diffusivity κ plays in a important role in several mixing diagnostics. It is well known that numerical advection / diffusion can introduce extra diffusion beyond what is specified explicitly by κ. We quantify this effect, as done in Marshall et al. (2006) and Abernathey et al. (2010), through the domain-averaged tracer variance budget. Multiplying (3.5) by q and taking an integral over the entire domain gives

$$\frac{\partial}{\partial t} \int \int \frac{q^2}{2} dA = -\kappa_{num} \int \int |\nabla q|^2 dA \ . \tag{3.6}$$

where the quantity κ_{num} is a measure of the total amount of diffusion, explicit and implicit, in the model. (By taking κ_{num} outside the integral, we have assumed that it, like the explicitly specified κ, is constant in space; this assumption may not be valid, but computing the numerical diffusivity locally is not possible with this method.) We can evaluate these integrals from the model output and solve for κ_{num}. We tested values of κ ranging from 25 to 150 m^2 s^{-1}. Tracers were initialized with a gradient in latitude and evolved for one year, with q output every month. This was repeated for four separate years of altimetric data. The results, shown in Fig. 3-2-a, indicate that κ_{num} is maximum at the beginning of the advection but within a few months settles into a reasonably steady state. The details of the flow clearly affect κ_{num} since it varies differently in each separate year. However, these variations are relatively small. The mean values of κ_{num} are given in Tab. 3.1. In what follows, κ_{num} will

Table 3.1: Average numerical diffusivity κ_{num} diagnosed from (3.6).

κ ($m^2 s^{-1}$)	κ_{num} ($m^2 s^{-1}$)
25	63 ± 12
50	83 ± 15
75	104 ± 17
100	126 ± 20
125	148 ± 23
150	171 ± 25

always be used in place of κ when analyzing our simulations.
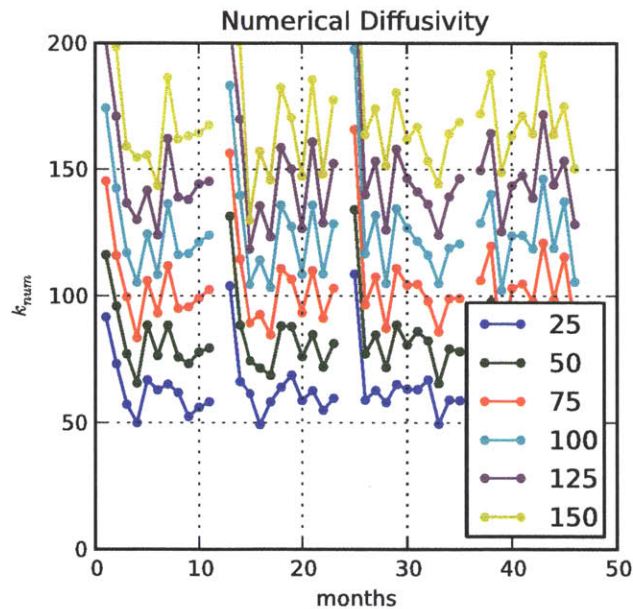
Figure 3-2: Numerical diffusivity κ_{num} over time diagnosed from (3.6) for six different tracers with different values of κ (whose values are in the legend). The tracers are reset every year.

3.3 Effective Diffusivity in a Pacific Sector

Effective diffusivity developed as a diagnostic in the mid-latitude troposphere and stratosphere (Nakamura, 1996; Nakamura and Ma, 1997; Haynes and Shuckburgh, 2000a,b) and was later applied to the Southern Ocean / ACC system (Marshall et al.,

2006; Shuckburgh et al., 2009a,b; Abernathey et al., 2010). Both these environments share an important feature: tracers have a strong, monotonic gradient in latitude, with the mean flow oriented perpendicular to the tracer gradients. The geometry of the mean flow in other ocean basins, however, is much more complex, with gyres, western boundary currents, and equatorial jets all playing a role. Futhermore, surface tracers (temperature and salinity) are not simply aligned with streamlines globally, as they are in the ACC, because strong air-sea forcing and vertical advection often dominate over advection by the mean flow. These issues make it very challenging to select an initial tracer distribution with which to perform a truly global effective diffusivity calculation: without forcing, the tracer contours will be strongly deformed by the mean flow, but with forcing, the effective diffusivity diagnostic can give very different results (Shuckburgh et al., 2011).

As a bridge to understanding mixing rates globally, we performed the following experiment: we took a sector in the east Pacific (180° to 130° W longitude, full range in latitude) and turned it into a re-entrant channel. This sector is unique in that it contains very little land and that the EKE is relatively homogenous in longitude. The mean flow (from ECCO) was zonally averaged and made costant in longitude $(\overline{u} = \overline{u}(y))$, with $\overline{v} = 0$. (The meridional mean flow was already weak in this sector.) The eddy velocities were derived from AVISO as described in the previous section, and were made consistent at the overlap longitude during the correction step. Shuckburgh et al. (2009b) and Ferrari and Nikurashin (2010) also performed experiments of this type in limited Southern Ocean sectors.

Although this synthetic flow seems far removed from the real ocean, it contains the essential elements necessary to correctly assess *meridional* mesoscale mixing rates. Obviously there is more to tracer transport than *just* eddy mixing, but it is the mixing we are interested in here. With the mean flow purely zonal, and with the eddy properties (EKE, eddy size, phase speed, etc.) varying strongly in latitude, we can initialize a tracer with a constant meridional gradient and study its evolution. This is now an ideal flow for diagnosing effective diffusivity

3.3.1 Effective Diffusivity Calculation

The effective diffusivity is defined as

$$K_{eff} = \kappa \frac{L_e^2}{L_{min}^2} \ .$$
(3.7)

L_e is the "equivalent length" of a tracer contour deformed by eddies, L_{min} is the minimum possible contour length, and κ is the small-scale background diffusivity. Nakamura (1996) showed that the equivalent length of a tracer contour q, enclosing an area of $A(q)$, can be expressed as

$$L_e^2(q) = \frac{\frac{d}{dA} \int_A |\nabla q|^2 dA}{\left(\frac{\partial q}{\partial A}\right)^2}$$
(3.8)

where the integral is taken over the area A. This expression is easy to evaluate numerically for a tracer concentration $q(x,y)$, and its value is readily mapped to an "equivalent latitude," i.e. the latitude of the mean tracer contour $\overline{q}(y)$. (The mapping is much harder if the geometry of the mean contours is more complex; this was part of the motivation to perform the simple periodic-domain experiment in the first place.) Likewise, $L_{min}(y)$ is trivially defined as the width of the $50°$ domain at each point in latitude. Our initial tracer is proportional to latitude: $q(x,y,t=0) = y$.

Since the true background value of κ in the ocean is unknown, the K_{eff} estimate is more reliable if it is independent of κ. As discussed in Marshall et al. (2006), K_{eff} becomes independent of κ the time scale associated with the eddy strain rates greatly exceeds the diffusive time scale associated with κ. Physically, this independence is due the fact that a smaller κ permits finer tracer filaments, allowing L_e to increase. To test whether this is the case in our experiments, we performed tracer a advection experiment in the Pacific channel using the six values of κ_{num} specified in Tab. 3.1. The tracers were allowed to evolve for one year, at which point K_{eff} was calculated using the appropriate values of κ_{num} for each tracer. The results, in Fig. 3-3, convincingly show that the K_{eff} is quite independent of κ_{num} over most of the domain. Some slight differences occur, for instance, in the peak near the equator. Inside this
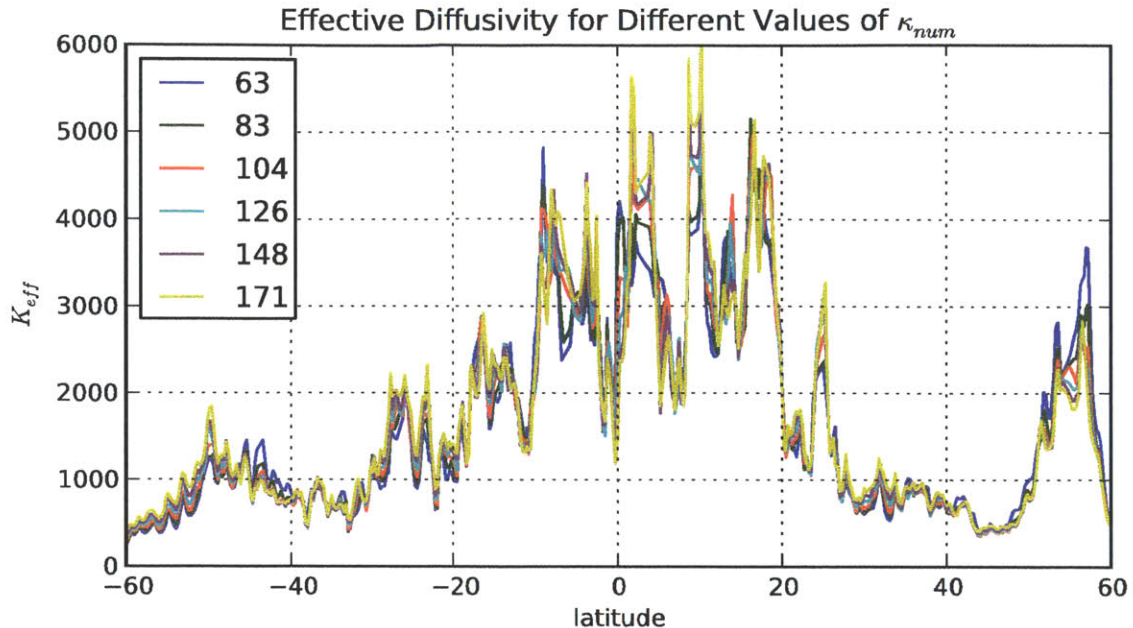
Figure 3-3: Comparison of K_{eff} values for six different κ_{num}, whose values are given in the legend.

peak, the K_{eff} values stratify by κ_{num}. One possible explanation could be that the *global* values of κ_{num} in these peaks are not appropriate, and that small-scale numerical dissipation where there is very intense mixing is enhanced locally beyond κ_{num} for small values of κ. Two important conclusions can be drawn from this experiment. First, the correct value of κ_{num} is clearly essential to obtain the correct K_{eff}; using the original values of κ would lead to much greater discrepancies. Second, the overall patterns and magnitude of K_{eff} does not depend strongly on κ, except perhaps in the peaks. All the subsequent analysis will be performed with $\kappa = 25$ m^2 s^{-1} / $\kappa_{num} = 63$ m^2 s^{-1}.

Next, we examine the temporal variations in K_{eff}. We allow this tracer to evolve for a year and compute L_e every month. At the end of the year, the tracer is re-initialized, and the process is repeated every year from 1993 through the end of 2009. A second tracer is also modeled, six months out of phase with the first, in order to better resolve the temporal variability. The results from each computation are shown in Fig. 3-4. As the figure shows, K_{eff} generally equilibrates quite rapidly (within 2 or

3 months) and then plateaus for the remainder of the year. (If the simulations were allowed to run on indefinitely, K_{eff} would eventually fall again as the tracer became homogenized in regions of intense mixing.)
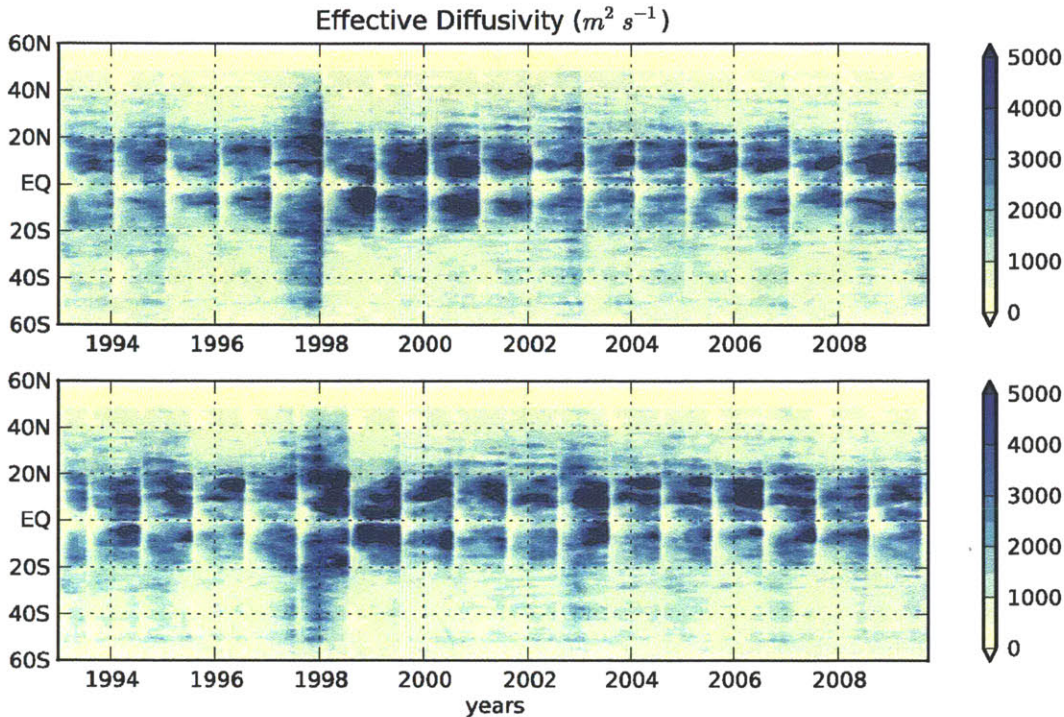
Figure 3-4: Monthly K_{eff} values as a function of equivalent latitude and time in the Pacific zonal sector experiment. The two tracers (top and bottom panels) are reset to their original concentration once a year, but six-months out of phase.

Some significant temporal variability is evident, with particularly intense mixing taking place in 1997-1998. The fact that this period coincides with a very strong El Niño event is quite intriguing, especially given the fact that the mean flow does not vary in time in these experiments. This suggests that ENSO-related processes can directly affect mixing rates by eddies. The temporal variability is not the subject of this study and will not be considered further, but it is an exciting topic for future study.

We compute a mean K_{eff} by averaging over the last 6 months of each year. This mean value and its standard deviation are plotted in Fig. 3-5 (black line).
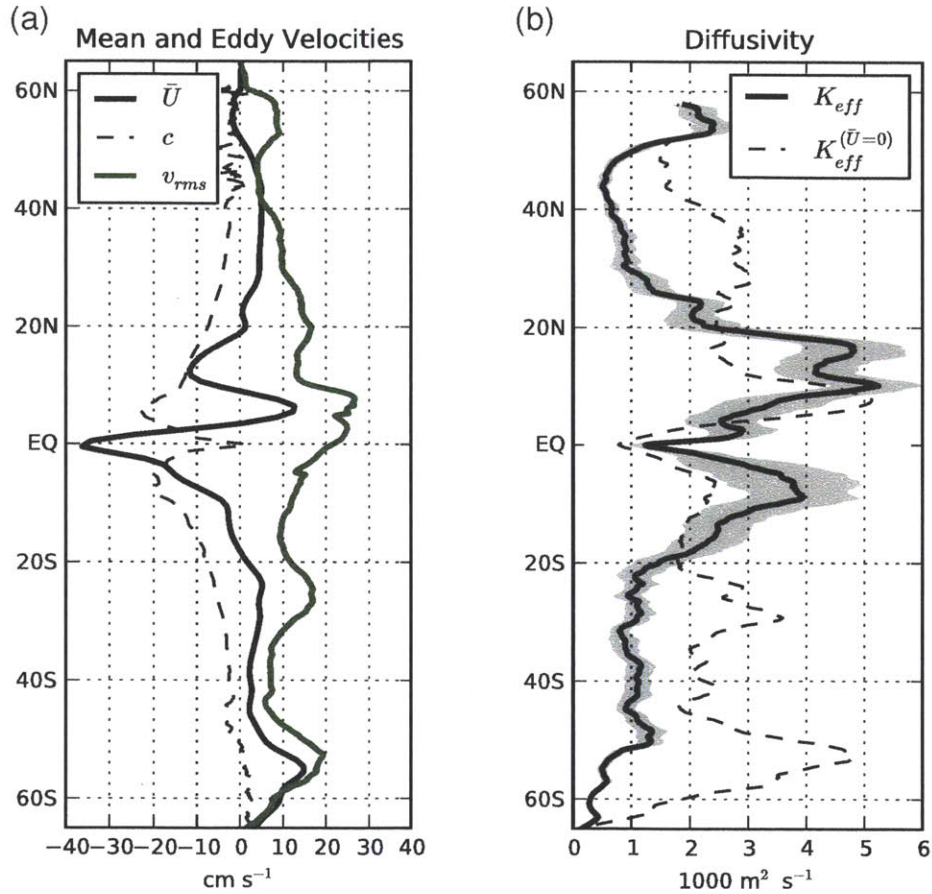
Figure 3-5: (a) Zonal mean flow $\bar{u}$, dominant phase speed c, and RMS eddy speed from the Pacific zonal sector experiment. The phase speed was diagnosed from the altimetric sea-surface height using Radon transforms by Chris Hughes (personal communication). (b) Diffusivity diagnostics. The mean K_{eff} is in black, with $\pm$ one standard deviation in gray. The dashed line shows the mean K_{eff} produced when the mean flow is set to zero.

3.3.2 Discussion of Mixing Rates and Mean Flow Effects

Building on work by Taylor (1921), Prandtl (1925), and Keffer and Holloway (1988), Ferrari and Nikurashin (2010) developed a simple analytical model for mixing across a jet, representing eddy effects with a stochastic advection term. They cross-jet diffusivity was found to be

$$K_\perp = \frac{\gamma}{\gamma^2 + k^2(\bar{u} - c)^2} EKE \tag{3.9}$$

where γ is the eddy decorrelation timescale, k the eddy wavenumber, $EKE = \overline{u'^2 + v'^2}/2$ the eddy kinetic energy, $\bar{u}$ the zonal mean flow, and c the eddy phase speed. (A similar expression can be derived for the QGPV diffusivity in a baroclinically unstable flow (Green, 1970).) Here we do not attempt to fit this formula to our results exactly; the constants k and γ can be difficult to asses. Nevertheless, the formula provides a very useful framework for interpreting our diagnosed diffusivities. In particular, we see that $K_\perp$ depends on the eddy kinetic energy, but also on a factor $(\bar{u} - c)^2$: given a particular EKE, the diffusivity is maximized when this term is zero. The diffusivity can be suppressed by presence of propagating eddies and / or by a mean flow. We plot EKE and $\bar{u}$ for our domain in Fig. 3-5-a. We also plot phase speeds c from the region inferred by Radon transforms of sea-surface height data, courtesy of Chris Hughes (personal communication).

We also performed the same experiment with the *mean flow removed*, i.e. $\bar{u} = 0$. The K_{eff} for the zero-mean-flow case is shown as the dashed line in Fig. 3-5-b. This experiment helps to highlight the role of the mean flow in setting mixing rates.

Beginning in the Southern Ocean, we see a picture already familiar from the work of Marshall et al. (2006), Ferrari and Nikurashin (2010), and Klocker et al. (2011b,a): relatively weak mixing in the core of the ACC where the mean flow is strongest, and slightly elevated values on the equatorward flank where eddy energy is still high but the mean flow is weaker. Comparing with the zero-mean-flow values, we see that the mean flow is strongly suppressing mixing rates; without it, they reach values > 4000 m^2 s^{-1} in the ACC. Moving north to the midlatitudes, we see relatively

uniform mixing between 40°S and 20°S of approximately 1000 m^2 s^{-1}, encouragingly close to the canonical Gent-McWilliams coefficient. It is intriguing to note, however, that the relatively weak eastward mean flow in this region still exerts a suppressing effect; without it, the mixing rates double.

Closer to the equator, the picture becomes more complex and interesting. North of 20°S, the mixing rates increase up to a peak of $\sim$ 4000 m^2 s^{-1} around 5°S. Furthermore, these values are evidently *enhanced* by the mean flow rather than suppressed. This behavior can be easily explained in terms of (3.9): as shown in Fig. 3-5-a, the phase speed c is negative throughout most of the domain, consistent with westward propagating Rossby waves (Chelton and Schlax, 1996; Tulloch et al., 2009). South of 20°S, $\overline{u}$ is westward: setting $\overline{u} = 0$ in this region reduces $(\overline{u} - c)^2$ and amplifies the diffusivity. In contrast north of 20°S, the mean flow is westward too, and $(\overline{u} - c)^2 < c^2$. Close to the equator there is a point where $\overline{u} \simeq c$, coincident with a maximum in K. Of course, the mixing rates are also modulated by the variations in EKE, but this experiment suggests a very strong role for the $(\overline{u} - c)^2$ term in the sub-equatorial region. Right at the equator, $c \to 0$ while $\overline{u}$ remains strongly westward and mixing rates drop.

In some ways, the northern hemisphere mirrors the southern, but there are important differences. While EKE peaks around 5°N, this is also the latitude of the equatorial counter-current, whose strong eastward flow evidently suppresses mixing considerably. Near 15°N north, however, we encounter another region where $\overline{u} \simeq c$ and another maximum in K. North of 20°N, the picture is the same as in the southern mid-latitudes: mixing rates of $O(1000$ m^2 s$^{-1})$. The peak in K near 55°N is associated with high EKE near the Aleutian islands and Alaskan coast.

Overall, this sector displays a wide range of mixing rates, spanning an order of magnitude from 500 to 5000 m^2 s^{-1}. These mixing rates are shaped by meridional variations in EKE, $\overline{u}$ and c. Especially high mixing rates in the sub-equatorial regions arise due to relatively high EKE combined with an alignment between the westward mean flow and westward propagating eddies. It seems likely that coarse ocean models, using a constant eddy diffusivity of 1000 m^2 s^{-1}, are strongly underestimating eddy

fluxes in these regions.

3.4 Global Mixing Rates

The East Pacific is ideal for investigating mixing rates using K_{eff} because of its lack of land and relative zonal symmetry. But focusing only on this sector neglects the regions of highest EKE in the global ocean: the western boundary currents. Unfortunately the complicated geometry of the mean flows near western boundaries makes it very difficult to calculate K_{eff} there in a robust way. In this section, we make use of a different diagnostic, the Osborn-Cox diffusivity (K_{OC}), for assessing mixing globally. The origin of this diagnostic lies in the tracer variance budget; it represents the part of the down-gradient eddy flux associated with irreversible mixing. We examine the variance budget first in the zonal channel described in the previous section, and we show that K_{OC} agrees with K_{eff}. We then move to the global view.

3.4.1 Eddy Diffusivity and the Variance Budget

By taking a time mean of (3.5), we obtain the Reynolds-averaged tracer equation:[3]

$$\frac{\partial \overline{q}}{\partial t} + \overline{\boldsymbol{v}} \cdot \nabla \overline{q} = -\nabla \cdot \overline{\boldsymbol{v'}q'} + \kappa \nabla^2 \overline{q} \; . \tag{3.10}$$

The overbar indicates a time / ensemble mean, and a prime a departure from that mean, such that $q = \overline{q} + q'$. This equation describes the evolution of the mean tracer $\overline{q}$ and looks identical to (3.5) except for the eddy flux term on the right.

The eddy flux can be decomposed into components perpendicular ($\overline{\boldsymbol{v'}q'}_{\perp}$) and

---

[3]This derivation is based on the paper by Nakamura (2001).

parallel ($\overline{v'q'}_\parallel$, a.k.a. the "skew" flux) to the tracer gradient:

$$\overline{v'q'} = \overline{v'q'}_\perp + \overline{v'q'}_\parallel \tag{3.11}$$

$$= (\overline{v'q'} \cdot \hat{n})\hat{n} - (\overline{v'q'} \times \hat{n}) \times \hat{n} \tag{3.12}$$

$$= \frac{\overline{v'q'} \cdot \nabla\overline{q}}{|\nabla\overline{q}|^2}\nabla\overline{q} - \frac{\overline{v'q'} \times \nabla\overline{q}}{|\nabla\overline{q}|^2} \times \nabla\overline{q} \ . \tag{3.13}$$

(The unit normal vector $\hat{n} = \nabla\overline{q}/|\nabla\overline{q}|$ points up the mean gradient.) These two components behave differently. Our focus will be on the cross-gradient flux, but first we discuss the skew flux. (Eden et al. (2007) discuss these decompositions in detail.)

By manipulating second term, it can be seen that the divergence of the skew flux can be represented as advection by a non-divergent eddy velocity $v_e = \hat{k} \times \nabla\psi_e$, such that

$$\nabla \cdot \overline{v'q'}_\parallel = -v_e \cdot \nabla\overline{q} \tag{3.14}$$

The streamfunction ψ_e can be written as

$$\psi_e = (\overline{u'q'}\frac{\partial\overline{q}}{\partial y} - \overline{v'q'}\frac{\partial\overline{q}}{\partial x})|\nabla\overline{q}|^{-2} \ . \tag{3.15}$$

Integrated around a closed contour of $\overline{q}$, the skew flux divergence is zero. Furthermore, the eddy velocity can be combined with the mean velocity to define a residual advection velocity, as in transformed Eulerian mean theory (Andrews and McIntyre, 1976; Andrews et al., 1987; Plumb and Ferrari, 2005). This residual tracer equation is

$$\frac{\partial\overline{q}}{\partial t} + (\overline{v} + v_e) \cdot \nabla\overline{q} = -\nabla \cdot \overline{v'q'}_\perp + \kappa\nabla^2\overline{q} \ . \tag{3.16}$$

Seen in this form, the skew flux is clearly not representative of the sort of non-conservative process that we associate with mixing. The non-conservative part of the flux lies entirely in the cross-gradient flux $\overline{v'q'}_\perp$.

The nature of the cross-gradient flux can be illuminated by considering the tracer variance budget. This budget is obtained by subtracting (3.10) from (3.5), multiplying

by q' and taking the average. The resulting equation is

$$\frac{\partial}{\partial t}\frac{\overline{q'^2}}{2} + \nabla \cdot \overline{v\frac{q'^2}{2}} + \overline{v'q'} \cdot \nabla\overline{q} = \nabla^2\left(\kappa\frac{\overline{q'^2}}{2}\right) - \kappa\overline{|\nabla q'|^2} \qquad (3.17)$$

and the quantity $\overline{q'^2}/2$ is the tracer variance. The first term is the variance tendency, and the second represents advection of variance. The third term, $\overline{v'q'} \cdot \nabla\overline{q}$, involves the cross-gradient eddy flux. (Because the skew flux is parallel to $\nabla\overline{q}$, it does not enter the variance budget.) Locally, the cross-gradient flux can be a source or sink of variance, depending on its direction relative to $\nabla\overline{q}$.

We now integrate this variance equation (3.17) in space over the whole domain, assuming a steady state, and using the divergence theorem to eliminate all fluxes at the boundary. This global budget for tracer variance is

$$\int\int \overline{v'q'} \cdot \nabla\overline{q}\,dxdy = -\int\int \kappa\overline{|\nabla q'|^2}dxdy\,, \qquad (3.18)$$

which states that the production of variance from the mean flow (the term on the left) is balanced by dissipation of variance by small-scale mixing (the term on the right). Since the right side is negative definite, so must be the left side; this is implies that the cross-gradient flux must be, on average, *down* gradient. We now define an eddy transfer coefficient (i.e. eddy diffusivity) for the cross-gradient flux, such that

$$\overline{v'q'}_\perp = -K_\perp\nabla\overline{q}\,. \qquad (3.19)$$

The global budget then becomes

$$-\int\int K_\perp|\nabla\overline{q}|^2dxdy = -\int\int \kappa\overline{|\nabla q'|^2}dxdy\,. \qquad (3.20)$$

We can see from this expression that $K_\perp$ must be, on average, positive. Indeed, (3.20) is the underlying justification for any attempt to represent eddy fluxes as down-gradient diffusion. The dissipation term on the right side is unambiguously identified with irreversible mixing.

86

Osborn and Cox (1972) wanted to estimate the eddy vertical flux of heat, and the associated vertical diffusivity, based on microstructure measurements of the vertical temperature gradient. To do so, they essentially assumed that the *global* variance balance of (3.18) held *locally*, neglecting the other terms in (3.17). Regardless of whether this is the case, we can always identify the portion of the production term that is locally balanced by the dissipation term. We label this flux as $\overline{v'q'}_{OC}$, the Osborn-Cox flux, and define it as

$$\overline{v'q'}_{OC} \cdot \nabla \bar{q} = -\kappa \overline{|\nabla q'|^2} \, , \tag{3.21}$$

This allows us to define the Osborn-Cox diffusivity K_{OC} by

$$\overline{v'q'}_{OC} = -K_{OC} \nabla \bar{q} \tag{3.22}$$

where

$$K_{OC} = \kappa \frac{\overline{|\nabla q'|^2}}{|\nabla \bar{q}|^2} \, . \tag{3.23}$$

This is the diffusivity for the flux associated with local irreversible mixing; it will play a central role in our subsequent diagnostics. Physically, K_{OC} is quite similar to K_{eff}: it represents the enhancement of small scale mixing due to sharp tracer gradients created by eddy mixing. The factor $\overline{|\nabla q'|^2}/|\nabla \bar{q}|^2$ can be interpreted as ratio of length scales that quantifies the efficiency of this process, just like the factor L_e^2/L_{min}^2 in K_{eff}. In fact, it can be shown that K_{OC} integrated along a tracer contour is equivalent to K_{eff} (see Nakamura, 1996, eq. 2.2 - 2.5).

In general, the other terms in (3.17) will contribute to the variance budget as well, meaning $\overline{v'q'}_{OC} \neq \overline{v'q'}_{\perp}$. However, the leftover flux is qualitatively different from the Osborn-Cox flux, as we shall now see. We we refer to this leftover flux as the *non-local* flux because it arises mainly due to the transport of variance. We define it as

$$\overline{v'q'}_{NL} = \overline{v'q'}_{\perp} - \overline{v'q'}_{OC} \, . \tag{3.24}$$

By subtracting $\overline{v'q'}_{OC} \cdot \nabla\overline{q}$ from (3.17) we can write

$$\overline{v'q'}_{NL} \cdot \nabla\overline{q} = \frac{\partial}{\partial t}\overline{\frac{q'^2}{2}} - \nabla \cdot \overline{v\frac{q'^2}{2}} + \left(\kappa\overline{\frac{q'^2}{2}} \right) \ . \tag{3.25}$$

This equation shows that the non-local flux arises due to the variance tendency (small for quasi-steady states) and to the advection and diffusion of variance. It can be up or down gradient, and we know from (3.18) that the variance fluxes on the right-hand side must vanish in a global integral, implying that they cancel each other out over large spatial scales.

In analyzing the eddy potential energy and enstrophy equations, which both resemble (3.17), (Marshall and Shutts, 1981) considered a similar decomposition of the cross-gradient flux into what they called *rotational* and *divergent* components. Their divergent flux is equivalent to $\overline{v'q'}_{OC}$. Likewise, their rotational flux is related to $\overline{v'q'}_{NL}$; specificially they define

$$\overline{v'q'}_{Rot} \cdot \nabla\overline{q} = -\overline{v} \cdot \nabla\overline{\frac{q'^2}{2}} \ . \tag{3.26}$$

Comparing with (3.24), we see the $\overline{v'q'}_{Rot} = \overline{v'q'}_{NL}$ if the tendency, diffusion, and triple correlation (i.e. $\overline{v'q'^2}$) terms are all neglected, leaving only advection of variance by the mean flow $\overline{v}$.

(Marshall and Shutts, 1981) argued that the divergent flux was more important because it alone contributes to the budget of $\overline{q}$ within mean streamlines. They claimed that $\overline{q}$, in their case representing temperature or potential voriticity, will be generally aligned the streamlines $\overline{\psi}$ of the mean flow, such that then that $q = q(\overline{\psi})$. (Indeed this is expected for any tracer with weak sources / sinks (Rhines and Young, 1982).) Under this assumption, it can then be shown that

$$\int\int_{\overline{\psi}(\overline{q}} \nabla \cdot \overline{v'q'}_{Rot} dx dy = 0 \ , \tag{3.27}$$

i.e. that the rotational flux divergence inside a mean streamline $\overline{\psi}$ is zero, and that

only the divergent fluxes contribute to the budget of $\bar{q}$ (3.10). In retrospect, the neglect of the triple correlation term by Marshall and Shutts (1981) was unjustified. Nevertheless, variance budgets from our simulations (discussed in the subsequent sections) support the conclusions that, in general, the nonlocal fluxes only act to move variance around on small scales, and that the eddy contribution to the budget of $\bar{q}$ on large scales is primarily dominated by $\overline{v'q'}_{OC}$.

3.4.2 Variance Budget and K_{OC} in Pacific Channel Experiments

We first examine the budget for variance and Osborn-Cox diffusivity in the Pacific channel experiments described in the previous sections. The zonal symmetry simplifies the budget and also facilitates easy comparison with K_{eff}. In a zonal average, the variance budget (3.17) simplifies to

$$\frac{\partial}{\partial t}\frac{\overline{q'}^x}{2} + \frac{\partial}{\partial y}\left(\frac{\overline{v'q'^2}^x}{2}\right) + \overline{v'q'}^x\frac{\partial \overline{q}^x}{\partial y} = \frac{\partial^2}{\partial y^2}\left(\kappa\frac{\overline{q'^2}^x}{2}\right) - \kappa\overline{|\nabla q'|^2}^x \qquad (3.28)$$

Because there is no mean meridional flow, the variance advection term only includes the triple correlation. The budget was computed using the Pacific channel simulations described in the previous section. The terms are shown as functions of y in Fig. 3-6. The variance diffusion term (the first term on the right side of (3.28) was two orders of magnitude smaller than the others and so was not plotted. We did not diagnose the tendency term, but instead assume it to be given by the residual. The dominant balance is clearly between variance production ($\overline{v'q'}^x\frac{\partial \overline{q}^x}{\partial y}$) which is everywhere positive and variance destruction ($\kappa\overline{|\nabla q'|^2}^x$), which is negative. The triple correlation term is generally much smaller. In some narrow peaks, its magnitude approaches 1/2 of the other two terms; however, positive peaks are neighbored by negative peaks, indicating that the term acts only on small scales. The residual term is small, at maximum accounting for 20% of the balance. This indicates that the variance is not in a steady state, but rather is evolving slowly over the course of the year.

89
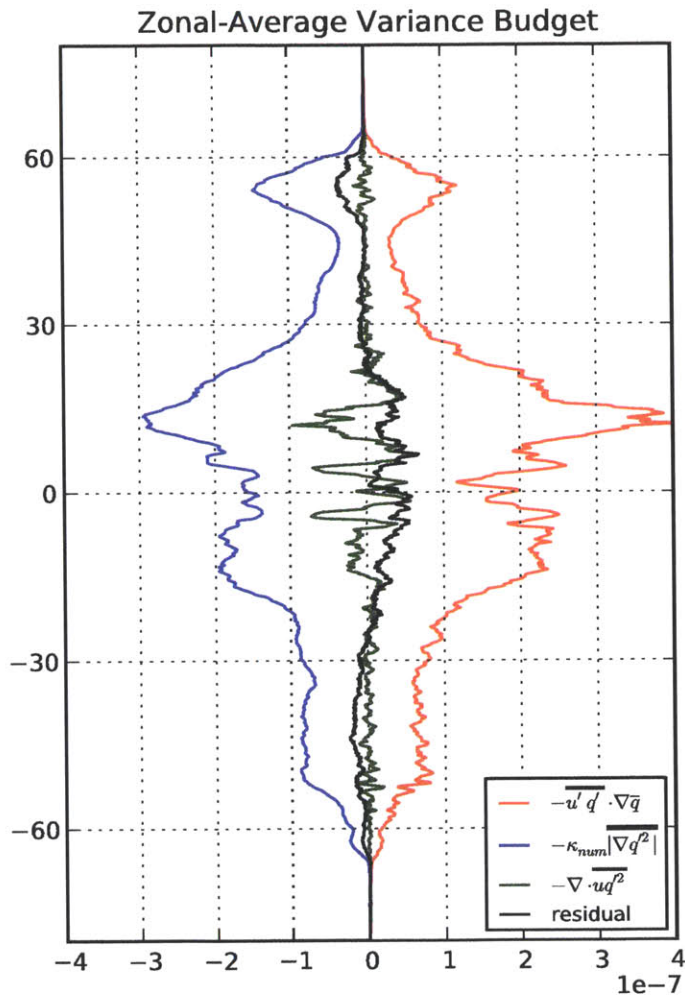
Figure 3-6: Terms in the zonal-mean variance budget (3.28). The tendency term was not diagnosed explicitly but is assumed to be equal to the residual.

Next we consider the mixing diagnostic K_{OC} and compare it to K_{eff}. In a zonally-averaged context, $K_{OC} = \kappa \overline{|\nabla q'|^2}^x / |\nabla \overline{q}^x|^2$. A third quantity worth comparing is

$$K_{flux} = -\overline{v'q'}^x \Big/ \frac{\partial \overline{q}^x}{\partial y} \ , \tag{3.29}$$

a more traditional diagnostic of mixing in channel flows. Based on our preceding discussion of the variance budget, we can see that K_{flux} is a diffusivity for the full cross-gradient flux, including the non-local part $\overline{v'q'}_{NL}$. Thus we expect it to depart from K_{OC} wherever the tendency term or the triple correlation term are significant.
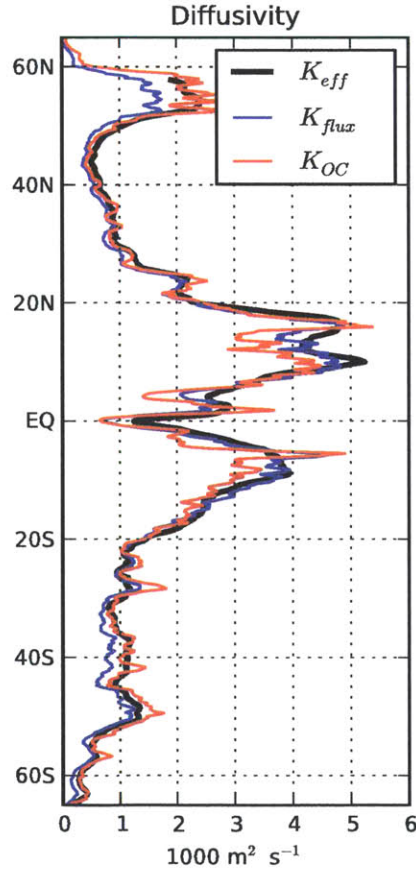
Figure 3-7: Comparison of three different diffusivity diagnostics (K_{eff}, K_{flux}, and K_{OC}) in the Pacific channel experiment.

We plot K_{eff}, K_{flux}, and K_{OC}, in Fig. 3-7; the agreement is quite good in

most places. The slight disagreement between K_{flux} and K_{OC} near 55 N is easily attributed to the presence of a variance tendency at this latitude, apparent in Fig. 3-6. (The same comment applies to the area around 40S.) Some disagreement between diagnostics is also evident in the peaks near the equator. The relatively strong triple correlation term is likely responsible for this. Also, we note that in these regions, we also found disagreement between K_{eff} obtained with different values of κ (see Fig. 3-3); we speculated that this could be due to spatially varying κ_{num} in regions of intense mixing. This could be a possible explanation for the disagreements between K_{eff} and K_{OC}. Overall though, these issues are small, and the three diagnostics give the same broad picture.

The advantage of K_{OC} is that, unlike the other diagnostics, it can give a two-dimensional picture of mixing, revealing variation in x as well as y. To illustrate this, we simply compute the local value of K_{OC}, as defined in (3.23). (The zonal average of this quantity is identical to what is plotted in Fig. 3-7.) The full $K_{OC}(x,y)$ is plotted in Fig. 3-8. A high degree of zonal symmetry is indeed evident, but some zonal variations also emerge, for instance, between 20 S and the equator, or near 50 S. We will now proceed to construct global maps of K_{OC}.

3.4.3 Global Osborn-Cox Diffusivity

The methodology we use for the global experiments follows in a straightforward way from the previous section. We initialize a tracer globally, stir it with the adjusted AVISO velocity field v' in combination with the ECCO mean flow $\overline{u}$, and reset the tracer after one year. The process is repeated for 17 years of AVISO data; the statistics necessary to compute K_{OC} and the terms of the variance budget are generated by time-averaging over the whole 17-year period. This procedure can be viewed as an ensemble of 17 individual yearly experiments. The results are not very sensitive to the averaging period, provided the period is short enough to prevent the tracer gradients from being completely mixed away, in which case K_{OC} becomes undefined.

The main challenge in the global experiment is the choice of an initial tracer. One obvious choice is the same latitude tracer used in the previous section; we will refer
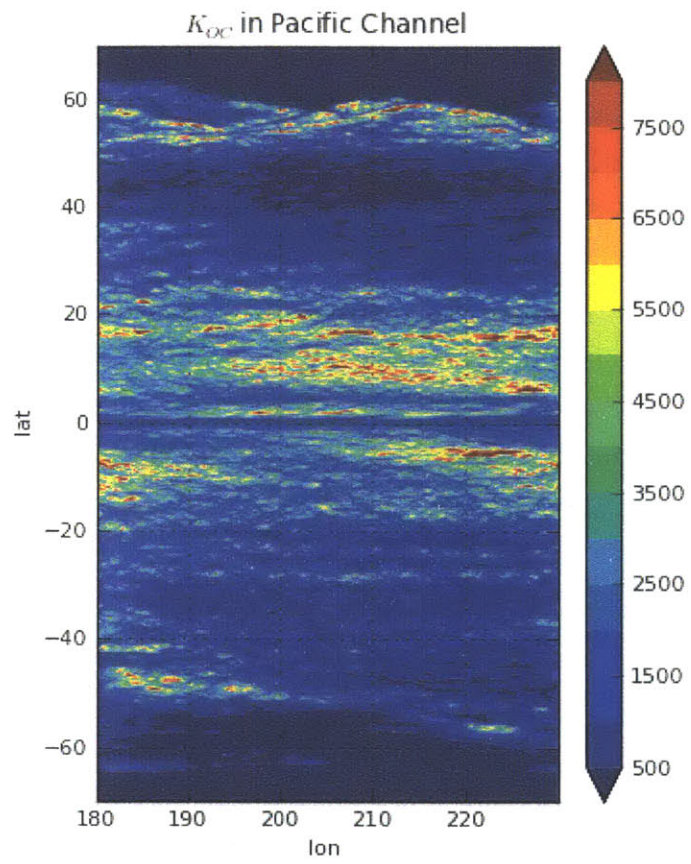
Figure 3-8: K_{OC} (3.23) computed locally in the Pacific channel experiment.

to this tracer as `trLAT`. This tracer facilitates easy comparison with the preceding results. However, a great disadvantage of `trLAT` is that it is no longer necessarily aligned with the mean flow; this misalignment means that the mean flow itself can greatly deform the mean $\bar{q}$ contours and cause irreversible mixing (Young et al., 1982). It would be misleading to identify this mixing with eddies, since it is produced by the mean flow.

An alternative is to use an initial tracer that is perfectly aligned with mean flow everywhere. Since the mean flow is non-divergent, its streamfunction defines such a tracer. We will call this tracer `trPSI`. With the eddies removed, `trPSI` will evolve only very slowly, diffusing weakly across streamlines due to κ but otherwise remaining unchanged. A major disadvantage of `trPSI` is that it contains local maxima and minima, for instance, in the middle of gyres. As previously mentioned, K_{OC} is undefined wherever the background gradient $|\nabla\bar{q}|$ vanishes, and very weak gradients can inflate the value of K_{OC} in an unrealistic way. We also explore a third tracer, the mean sea surface temperature, which is somewhat aligned with the mean flow but contains different local extrema from `trPSI`. We call this tracer `trSST`.

Before examining the K_{OC} results, we first turn to the variance budgets themselves. Figs. 3-9 and 3-10 show the relevant terms in the two-dimensional variance budget (3.17) for `trLAT` and `trPSI`. (The variance budget for `trSST` is very similar to `trLAT` and is not plotted.) Also plotted are the mean tracer concentration $\bar{q}$ and variance $\overline{q'^2}/2$. It is striking how different the variance field is for the different tracers. For `trPSI`, the region of highest variance is along the equator. We presume this is due to the very strong gradients of $\bar{q}$ which are present near the equator; these gradients in streamfunction coincide with the strong quasi-zonal equatorial jets. In contrast, the variance produced by `trLAT` is highest in boundary current regions.

The variance budgets themselves reflect these differences. The variance production and dissipation for `trLAT` are both strongest at the equator, where the variance itself is highest. Likewise, these terms are most intense in the boundary currents for `trPSI`. As we saw in the zonally-averaged budget (Fig. 3-6), production is largely balanced locally by dissipation for both cases. The variance advection (which includes both

triple correlation and mean advection) mostly displays small scale variations on scales below 500 km, with closely neighboring sites of positive and negative contribution. The areas where the advection terms is significant are mostly in boundary currents, the ACC, or near the equator. This means that variance is generally dissipated within 500km, or less, of where it is produced, implying that *on large scales*, the variance budget is approximately local.

The only glaring exception to this local balance is in near the equator for trPSI, where coherent zonal bands of positive and negative values are present. These bands indicate a systematic transfer of variance from a production region to a dissipation region. We note that this transfer is truly a combination of triple correlation and mean variance advection, rather than being due just to one term, although only the net effect is plotted.

There are several reasons to expect somewhat different values of K_{OC} to emerge from calculations using different initial tracers. As mentioned above, the misalignment between trLAT and the mean flow can create additional mixing by the mean flow itself. We expect this effect to be especially strong in western boundary current regions, where the mean flow is nearly perpendicular to trLAT. On the other hand, trPSI contains vanishing gradients that can cause K_{OC} to blow up. This is especially problematic near the equator, where trPSI has several local extrema in close proximity to strong variance dissipation regions. We expect this effect to produce strong maxima in K_{OC} near the equator for trPSI.

We now turn to the maps of K_{OC} themselves. The results for the three tracers are shown in Fig. 3-11 on a logarithmic scale. Despite significant difference in the variance budgets themselves, all three calculations share the following key attributes in K_{OC}:

- Large values ($K_{OC} > 10^4$ m^2 s^{-1}) on the flanks of western boundary currents such as the Gulf Stream and Kuroshio

- Local minima($K_{OC} < 10^3$ m^2 s^{-1}) in the mid-latitude gyres around 45 N / S

- Patterns in the Southern Ocean consistent with Marshall et al. (2006), with
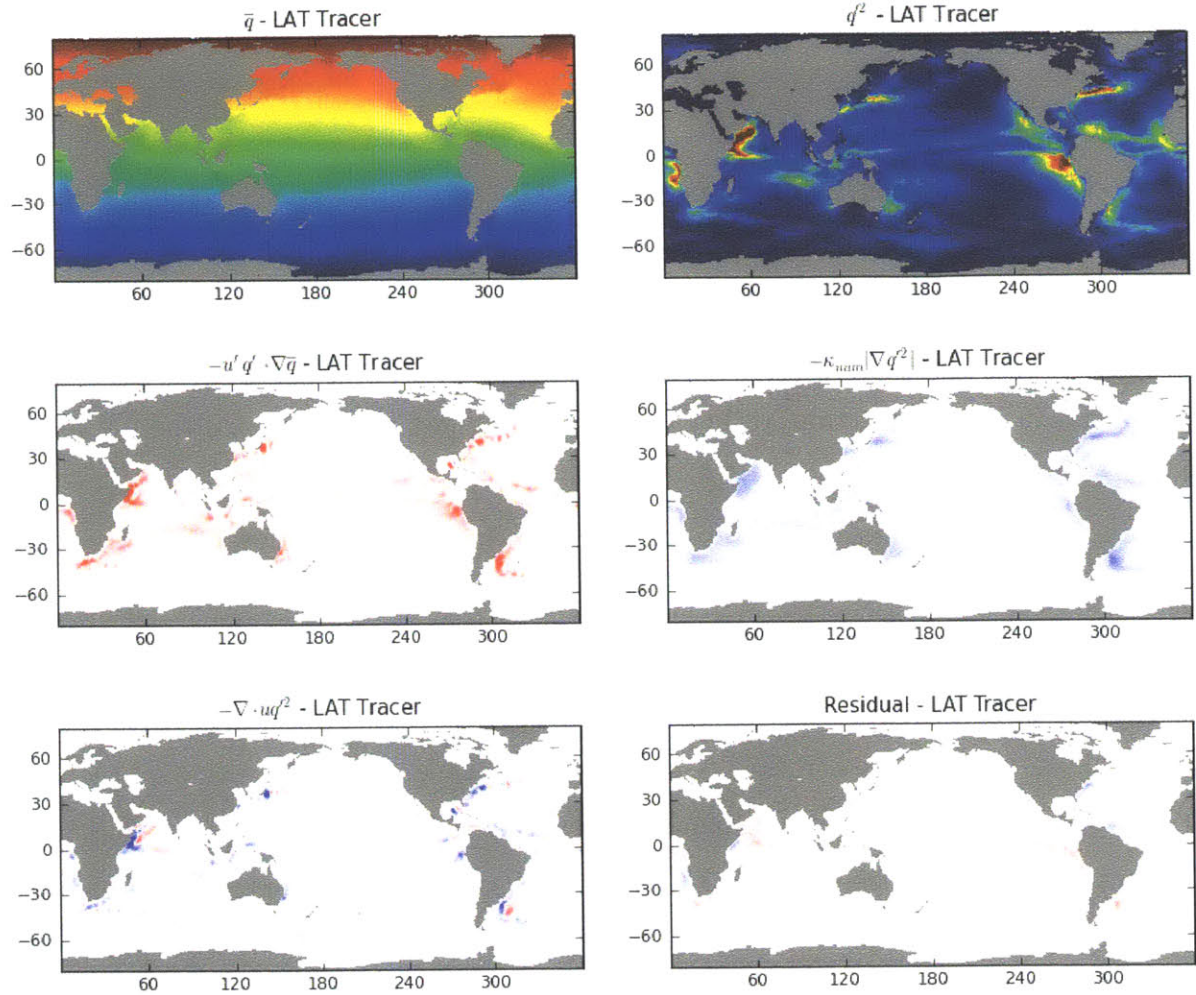
Figure 3-9: Diagnostics of tracer variance from the global trLAT experiments. The top row shows the mean tracer concentration $\overline{q}$ and variance $\overline{q'^2}/2$. The magnitude of the terms is meaningless, since the tracer units themselves are arbitrary. In the bottom four panels, the terms of the variance budget (3.17) are all arranged on the right-side of the equation, so that a positive value acts to locally increase the variance. (he bottom four panels are plotted with the same color scale, with red indicating positive and blue negative. The residual, shown in the bottom right panel, is assumed to correspond to a net tendency. (The tendency was not diagnosed explicitly).
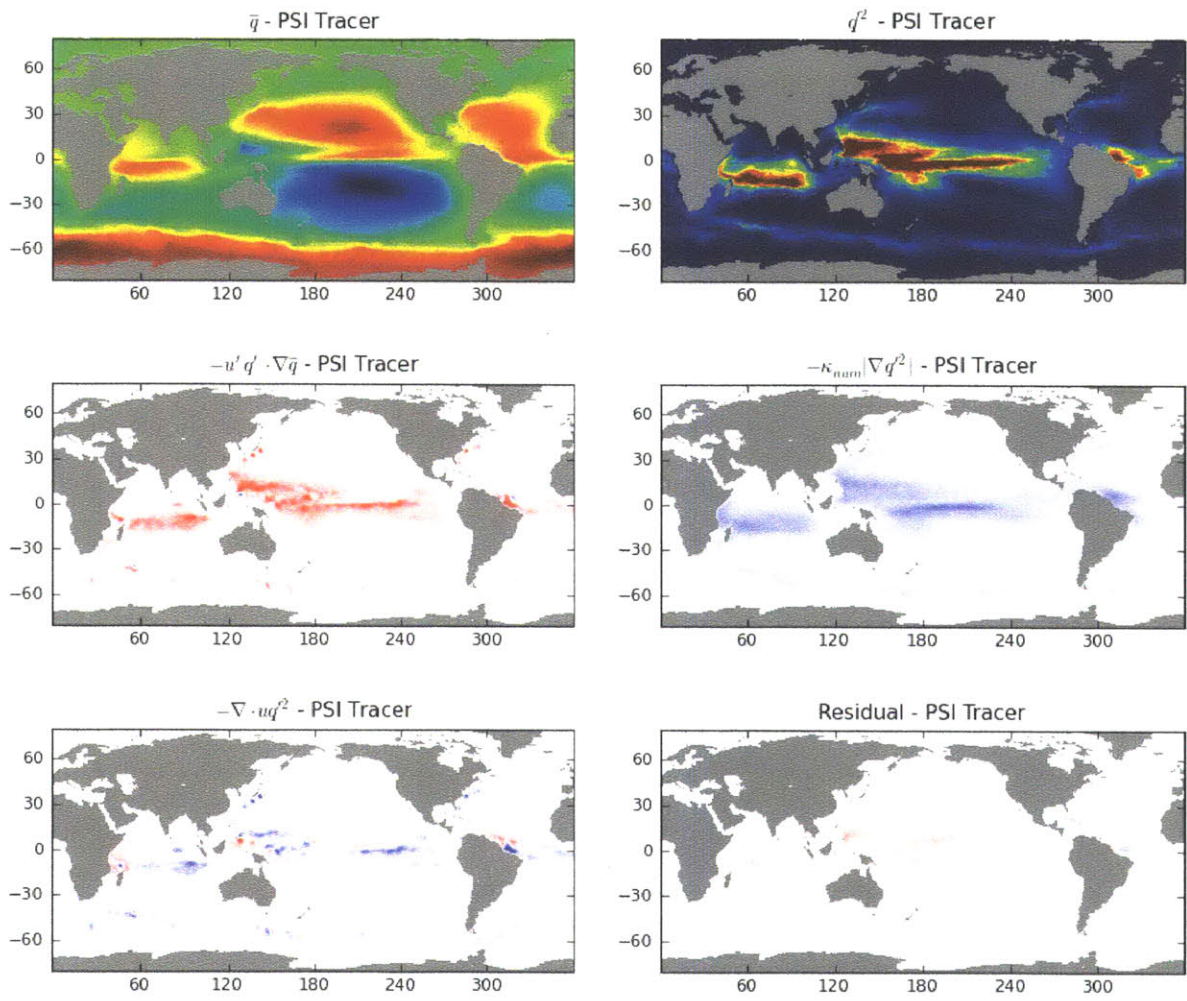
Figure 3-10: Same as Fig. 3-9 but for trPSI.

high values on the northern flank of the ACC and lower values farther south

- Very high values in the tropics, but differing spatial patterns

Many of the apparent differences can be understood in terms of the issues suggested above. Both `trLAT` and `trSST` exhibit high K_{OC} in the western-boundary-current extension regions. `trPSI`, on the other hand, does not have such a pronounced maximum in these regions. We attribute this to the fact that `trPSI` is totally aligned with the currents in these regions, while the others are not. The misalignment leads to strong mixing by the mean flow alone. This conclusion is supported by the experiments with no mean flow, presented in the next subsection.

As also mentioned above, K_{OC} becomes undefined where $|\nabla\overline{q}|^2 = 0$. The latitude tracer avoids this situation better than the other tracers because it contains no pre-existing local extrema. Both the SST and streamfunction tracers, however, contain local maxima to begin with, and these points inevitably are associated with very large values of K_{OC}. To illustrate this effect, Fig. 3-11 includes a contour showing where $|\nabla\overline{q}|$ is equal to 20% of its global mean value, indicating where the background gradients are very weak. There are almost no such areas for the latitude tracer, but there are several large regions for the other tracers. If the variance budget is local in these regions, the large values of K_{OC} truly represent strong mixing. But if the budget is not local, they are misleading. A particularly severe example of the later case occurs in the banded structures near the equator for `trPSI`. We saw in Fig. 3-10 that variance is exported by the advection term from a production region near the equator to a dissipation region just slightly north. Because `trPSI` has strong strong and weak gradients in close proximity in this region, K_{OC}, which is based on a local variance budget, becomes artificially large where the gradient is small. Indeed, from examining maps of $|\nabla\overline{q}|^{-2}$ (not plotted), it becomes clear that this term plays a major role in determining the spatial patterns of K_{OC}.

The upper bound of our diagnosed diffusivities, $O(20,000 \text{ m}^2 \text{ s}^{-1})$, is very large compared to the values used in conventional ocean models. But it is not without precedent. Zhurbas and Oh (2003, 2004) analyzed surface drifter trajectories to asses

(a) $\log_{10}(K_{OC})$ from latitude tracer

(b) $\log_{10}(K_{OC})$ from SST tracer

(c) $\log_{10}(K_{OC})$ from streamfunction tracer
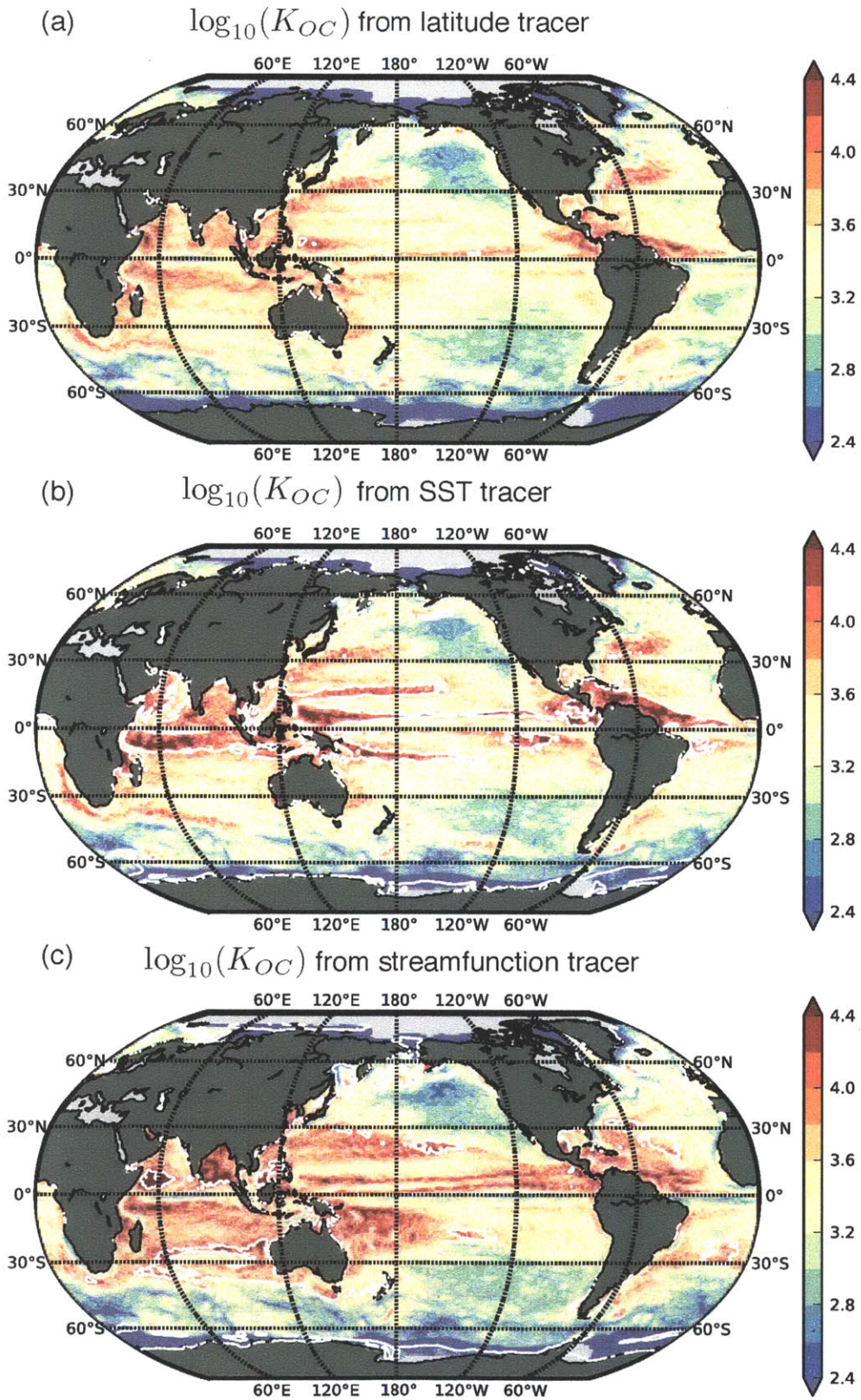
Figure 3-11: Osborn-Cox diffusivity on a logarithmic scale, i.e. $\log_{10}(K_{OC})$. The initial tracer concentrations used were (a) latitude, (b) SST, (c) streamfunction for mean flow. The white contour indicates where $|\nabla \overline{q}|$ is one fifth of its global mean value. See text for details.

Lagrangian diffusivities in the Atlantic and Pacific. They found diffusivities of similar magnitude in the boundary currents and equatorial regions. Overall, their spatial patterns of diffusivity are quite similar to ours as well.

3.4.4 Impact of Mean Flows

The role of the mean flow in determining the spatial pattern of K_{OC} can be assessed by conducting the global experiment with the mean flow set to zero. We show results of these experiments for trLAT and trPSI in Figs. 3-12 and 3-13. As discussed above, these two tracers have very different orientations relative to the mean flow, in particular in the western-boundary-current regions, where trLAT is nearly perpendicular to to the mean flow. trPSI, on the other hand, is always perfectly aligned with the mean flow. The effect of removing the mean flow will be different in each case. By removing the mean flow from the trLAT experiment, we also remove the mixing due to the mean flow itself. Because trPSI is not mixed by the mean flow at all, its' zero-mean-flow experiment is more pure, revealing only the interaction between mean flow and wave propagation envisioned described in Sec. 3.3.2.

Focusing first on trPSI (Fig. 3-12), we note similar patterns of suppression and enhancement to those found in the Pacific channel experiment. (Compare with Fig. 3-5.) We observe strong suppression by the mean flow throughout the ACC. In the tropics where the mean flows becomes westward (same sign as Rossby wave propagation), the presence of the mean flow leads to enhancement which is correlated with the structure of the equatorial jets. Where the equatorial counter-current flows eastward, we observe suppression. In the western boundary currents and their extension jets that flow eastward between the subtropical and subpolar gyres, we observe significant suppression. Just as in the ACC, the combination of eastward flow and westward propagating waves / eddies leads to suppression of mixing. It has been suggested (Bower et al., 1985) that the Gulf Stream creates a mixing barrier near the surface, and our results are consistent with this interpretation.

For the most part, the effects of the mean flow on trLAT are similar, with the same broad patterns of enhancement and suppression. There is a big difference, however,

100

in the western-boundary-current regions. In the core of the Gulf stream, and on the northern flank of the Kuroshio extension, the mean flows clearly suppress mixing, as observed across the region for trPSI. However, for trLAT the addition of the mean flow causes extremely *enhanced* mixing on the southern flanks. We interpret this as mixing caused directly by the mean flow itself, due to the initial misalignment between trLAT and the current.

3.4.5 Composite Map of K_{OC}

In general, it is not obvious whether one of these tracers is the "best" measure of the true mixing rates. Each has advantages and disadvantages. trLAT maintains a stable gradient everywhere, making the diagnostics more robust. The spatial structure of trPSI, on the other hand, is clearly strongly affected by the initial tracer distribution. But trPSI represents only mixing by the eddies, not the mean flow itself. As we have just seen, part of the mixing of trLAT is due to the misalignment of the initial tracer gradient with the mean flow. (trSST is in a way the worst of both worlds, exhibiting both issues.) In short, we feel that the different calculations are robust in different parts of the ocean. Therefore we propose a composite quantity, which we simply call K, as the minimum of the K_{OC} obtained with trLAT and trPSI at each point. By choosing the minimum of the two values, we automatically avoid the points where trPSI is large due to weak initial gradients and where trLAT is strong due to mean-flow induced mixing. K is plotted in Fig. 3-14. We believe that this quantity most accurately represents the true eddy mixing rates in the surface ocean.

3.4.6 Sensitivity to κ

Here we address whether K_{OC} is independent of κ in the same way as K_{eff} was shown to be in Marshall et al. (2006) and the previous section. The factor $|\nabla \overline{q}|^2$, the mean background gradient, is certainly independent of κ, so K_{OC} will be independent of κ if $\overline{|\nabla q'|^2} \sim \kappa^{-1}$. Employing the same set of experiments used to calculate κ_{num}, we calculated the domain-averaged value of $\overline{|\nabla q'|^2}$ for a range of κ. The results,
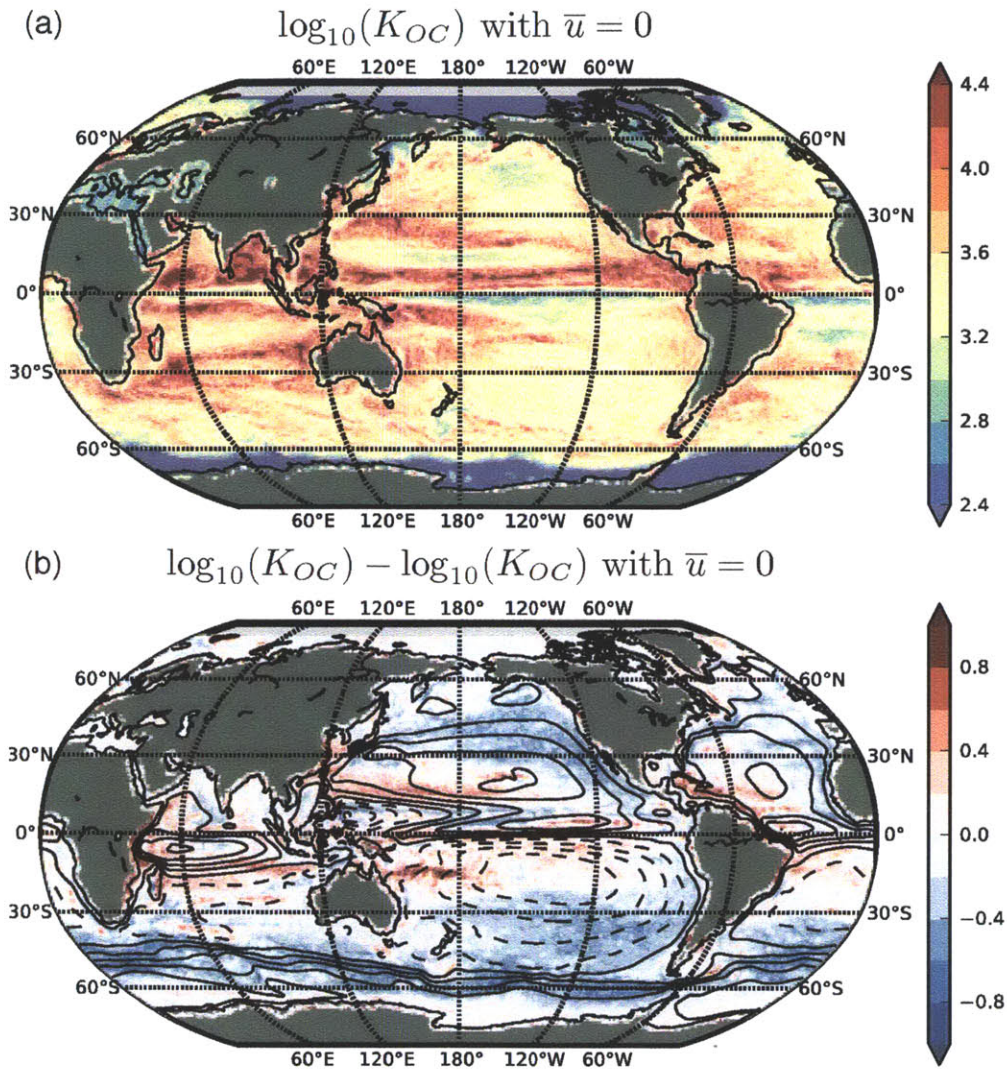
Figure 3-12: (a) Osborn-Cox diffusivity on a logarithmic scale for the latitude-tracer experiment with the mean flow set to zero for `trLAT`. (b) The ratio between K_{OC} with and without the mean flow. The black contours are the streamfunction of the mean flow, indicating the position of mean currents. The solid contours surround regions of large-scale clockwise flow while the dashed contours show counterclockwise flow.

(a) $\log_{10}(K_{OC})$ with $\overline{u} = 0$

(b) $\log_{10}(K_{OC}) - \log_{10}(K_{OC})$ with $\overline{u} = 0$
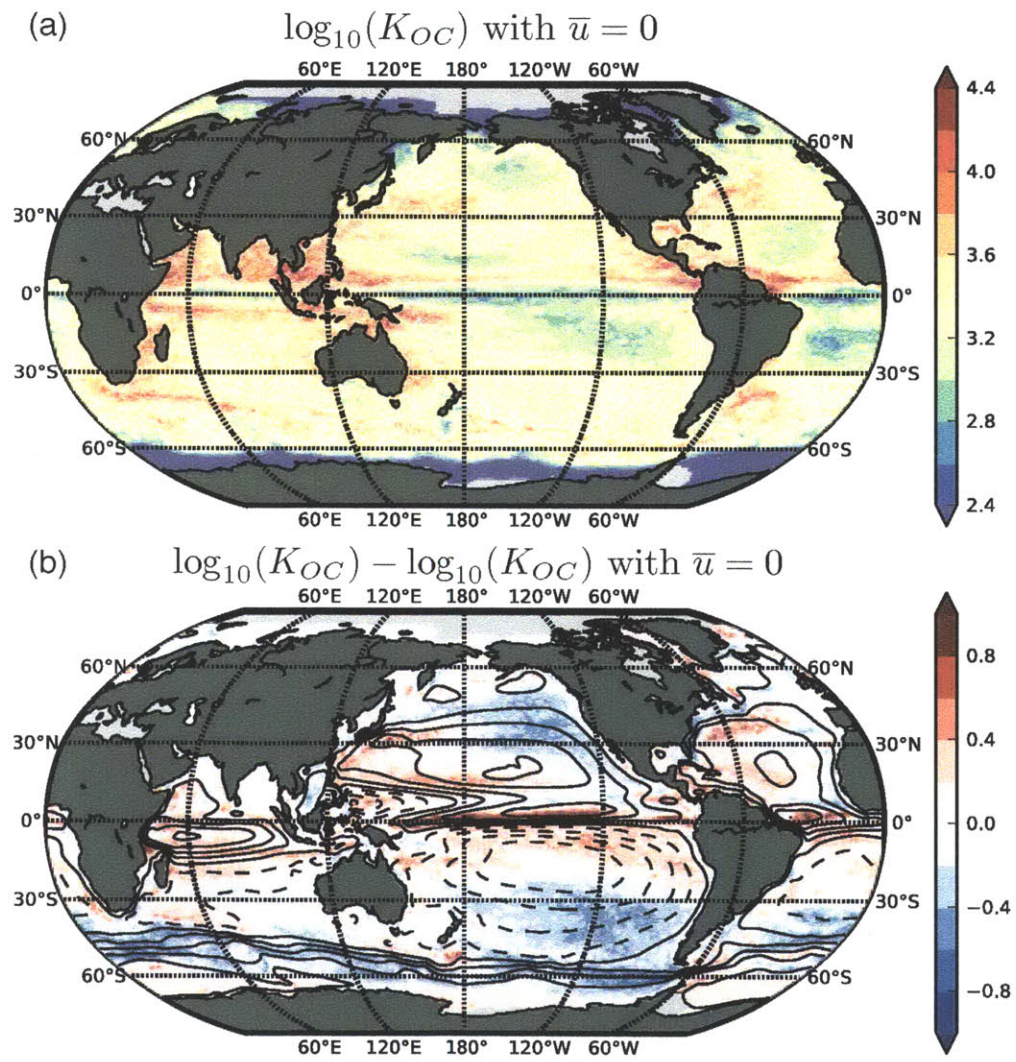
Figure 3-13: Same as Fig. 3-13 but for `trLAT`.
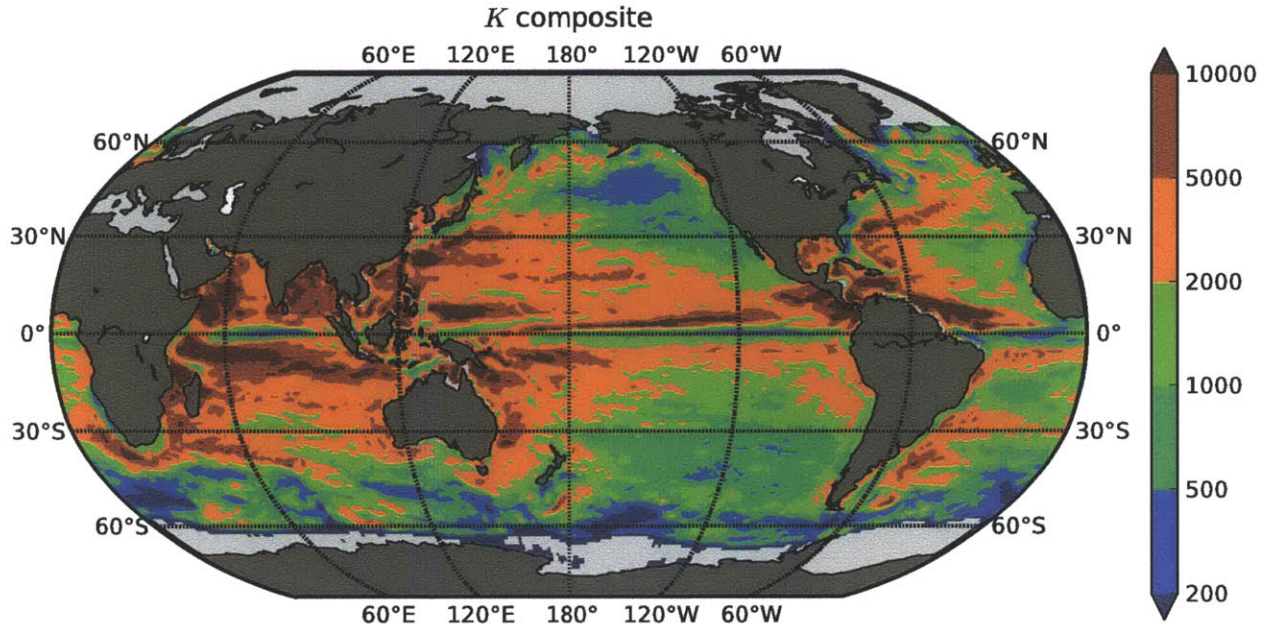
Figure 3-14: Composite value of K produced by taking the minimum K_{OC} produced by trLAT and trPSI. See text for discussion.

shown in Fig. 3-15 on a logarithmic scale, do indeed show that this factor is inversely proportional to κ, with power-law relationship close to -1. A linear fit of the points in Fig. 3-15 reveals that, actually, $\overline{|\nabla q'|^2} \propto \kappa^{-0.8}$. The departure of the exponent from -1 means that K_{OC} does depend weakly on κ: specifically, that $K_{OC} \propto \kappa^{-0.2}$

Measurements of the true background diffusivity in the ocean on scales of 1-10 km have been estimated by Ledwell et al. (1998) from deliberate tracer release experiments. Based on observations of tracer filament width, they concluded that $\kappa \simeq 2$ m^2 s^{-1} at 300 m depth in the North Atlantic. This is significantly less than the $\kappa_{num} = 66$ m^2 s^{-1} value we used. Assuming the $\kappa^{-0.2}$ dependence holds down to such low values of κ, we can extrapolate what value of K_{OC} would result from to employing $\kappa \simeq 2$ m^2 s^{-1}. Since $(2/66)^{0.2} = 0.50$, we conclude that our estimates could be off (too large) by a factor of 2. It seems likely that small scale mixing processes contributing to κ are stronger at the surface, where mechanical forcing and turbulence are much stronger than at 300 m depth. Therefore we consider the factor of 2 an upper bound.
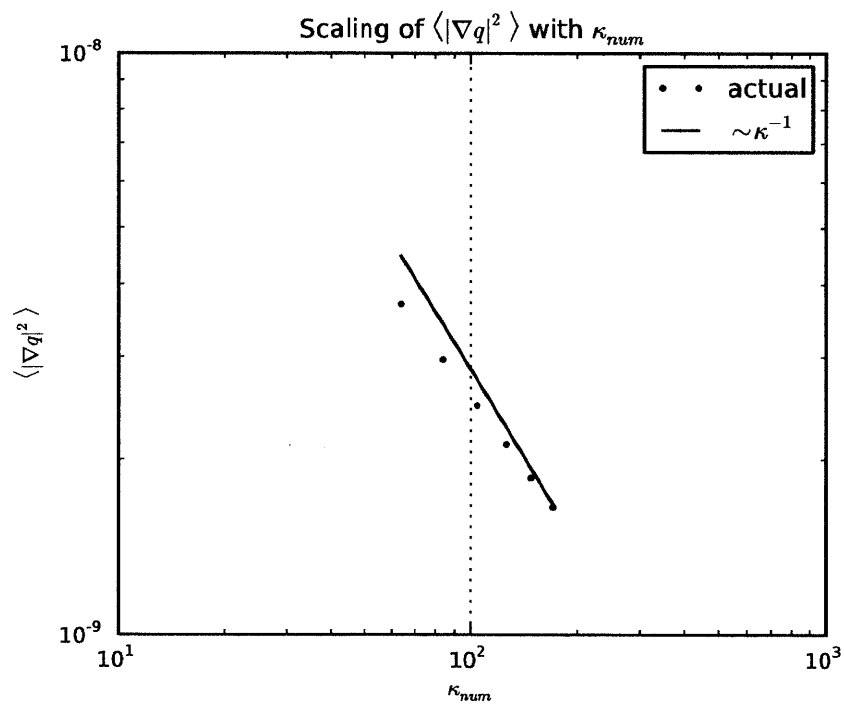
Figure 3-15: Relationship between κ_{num} and κ if $\overline{|\nabla q'|^2}$s diagnosed for six different values of κ. The solid line represents a -1 power law dependence

3.5 The Eddy Stress

The mixing rates diagnosed in this work have various implications for transport in the ocean. Most directly, we can expect that they describe the rates of mixing of heat, salt, and other tracers in the ocean surface layer. (This was the application envisioned by Holloway (1986).) Here we focus on a slightly more subtle application: estimating the near-surface eddy forcing of the mean flow due to the eddy potential-vorticity (PV) flux. This forcing can be expressed as an eddy stress. Although several assumptions must be made to connect our K_{OC} diagnostics with the eddy stress, we see it as a worthwhile step. Eddy PV fluxes can theoretically exert a strong forcing on the ocean circulation, but they are nearly impossible to measure directly on a large scale. Our estimates of K_{OC} based on satellite observations offer an opportunity to infer this forcing in a new way.

Our starting point for understanding how eddies influence the mean flow is the transformed-Eulerian-mean (TEM) form of the planetary-geostrophic momentum equations (Andrews and McIntyre, 1976; Andrews et al., 1987; Treguier et al., 1997; Plumb and Ferrari, 2005; Ferreira et al., 2005; Zhao and Vallis, 2008; Marshall et al., 2012)

$$f\hat{z} \times \boldsymbol{v}_{res} = -\frac{1}{\rho_0}\nabla\overline{p} + \frac{1}{\rho_0}\frac{\partial \boldsymbol{\tau}_w}{\partial z} - \hat{z} \times \overline{\boldsymbol{v}'q_p'} \tag{3.30}$$

where $\boldsymbol{\tau}_w$ is the mean wind stress, $\boldsymbol{v}_{res}$ is the so-called *residual* velocity (which includes the steady flow and also the "eddy-induced" circulation), and $\overline{\boldsymbol{v}'q_p'}$ is the eddy flux of quasi-geostrophic potential vorticity (QGPV). (See references above for full discussion of TEM theory, and especially Treguier et al. (1997) and Plumb and Ferrari (2005) for discussion of the applicability of quasi-geostrophic formulas on a planetary scale. Also see Greatbatch (1998) for a discussion of the connection to isopycnal coordinates.) This framework is appropriate for the large-scale flow in circumstances where standard quasi-geostrophic scaling assumptions apply: low Rossby number (i.e. strong rotation) and high Richardson number (i.e. strong stratification). A similar expression can be derived when the stratification is weak (e.g. in the mixed layer), but the formula is much more complicated (Plumb and Ferrari, 2005).

In this framework, the eddy forcing of the mean flow is subsumed into the eddy flux term $\overline{v'q'_p}$. One interpretation of (3.30) is that the QGPV flux essentially exerts a force on the fluid, which is balanced by a Coriolis force on the eddy-induced velocity v^* (which is a part of v_{res}), such that

$$-fv^* = \overline{v'q'_p} \ . \tag{3.31}$$

The eddy QGPV flux in two dimensions can also be interpreted as the divergence of an eddy stress tensor (Plumb, 1986). The contribution of the eddy QPGV flux on ocean circulation was first envisioned by Welander (1973), who concluded that eddies would induce a frictional force that would act to increase the gulf stream transport. Many subsequent eddy-closure theories have evolved based on the QGPV flux (Green, 1970; Stone, 1972; Marshall, 1981; Killworth, 1997; Treguier et al., 1997, to name a few). Here we are interested not so much on *parameterizing* the effect of eddies in an ocean model but *inferring* their effect from observations, in particular, from our estimates of K_{OC} in conjunction with mean hydrography.

The fundamental *ansatz* of this section is that the near-surface QGPV flux can be estimated using K, the composite of K_{OC} obtain using multiple tracers, in conjunction with with background gradient, such that

$$\overline{v'q'_p} = -K\nabla\overline{q}_p \ . \tag{3.32}$$

In light of how K_{OC} was calculated, this closure seems much more justified than a closure based on the buoyancy flux, as in the Gent and McWilliams (1990) parameterization; QGPV is a quasi-conserved tracer that is advected by the geostrophic flow in the 2D horizontal plane, just like the passive tracers we used to diagnose K_{OC}. Also, the vertical flux of QGPV is not important, while the vertical flux of buoyancy is. Furthermore, since K_{OC} captures only irreversible mixing, it automatically eliminates the divergent QGPV fluxes that do not contribute to the mean circulation (Marshall and Shutts, 1981).

The QGPV gradient is given by

$$\nabla \overline{q}_p = \underbrace{\beta \hat{\boldsymbol{y}} + \nabla \overline{\zeta}}_{\text{vorticity}} - \underbrace{f \frac{\partial \boldsymbol{s}}{\partial z}}_{\text{stretching}} \quad . \tag{3.33}$$

where $\overline{\zeta} = \partial \overline{v}/\partial x - \partial \overline{u}/\partial y$ is the background relative vorticity and $\boldsymbol{s} = -\nabla \overline{b}(\partial \overline{b}/\partial z)^{-1}$ is the vector isopycnal slope. As indicated, part of the QGPV gradient is due to the vorticity gradient (including the planetary β), while part is due to the mean hydrographic gradients, i.e. the "vortex stretching" term. We can formalize this distinction by writing

$$\nabla \overline{q}_p = \boldsymbol{\beta}^* + \nabla \overline{q}_s \tag{3.34}$$

where $\boldsymbol{\beta}^* = \beta \hat{\boldsymbol{y}} + \nabla \overline{\zeta}$ is the vorticity gradient and $\nabla \overline{q}_s = -f \partial \boldsymbol{s}/\partial z$ is the stretching gradient. Carrying this separation over to the flux and using the down-gradient closure (3.32), we can write

$$\overline{\boldsymbol{v}' q_p'} = (\overline{\boldsymbol{v}' q_p'})_\beta + (\overline{\boldsymbol{v}' q_p'})_s \tag{3.35}$$

where

$$(\overline{\boldsymbol{v}' q_p'})_\beta = -K \boldsymbol{\beta}^* , \tag{3.36}$$

$$(\overline{\boldsymbol{v}' q_p'})_s = -K \nabla \overline{q}_s . \tag{3.37}$$

We shall treat these two components separately.

Focusing first on the vorticity term, using (3.36) in (3.31), we can estimate the eddy-induced velocity due to vorticity mixing as

$$\boldsymbol{v}_\beta^* = f^{-1} K (\beta \hat{\boldsymbol{y}} + \nabla \overline{\zeta}) . \tag{3.38}$$

(This is equivalent to estimating the eddy-induced force, since this force is balanced by a Coriolis force on $\boldsymbol{v}^*$.) We used the ECCO atlas to estimate $\nabla \overline{\zeta}$ and evaluated (3.38) at 200 m depth. This depth was chosen because it is below the mixed layer

in most places and consequently the dynamics can reasonably be described by quasi-geostophy, but it is close enough to the surface that K can still be expected to describe mixing rates at this depth. In Fig. 3-16 we plot three quantities $\beta + \partial \bar{\zeta}/\partial y$ (the relative vorticity gradient), v_β^* as inferred by (3.38), and the mean $\bar{v}$ for comparison. (We did not plot the zonal vorticity gradient or u_{vort}^* because these quantities are smaller by an order of magnitude compared to their meridional counterparts.) This figure shows that the vorticity gradient is dominated by β, with the relative vorticity gradient only acting to slightly modify the contours of the planetary vorticity. (This holds even for the surface flow, except at the equator.) Therefore v_β^* reflects the sign of β, but its magnitude is modulated strongly by K. This leads to significant eddy-driven velocities mainly in the tropics, where v_β^* points away from the equator in both hemispheres. One possible interpretation of $(\overline{v'q_p'})_\beta$ near the equator is that it represents the forcing due to the Reynolds-stress divergence generated by tropical instability waves stirring the planetary vorticity gradient.

We now turn to $(\overline{v'q_p'})_s$. It can be shown that this term represents the vertical divergence of an eddy stress, related to the interfacial form stress exerted by one isopycnal layer on another (see Plumb, 1986; Marshall et al., 2012, for derivations and expressions for the full eddy stress) Because it is related to the vortex-stretching term in the PV equation, this term cannot exert a net force on the water column, but rather must vanish in a vertical integral (Marshall, 1981). This constraint can be achieved by imposing that $s \rightarrow 0$ at $z = 0$. (A similar requirement exists for the bottom, but we are concerned just with the surface here.) We can then define a bulk gradient due to the vortex stretching term (which we shall call ∇Q_s) for the surface layer, giving

$$\nabla Q_s = \frac{1}{h} \int_{-h}^{0} -f \frac{\partial s}{\partial z} dz = f h^{-1} s|_{-h} \tag{3.39}$$

where h is the depth of the surface layer and $s|_{-h}$ indicates the slope at the base of the layer. In the limit of $h \rightarrow 0$, this surface layer becomes identical to the δ-function "PV sheet" defined by Bretherton (1966), and the s-term is identical to the surface buoyancy gradient.
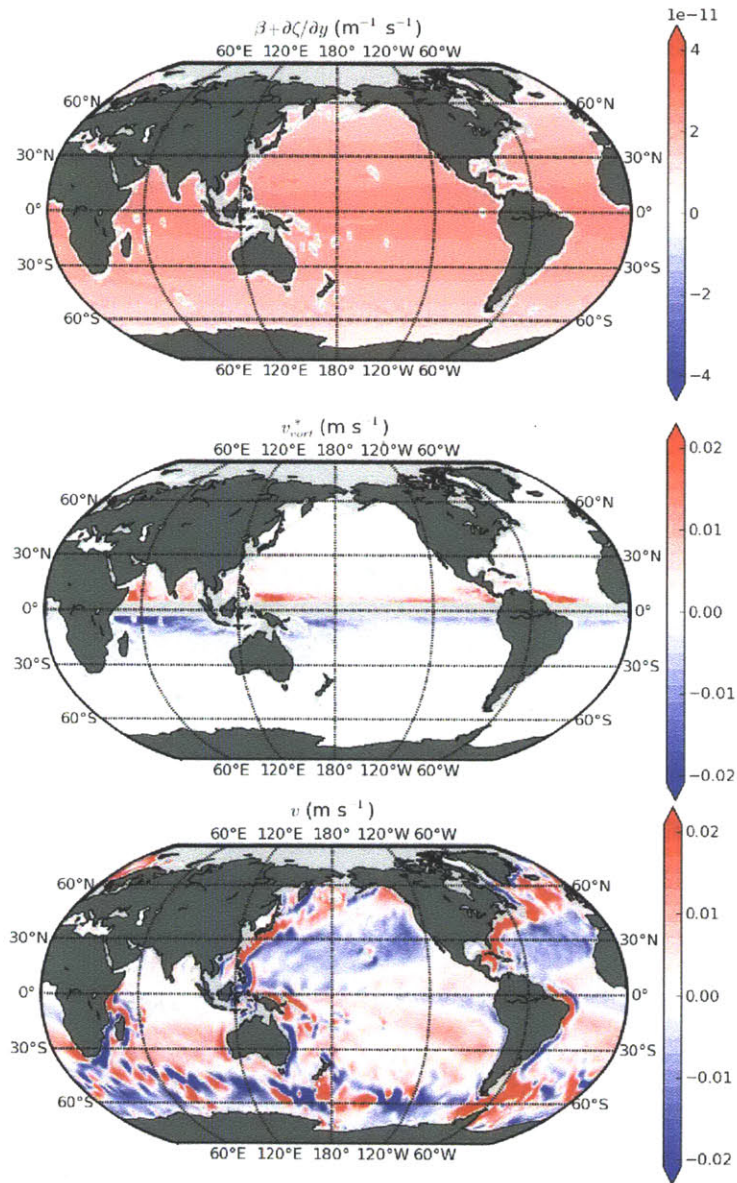
Figure 3-16: Top: $\beta + \partial\overline{\zeta}/\partial y$ at 200 m depth. Middle: v_β^* as inferred from the gradient by (3.38) (the region near the equator is masked because $f^{-1} \to \infty$ there). Bottom: mean $\overline{v}$ for comparison.

The eddy-induced transport in the surface layer due to the vortex stretching term can now be written as

$$\boldsymbol{V}^* = \int_{-h}^{0} \boldsymbol{v}^* dz = f^{-1} \int_{-h}^{0} (\overline{\boldsymbol{v}'q_p'})_s dz = f^{-1} K \nabla s|_{-h} \qquad (3.40)$$

Here we have assumed that K, which we derived from the surface flow, is an appropriate bulk diffusivity for a the entire surface layer. If the eddy kinetic energy and the mean flow do not vary strongly over h, then we expect this assumption to be valid. Just as the Ekman transport is driven by a wind stress at the surface, the eddy transport in the surface layer can now be viewed as driven by an eddy stress at the bottom of the layer (Rhines, 1979; Johnson and Bryden, 1989; Ferreira et al., 2005). The relation between the eddy stress $\boldsymbol{\tau}_e$ and the transport is

$$\boldsymbol{\tau}_e = \rho_0 f \hat{\boldsymbol{z}} \times \boldsymbol{V}^* \qquad (3.41)$$

Using (3.40) in conjunction with (3.32), we can write the zonal and meridional components as

$$\tau_e^x = \rho_0 K f s^y|_{-h}$$

$$\tau_e^y = -\rho_0 K f s^x|_{-h} \qquad (3.42)$$

where s^x and s^y are the zonal and meridional isopycnal slopes. If K is constant, the transport induced by this stress is equivalent to the transport produced by the Gent and McWilliams (1990) eddy parameterization.

We used the ECCO atlas (Wunsch and Heimbach, 2009) to compute $\nabla \overline{Q}_p$ and estimate $\boldsymbol{\tau}_e$ at 200 m depth. We computed the potential density referenced to the surface and used this density field to calculate isopycnal slopes s^x and s^y. We then evaluated(3.39) to find ∇Q_s. The resulting gradients are plotted in Fig. 3-17. From this figure it is evident that the β-effect is relatively weak in mid-latitudes, since $\beta = O(10^{-11} \text{ m}^{-1} \text{ s}^{-1})$, compared to the full gradient, which frequently exceeds 10^{-10} m^{-1} s^{-1}.
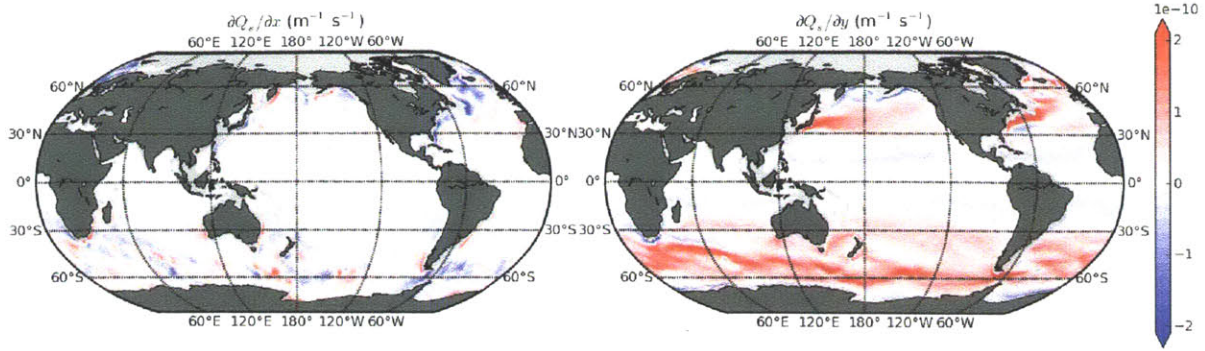
Figure 3-17: Surface layer bulk QGPV gradient ∇Q_s, computed from the ECCO atlas according to (3.39).

Next we calculate the eddy stress using (3.42). The result is plotted in Fig. 3-18. For comparison, the figure also shows the mean observed surface wind stress from the Surface Climatology of Ocean Winds (Risien and Chelton, 2008). We concentrate our discussion on the zonal component of the stress, which is the dominant one for both the winds and eddies. The most striking feature of these maps is how the zonal wind and eddy stress have the same broad pattens, with westward wind / eddy stress in the tropics and eastward wind / eddy stress at higher latitudes. However, in general the eddy stress is lesser in magnitude than the wind stress.

In the Southern Ocean, the eddy stress plays an important role in the momentum balance by moving momentum down the water column, where the wind stress input can eventually be balanced by bottom topographic form stress (Johnson and Bryden, 1989; Marshall et al., 1993; Ferreira et al., 2005). Indeed we observe a band of positive τ_e^x across the Southern Ocean, validating this idea. However we do not see a complete balance between eddy stress and wind stress in the Southern Ocean–instead, the wind stress is greater. This could be related to the fact that eddy mixing is known to intensify with depth in the Southern Ocean (Smith and Marshall, 2009; Abernathey et al., 2010). The assumption that K does not vary greatly over the top 200 m in the Southern Ocean may not be valid; the results of Chapter 1 indicate that this may in fact be the case (see Fig. 2-4).

Our results indicate that the eddy stress plays a significant role in the momentum
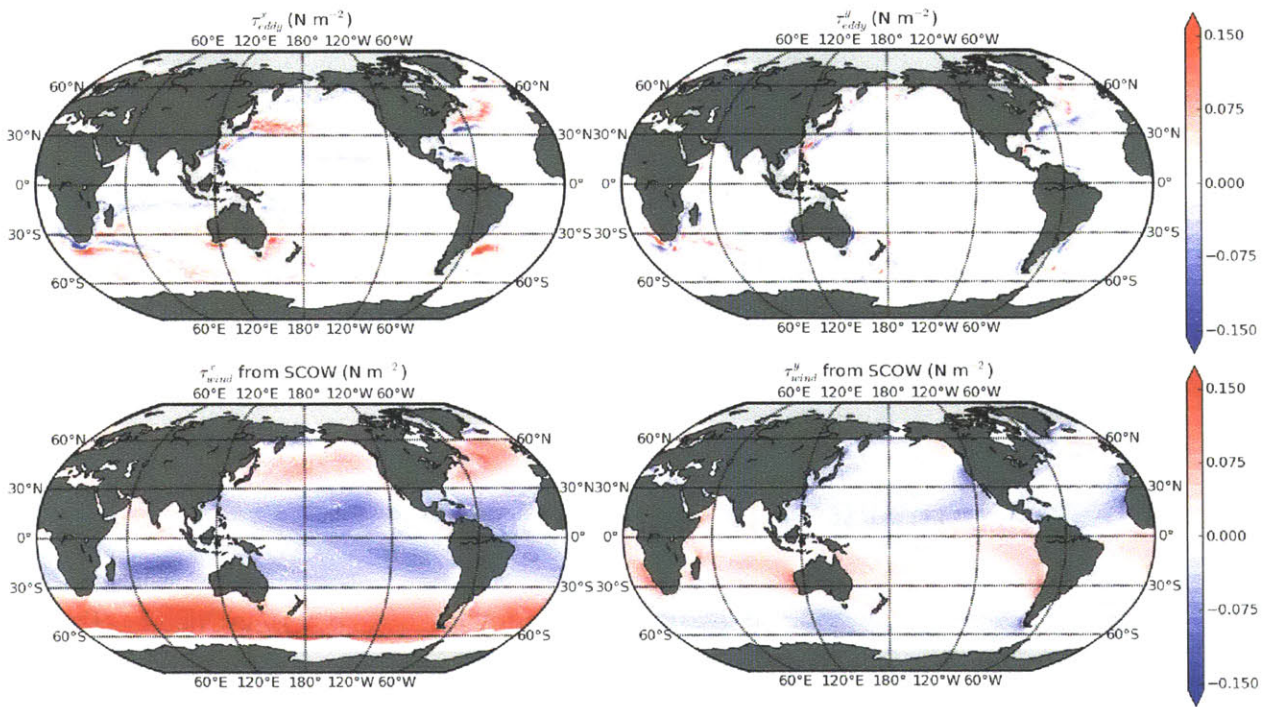
Figure 3-18: Top: zonal and meridional eddy stress $\boldsymbol{\tau}_e$ at 200 m dpeth, as calculated from (3.42). Bottom: Surface wind stress from the Surface Climatology of Ocean Winds (Risien and Chelton, 2008).

balance also outside the Southern Ocean. The main difference between the other ocean basins and the Southern Ocean is that eddy stresses are not necessarily *required* for the momentum balance, because means zonal pressure gradients can exists at all depths Hughes and de Cuevas (2001). However, large areas of positive eddy stresses are clearly visible in western boundary currents region, with magnitudes comparable to the local wind stress. Negative bands of eddy stress in the tropics, while quite a bit weaker the than the westward wind stress, suggest a partial balance between in wind and eddy stress also in the tropics.

There will be an eddy-induced upwelling due to the divergence of the eddy-induced transport in the surface layer, equal to $w^* = -\nabla \cdot V^*$. We have not calculated w^* explicitly, because it involves yet another derivative of an already noisy field. But we can deduce from the general structure of τ_e that the overall effect of this upwelling will be a partial cancellation of the Ekman pumping in the upper ocean by eddy-induced upwelling.

3.6 Summary and Conclusions

We have constructed a global map of eddy mixing rates based by using satellite observations to simulate the evolutions of passive tracers. We began in a "zonalized" version of the east Pacific, where we computed effective diffusivity as functions of latitude. We found surprisingly high mixing rates (> 5000 m^2 s^{-1}) in the tropics. We saw that the zonal mean flow acts to suppress mixing at high latitudes, where the flow is eastward, as previous studies in the ACC have already confirmed. However, between 30° N and S, where the mean flow is westward, the presence of a mean flow actually *enhances* mixing rates. We suggested that this behavior arises due to the westward phase speed of eddies and waves. When the mean flow and the phase speed have the same sign, as in low latitudes, the mean flow enhances mixing. When they have the opposite sign, the mean flow suppresses mixing. Near the equator, where the mean flow consists of zonal jets of alternating sign, we saw complex patterns of mixing and suppression.

114

We then introduced the Osborn-Cox diffusivity K_{OC}, which arises from considering the the tracer variance budget. We showed how K_{OC} captures the part of the cross-gradient eddy flux that is locally balanced by dissipation. When the variance budget is non-local and non-steady, there are additional fluxes not captured by K_{OC}. However, we showed, both in the Pacific channel model and later in global simulations, that these effects are generally small; the variance budget contains non-local fluxes on scales of $O(500 \text{ km})$, but the overall balance between variance production and dissipation is well captured by K_{OC}

We calculated K_{OC} from global simulations using three different initial tracers: one aligned with latitude, one proportional to the streamfunction of the mean flow, and one proportional to SST. Despite significant differences in the variance budget for these tracers, the resulting K_{OC} values showed similar large-scale structure and magnitudes. Differences arose in regions with weak initial background tracer gradient and in regions where the initial tracer aligned strongly perpendicular to the mean flow. We defined a composite K as the minimum value of these three calculations that avoids the problem areas of the particular tracers. We also performed global experiments with the mean flow set to zero—these confirmed the general picture of mean-flow suppression at high latitudes and mean-flow enhancement at low latitudes.

As a final step, we applied these mixing rates to infer the eddy stress by estimating the QGPV flux in the surface layer. We showed that the dominant part of this QGPV can be described as an eddy stress. The eddy stress was shown to generally have the same sign as the wind stress, but a lesser magnitude. This indicates a partial balance between the eddy stress and wind stress. We speculated that this leads to a partial cancellation between the Ekman pumping and the eddy-induced vertical velocity w^* near the surface.

The vertical velocity near the surface is particularly important to model correctly when attempting to assess the role of the ocean in climate change, because the vertical velocities help propagate surface anomalies into the interior. Anthropogenic CO_2 in the atmosphere is a very long-lived chemical species; its only significant sink is uptake by the land and ocean (an D. Qin et al., 2007; Archer et al., 1997). Therefore, the

amount of greenhouse-induced warming we experience in the future depends directly on the rate of uptake by the ocean. Le Quéré et al. (2009) recently suggested that the oceanic carbon sink may be slowing. But none of the models used to address these questions resolve mesoscale eddies, and instead commonly employ the Gent and McWilliams (1990) framework with spatially constant eddy mixing rates. As a result, it is possible that these models underestimate the near-surface eddy stress and consequently display unrealistically weak values of w^*.

As a consequence of increased radiative forcing from anthropogenic emissions, the near-surface atmosphere has warmed considerably (an D. Qin et al., 2007), which is causing the ocean to warm as well. Levitus et al. (2998) estimate that the ocean has gained about 1.5×10^{23} J of heat since 1950. Climate models display a wide spread in rates of oceanic heat uptake; which is often attributed to different amounts of "vertical mixing" among models (Sokolov et al., 2003). Different rates of heat uptake consequently imply very different climate sensitivities (Forest et al., 2002), making the issue a central one in the problem of anthropogenic climate change. But the paradigm of "vertical mixing" as the cause of ocean heat uptake has severe limitations; it implies that heat is literally diffused into the ocean, rather than advected. Our results suggest that a proper representation of the eddy stress, by using realistic eddy mixing rates, could potentially affect the rate of ocean heat uptake in climate models.

The K_{OC} diagnostic has proven to be a very useful tool for assessing mesoscale mixing by ocean eddies. Several questions remain, however, regarding its implementation and interpretation. For eddy diffusivity to be a useful concept, it should be independent of the tracer distribution in question, expressing a fundamental property of the velocity field itself. While the broad patterns of K_{OC} were the same for three different tracers, there were nevertheless regions with significant differences due to vanishing of the background gradients. One possible way to resolve this issue would be to compare K_{OC} with Lagrangian diagnostics of mixing such as two-particle diffusivity (LaCasce, 2008; Klocker et al., 2011b); this is an obvious course for future research. A complimentary approach would be to attempt to diagnose **K** in its full tensor form using multiple tracers, as done by (Plumb and Mahlman, 1987). Finally,

116

an understanding of the vertical dependence of mixing is a crucial ingredient for inferring v^* away from the surface. Indeed, the validity of applying K_{OC} to infer $\overline{v'q'_p}$ begs to be tested in an eddy-resolving model. Despite these challenges, we hope our study has helped advance understanding of the global geography of eddy mixing rates.

Chapter 4

The Dependence of Southern Ocean Meridional Overturning on Wind Stress

4.1 Introduction

Changes in wind stress over the Southern Ocean may be responsible for modulating the strength of the global meridional overturning circulation (MOC) (Toggweiler, 2009). Such wind-induced changes in the MOC could help regulate glacial-interglacial cycles by venting CO_2 from the deep ocean to the atmosphere (Toggweiler and Russell, 2008; Anderson et al., 2009; Marshall and Speer, 2011). The mechanism could also play an important role in future climate change; the westerlies appear to be shifting south due to greenhouse gas emissions and ozone depletion, (Thompson and Wallace, 2000; Marshall, 2003; Polvani et al., 2011) and Toggweiler and Russell (2008) hypothesize that in response the MOC will strengthen. But by how much? To what extent is the Southern Ocean MOC controlled by the winds?

Since Johnson and Bryden (1989) we have recognized the existence of an eddy-driven overturning circulation in the Southern Ocean potentially large enough to completely cancel the wind-driven Ekman overturning. The actual MOC is the small

residual between these two opposing circulations. Work by Toggweiler and Samuels (1998), Speer et al. (2000) and Marshall and Radko (2003, hereafter MR) showed that, for realistically weak values of interior diapycnal mixing, the residual overturning transport in the subsurface Southern Ocean must proceed along mean isopycnal surfaces. The residual circulation can cross isopycnals in the surface diabatic layer, where cross-isopycnal advection can be balanced by direct diabatic forcing from the atmosphere (Marshall, 1997). Therefore, from a diagnostic point of view, the strength and sense of the MOC can be inferred from surface buoyancy flux data, as done by Speer et al. (2000) and Karsten and Marshall (2002a), independently of the wind stress. This thermodynamic perspective also implies that the MOC is sensitive to surface buoyancy fluxes, as hypothesized by Watson and Naveira Garabato (2006) or Badin and Williams (2010). Our goal here is to study the relationship between wind stress, overturning circulation, and surface buoyancy flux in a model that explicitly resolves mesoscale eddies, bypassing the need for any *a priori* assumptions about the eddy response.

On a related note, it is well established that coarse-resolution ocean models do not accurately simulate the response of the Southern Ocean overturning to changes in wind stress forcing when compared with eddy-resolving models. This is true of both realistic models (Hallberg and Gnanadesikan, 2006; Farneti et al., 2011) and models with simplified geometry and forcing (Henning and Vallis, 2005). In general, models that permit eddies seem *less sensitive* to changes in wind, whether the focus is the overturning circulation (as in the above works), the zonal transport (Hutchinson et al., 2010), or the transport of tracers such as anthropogenic carbon (Marshall et al., manuscript in preparation). Most of these results are ultimately due to compensation between the wind- and eddy-driven overturning circulations, which is more complete when mesoscale eddies are explicitly resolved rather than parameterized. The lack of a robust parameterization for mesoscale eddies is indicative of our incomplete understanding of the nature of eddy-driven circulations. Most recently, Viebahn and Eden (2010) studied the sensitivity of the residual MOC to the wind in an idealized model and found that changes in eddy kinetic energy and eddy diffusivity play a

central role in determining how the compensation occurs.

Our goal in this study is to further explore the physical mechanisms that determine the sensitivity of the residual MOC to changes in wind forcing. In particular, there are two questions not previously addressed that we wish to pursue here. First is the influence of the boundary condition for buoyancy. Second, we wish to develop a simple theory based on physical principles capable of explaining the MOC sensitivity. To study these issues, we reduce the system to its essential elements: an Ekman-driven and an eddy-driven circulation in a zonally-symmetric channel with buoyancy forcing at the surface. This system was studied analytically by MR who invoked a closure for the eddies, but here we realize it as a high-resolution numerical model. The strength of the Ekman circulation obviously depends linearly on the winds; the strength of the eddy-driven circulation is determined by the geostrophic-turbulent dynamics of the model. We vary the strength of the wind stress and diagnose the steady-state residual overturning circulation.

We find that increased eddy circulation does generally compensate for increased Ekman circulation under stronger winds. However, the degree of compensation depends on the surface boundary conditions. When the surface heat fluxes are held fixed, the residual MOC strength is relatively insensitive to the winds. With an interactive heat flux, we recover the results of Viebahn and Eden (2010): a residual MOC which increases weakly with the winds and whose sensitivity is set primarily by changes in eddy diffusivity. We develop a scaling theory for the eddy diffusivity dependence on the wind and apply this scaling to reconstruct the eddy response. This method yields a closed theory for the sensitivity of the residual MOC which, despite many approximations, shows encouraging agreement with the results from the numerical model.

Section 2 describes the model setup, a reference solution, and the basic experimental results under differing values of wind stress. In section 3, we analyze the results in terms of the buoyancy budget and discuss the constraints imposed by the surface boundary condition for buoyancy. Section 4 describes a framework for understanding the MOC changes in terms of changes in Ekman circulation, isopycnal

121

slope, and eddy diffusivity. Our scaling for the eddy diffusivity and the resulting MOC sensitivity estimates are then presented. We summarize the results and discuss their connection with the real ocean in section 5.

4.2 Experiments with Numerical Model

4.2.1 Modeling Philosophy

The Southern Ocean is dominated by the Antarctic Circumpolar Current (ACC), a strong eastward flow in thermal-wind balance with the strong density front separating polar from tropical waters (Rintoul et al., 2001). This flow circumnavigates the globe and connects back on itself, inspiring a comparison with the large-scale atmospheric jets (Thompson, 2008). Strong atmospheric westerly winds blow over the surface, driving an equatorward Ekman flow. The surface buoyancy flux, a combination of radiative, latent, and sensible heat fluxes as well as freshwater fluxes from evaporation, precipitation and ice-related processes, is notoriously uncertain due to poor data sampling (Cerovecki et al., 2011). Nevertheless, the general pattern (shown in Fig. 4-1) indicates buoyancy loss in the extreme south polar regions, buoyancy gain on the poleward flank of the ACC, and buoyancy loss in some regions on the equatorward flank associated with mode water formation. Although the current meanders and splits as it makes its way around topographic features, authors such as de Szoeke and Levine (1981) and Ivchenko et al. (1996) have argued that, when the real ACC is described using a "streamwise-average" view, the large-scale dynamics bear a close resemblance to zonally symmetric models.

Indeed, zonal channel models with highly idealized geometry form the foundation of contemporary theories of the Southern Ocean circulation, capturing the essential physics of the system and providing insight into important mechanisms (Munk and Palmén, 1951; McWilliams et al., 1978; Marshall, 1981; Johnson and Bryden, 1989; Marshall, 1997; Olbers et al., 2004; Marshall and Radko, 2006, among many). The Southern Ocean MOC, however, exports and imports water from other ocean basins
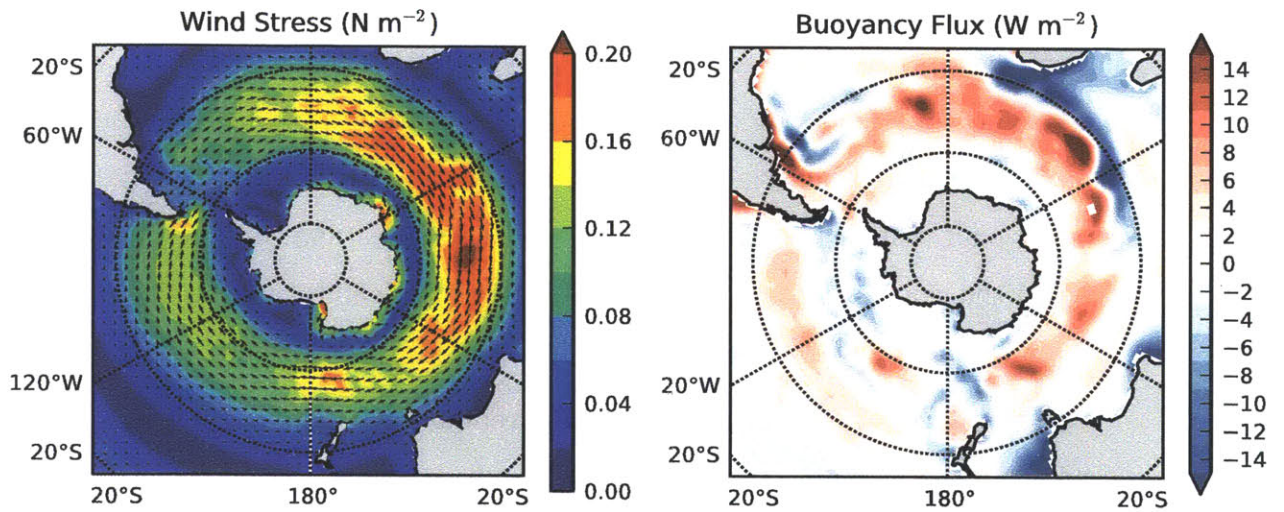
Figure 4-1: Maps of the observed surface forcing in the Southern Ocean, averaged from the CORE2 dataset over the period 1949-2006 (Large and Yeager, 2009). The left panel shows the wind stress in $N\,m^{-2}$, with the magnitude indicated by the colored shading and the direction by the arrows. The right panel shows the buoyancy-equivalent heat flux in $W\,m^{-2}$ equivalent, and includes contributions from longwave and shortwave radiative fluxes, latent and sensible heat fluxes, as well as the buoyancy fluxes due to evaporation, precipitation, and runoff.

(e.g. Ganachaud and Wunsch, 2000; Talley, 2008). Antarctic Bottom Water (AABW) flows out of the Southern Ocean in the deepest layers. North-Atlantic Deep Water (NADW) and Circumpolar Deep Water (CDW) flow in (poleward) at intermediate depths, and Antarctic Intermediate Water (AAIW) and Sub-Antarctic Mode Water (SAMW) flow equatorward in the the upper thermocline. As a result, channel-only models that attempt to investigate the Southern Ocean MOC without representing other basins find vanishingly weak deep residual circulations (Karsten et al., 2002; Kuo et al., 2005; Cessi et al., 2006; Cerovecki et al., 2009). Some authors have tackled this problem by attaching closed basins to their channels. This approach can certainly yield insights, but it also adds to the complexity of the problem by introducing gyre dynamics. When such basins are global scale, as in Wolfe and Cessi (2009), the computational cost of an eddy resolving model becomes immense. When they are small (on the same order of the channel itself), as in Henning and Vallis (2005) and Viebahn and Eden (2010), the link with the real ocean is less clear.

We choose to address this problem in a novel way: by including a narrow "sponge layer" along the channel's northern boundary, in which the temperature is relaxed to a prescribed exponential stratification profile. This diabatic forcing provides a return pathway for deep residual overturning, which otherwise would not be able to cross isopycnals. Physically, the sponge layer encapsulates all the diabatic processes occurring outside of the Southern Ocean, such as deep water formation by air-sea heat fluxes in the North Atlantic or diapycnal mixing in the abyss. The disadvantage of this method is that the stratification at the northern boundary cannot change significantly. The advantage is that it provides a clean, simple framework in which to investigate non-zero residual circulations, focusing on the dynamics of the channel alone rather than the complex teleconnections of the global problem (Wolfe and Cessi, 2011). In combination with appropriate surface wind and buoyancy forcing, we will see that this configuration can produce realistic overturning cells.

Given the many idealizations made in constructing our model, we must interpret our results with care. We emphasize that our goal is not to make quantitative predications for the real global ocean-atmosphere system—rather, we hope to gain insight

124

into the underlying physical mechanisms that govern this system in order to inform the interpretation of more realistic models and observations.

4.2.2 Model Physics and Numerics

The basic physical system simulated by our model is a Boussinesq fluid on a beta-plane with a linear equation of state and no salinity. The model is forced mechanically by a surface stress and thermodynamically by a surface heat flux as well as by the aforementioned sponge-layer restoring. Mechanical damping is provided by linear bottom drag—there is no topography. Key physical and numerical parameters are given in Tab. 4.1.

Table 4.1: Parameters used in the numerical model reference experiment.

Symbol	Value	Description
L_x, L_y	1000 km, 2000 km	Domain size
L_{sponge}	1900 km	Latitude where the sponge layer begins
H	2985 m	Domain depth
ρ_0	999.8 kg m^{-3}	Reference density
α	2×10^{-4} K^{-1}	Linear thermal expansion coefficient
f_0	-1×10^{-4} s^{-1}	Reference Coriolis parameter
β	1×10^{-11} s^{-1} m^{-1}	Meridional gradient of Coriolis parameter
Q_0	10 W m^{-2}	Surface heat flux magnitude
τ_0	0.2 N m^{-2}	Wind stress magnitude
r_b	1.1×10^{-3} m s^{-1}	Linear bottom drag parameter
τ_{sponge}	7 days	Sponge layer relaxation timescale
Δ_x, Δ_y	5 km	Horizontal grid spacing
Δ_z	10 - 280 m	Vertical grid spacing
κ_v	0.5×10^{-5} m s^{-2}	Vertical diffusivity
κ_h	0	Horizontal diffusivity
A_v	3.0×10^{-4} m s^{-2}	Vertical viscosity
A_h	12.0 m s^{-2}	Horizontal viscosity
A_4	9.0×10^8 m^4 s^{-1}	Horizontal hyper-viscosity

The surface thermal forcing in our model is intended to mimic, in a simplified way, the observed buoyancy flux over the Southern Ocean (see Fig. 4-1). In the first set of experiments, a heat flux is simply prescribed to include a region of cooling in the far south of the domain, heating in the middle, and cooling again farther north.

125

These regions are intended to represent, respectively, the buoyancy loss associated with AABW formation, the buoyancy gain over the ACC, and the buoyancy loss associated with AAIW / SAMW formation north of the front. More precisely, the heat flux has the form

$$Q(y) = -Q_0 \cos(3\pi y/L_y) \text{ for } y < 5L_y/6 \qquad (4.1)$$

and $Q = 0$ north of this point, with $Q_0 = 10$ W m^{-2}. L_y is the length of the channel in y. (Q is positive downward, i.e. heat flux into the ocean.) This simple pattern of buoyancy flux is consistent with a recent review of all the available air-sea buoyancy flux data products by Cerovecki et al. (2011).

Inside the sponge layer, the temperature T is relaxed to the prescribed temperature profile

$$T^*(z) = \Delta T(e^{z/h} - e^{-H/h})/(1 - e^{-H/h}) , \qquad (4.2)$$

which describes an exponential decay from ΔT at the surface to 0 at depth $-H$ with a scale height of h. The relaxation coefficient increases from 0 (meaning no relaxation) at the southern edge of the sponge layer ($y = L_{sponge}$) to 7 days^{-1} at the northern boundary ($y = L_y$). The choice of an exponential temperature profile was motivated by observations (Karsten and Marshall, 2002b), laboratory studies (Cenedese et al., 2004) and modeling results (Karsten et al., 2002; Henning and Vallis, 2005; Wolfe and Cessi, 2009). The results described in the rest of the paper all use $h = 1000$ m, a value close to the "natural" stratification that arises when the sponge layer is turned off, and to the observed stratification on the equatorward flank of the real ACC. We experimented with several values of the stratification depth h, and found that the MOC transport was rather insensitive to this choice.

The final key element of the forcing is the wind stress. A zonal stress is applied at the surface of the form

$$\tau_s(y) = \tau_0 \sin(\pi y/L_y) . \qquad (4.3)$$

For the base-case simulation, $\tau_0 = 0.2$ N m^{-2}, but a central point of our study is to

explore the strength of the MOC given different values of τ_0.

Dissipation is mainly accomplished through linear bottom drag. A stress is applied at the bottom of the form

$$\boldsymbol{\tau}_b = \rho_0 r_b \mathbf{u_b} \tag{4.4}$$

where r_b is a bottom drag coefficient and $\mathbf{u_b}$ the horizontal component of the bottom velocity.

The model code is the MITgcm, a general-purpose primitive-equation solver (Marshall et al., 1997a,b). The domain is a Cartesian grid 1000 km long (i.e. zonal direction), 2000 km wide (i.e. meridional direction), and 2985 m deep. Although this domain is relatively narrow, the zonal symmetry means that a larger domain would not alter the results and would only add computational cost. The domain size does not appear to constrain the eddy size, since a typical eddy size is $\sim$ 200 km. We resolve the first baroclinic deformation radius (approx. 15 km in the center of the domain), employing 5-km horizontal resolution and with 30 vertical levels, with spacing increasing from 10 m at the surface to 280 m at the bottom. A realistically effective diapycnal diffusivity ($\kappa_v = 0.5 \times 10^{-5}$ m s^{-2}) is maintained thanks to the second-order-moment advection scheme of Prather (1986) (see also Hill et al., 2011). In order to maintain a surface mixed layer, we employed the KPP mixing scheme (Large et al., 1994). In our case, this scheme simply acts to mix tracers and momentum over a layer of roughly 50 m depth.

The model was spun up from rest for approximately 200 years until it reached a statistically steady state, as indicated by the mean kinetic energy. A typical eddy temperature field from the equilibrated state is shown in Fig. 4-2. Averages were performed over 20-year intervals. In cases where parameters were changed, the model was allowed to reach a new equilibrium before taking an average.

4.2.3 The Zonal Momentum Balance

Since the meridional flux of momentum by Reynolds stresses is relatively small, the depth-integrated zonal-average momentum balance dictates (c.f. Cessi et al., 2006)
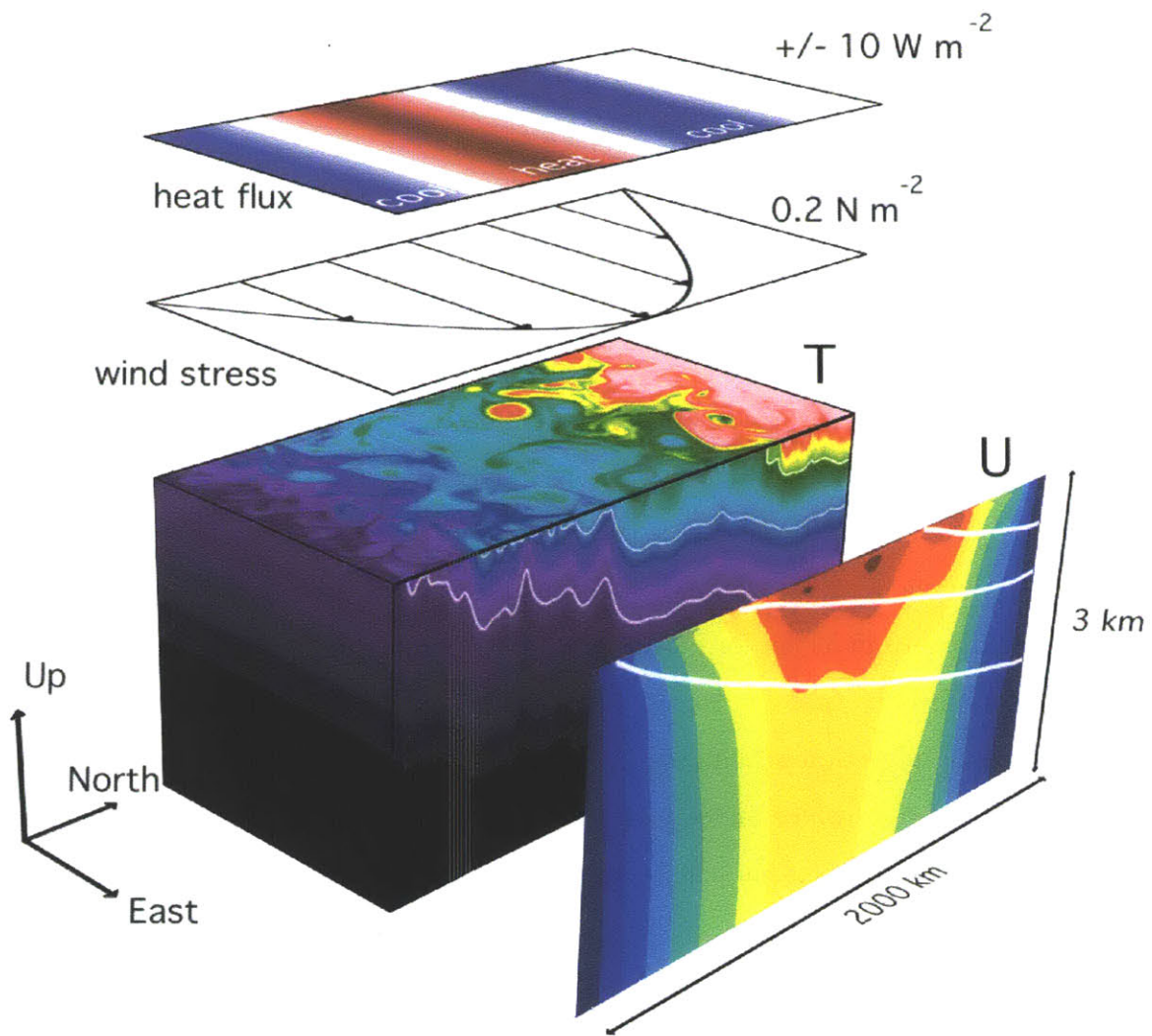
Figure 4-2: A 3D snapshot of the model's temperature field, revealing the mesoscale eddy field. The temperatures range from 0 - 8° C. Overlaid on top are depictions of the wind stress and heat flux surface forcing. To the right is the zonal- and time-mean zonal velocity $\overline{u}$, which ranges from 0 - 25 cm s^{-1}. The contour interval for $\overline{u}$ is 2.5 cm s^{-1}. Overlaid in white are the 1, 3, and 5° C isotherms.

that

$$\tau_s = \hat{\mathbf{x}} \cdot \overline{\boldsymbol{\tau}}_b = \rho_0 r_b \overline{u}_b \tag{4.5}$$

where the overbar indicates a zonal and time average. This balance states that the momentum input by the wind (constant in x and time) is balanced by bottom drag on a mean zonal flow at the bottom. In the real ocean, in contrast, topographic form drag is believed to balance the wind stress (Munk and Palmén, 1951; Johnson and Bryden, 1989; Hughes, 1997; Olbers, 1998; Ferreira et al., 2005). This means that our model requires a significant steady bottom flow (~ 17 cm s^{-1}) and thus has an unrealistically large zonal transport: 788 Sv for the reference case. But most of this transport is barotropic and simply translates the entire system westward without any consequences for the overturning circulation. The zonal transport by the baroclinic flow is only 99 Sv.

A steady meridional circulation exists in Coriolis balance with these steady zonal stresses. Outside of the Ekman layers, this circulation is described by the streamfunction

$$\overline{\Psi} = -\frac{\tau_s}{\rho_0 f} , \tag{4.6}$$

where $\overline{v} = -\partial \overline{\Psi}/\partial z$ and $\overline{w} = \partial \overline{\Psi}/\partial y$. The absence of topography means that the surface Ekman flow is returned in a bottom Ekman layer, rather than by a geostrophic flow below topography. But the strength of $\overline{\Psi}$ is independent of the nature of the bottom drag and is driven solely by the wind.

Likewise, as discussed in detail in Sec. 4, the barotropic component of the flow does not participate in the eddy energy cycle, and thus we expect the eddy-driven circulation to be similar with or without topography. Experiments performed with a topographic ridge (but not described further here) support the conclusion that the presence of topography strongly damps the barotropic zonal flow but does not affect the MOC. We therefore expect that conclusions drawn from our model about the MOC can still apply to the real Southern Ocean, especially to the portion of the flow that occurs above major topographic features.

4.2.4 Residual Overturning Circulation

To diagnose the residual MOC, we computed a streamfunction from the time- and zonal-mean transport in isopycnal layers, defined as

$$\Psi_{iso}(y, b) = \frac{1}{\Delta t} \int_{t_0}^{t_0 + \Delta t} \int \int_0^b (vh) db' dx dt \, , \tag{4.7}$$

where $h = -\partial z / \partial b$ is the layer thickness and b' is a dummy variable of integration. (In practice, the average was performed in 22 discrete, uniformly spaced temperature layers.) This technique has become widely-used for diagnosing transport in the presence of eddies (Döös and Webb, 1994; Henning and Vallis, 2005; Hallberg and Gnanadesikan, 2006; Wolfe and Cessi, 2009, 2010). The transport thus computed includes both the Eulerian-mean (Ekman) transport and the eddy-driven component. We can map this streamfunction into z-coordinates by using the mean depth of buoyancy surfaces, $\Psi_{iso}(y, b) = \Psi_{iso}[y, \bar{b}(y, z)]$. The leading-order equivalence between Ψ_{iso} in z-coordinates and the Transformed-Eulerian-Mean (TEM) residual circulation is well documented (Andrews et al., 1987; McIntosh and McDougall, 1996). (See Sec. 4 for more on TEM theory.) Ψ_{iso} is the most climate-relevant quantity because it describes the circulation that advects tracers such as heat an carbon. Henceforth when we refer to "the MOC," we will generally be talking about Ψ_{iso} as defined in (4.7).

The MOC is characterized by three distinct cells, as shown in Fig. 4-3. In the interior of the domain, away from the surface and the sponge layer, the MOC is directed along mean isopycnals, i.e. $\Psi_{iso} = \Psi_{iso}(\bar{b})$. Although the circulation is highly idealized, it shares several important features with the real Southern Ocean MOC, as described for example, by Rintoul et al. (2001), Lumpkin and Speer (2007), Talley (2008), or Marshall and Speer (2011). The magnitude of Ψ_{iso} (~ 0.5 Sv) is realistic: if our channel were as long as the real Southern Ocean (a factor of about 25), the transport would be roughly 12 Sv. The broad upwelling band at mid depth can be thought of as NADW / CDW. This upwelling water splits into two separate cells. The upper branch travels north, eventually encountering a region
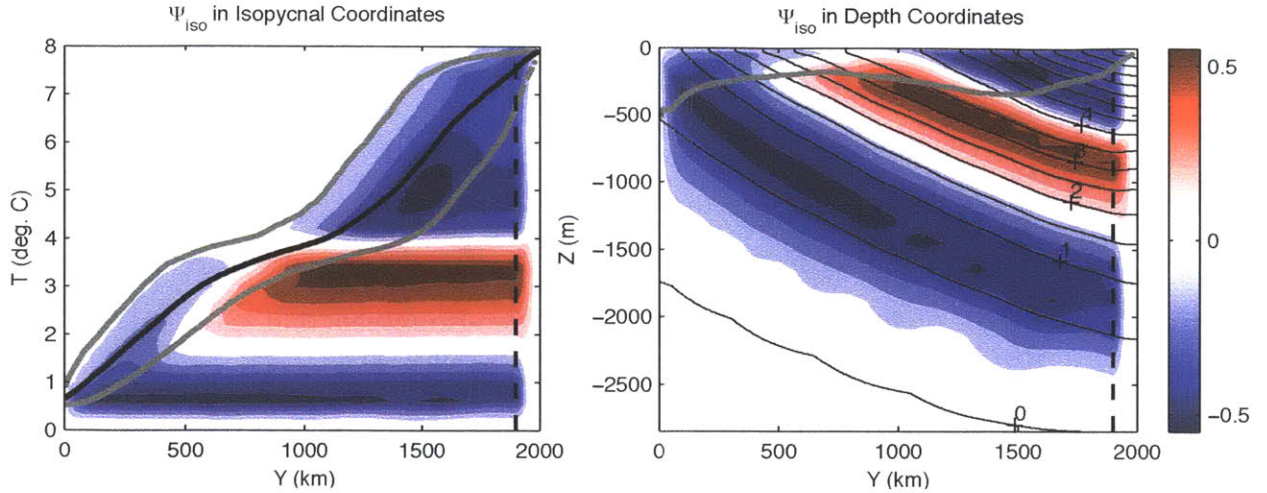
Figure 4-3: The residual MOC streamfunction Ψ_{iso} as originally diagnosed in isopycnal coordinates (left panel), and mapped back to depth coordinates (right panel). The units are Sverdrups (10^6 m^3 s^{-1}), and the contour interval is 0.1 Sv. The solid black line in the left panel indicates the mean SST, and the grey lines are the 5% (left panel only) and 95% levels of the SST CDF. The dotted black is the southern boundary of the sponge layer. The mean T contours are also shown in the right panel in black, contour interval 0.5°C.

of cooling and subduction. The subduction in this northern region along the 4° C isotherm, driven by surface heat loss and accompanied by low values of Ertel potential vorticity, is reminiscent of SAMW / AAIW formation (McCartney, 1977; McCarthy and Talley, 1999). The water associated with downwelling in the far south of the domain resembles AABW in some respects—it is formed by buoyancy loss and is the coldest, densest water in the model. Given the complex physics of AABW formation on the continental shelf, the fact that much of the AABW circulates at depths blocked by topography, and the importance of diapycnal mixing for the lower limb overturning (Ito and Marshall, 2008), this lower cell is not meant to be a truly realistic representation of AABW. All the overturning cells have an adiabatic pathway in the ocean interior and close diabatically in the sponge layer.

The surface heat flux is specified as a fixed function of latitude; consequently, the heat flux is felt by all isopycnals that graze the surface at that particular latitude. The cumulative distribution function (CDF) of surface temperature tells how likely a particular temperature is to be found at the surface and thus be exposed to diabatic

transformation. Superimposed on Fig. 4-3 are the 5% and 95% values of T from the surface temperature CDF. (The mean SST is very close to the median value.) Nearly all of the diabatic MOC transport (i.e. advection across mean isopycnals) takes places in between these values. When plotted in z-coordinates, the 95% CDF value is an effective measurement of the depth of the surface diabatic layer—below it, the contours of Ψ_{iso} and $\bar{b}$ coincide. This view also reveals that the northernmost, shallow, counter-clockwise MOC cell is contained almost entirely by the diabatic layer. We do not focus further on this shallow cell, concentrating from now on only on the two cells (lower and upper) that enter the adiabatic interior.

This definition of the MOC streamfunction (4.7) should be distinguished from the steady, Eulerian-mean overturning streamfunction $\overline{\Psi}$ (4.6). The difference between the two circulations we define as the eddy circulation:

$$\Psi_{eddy} = \Psi_{iso}\left(y, z(\bar{b})\right) - \overline{\Psi}(y, z) \ . \tag{4.8}$$

Both $\overline{\Psi}$ and Ψ_{eddy} are shown in Fig. 4-4. Their magnitudes are large, but they oppose each other, leaving Ψ_{iso} as a small residual. Since the dependence of $\overline{\Psi}$ on the wind is clear from (4.6), the difficulty in understanding the residual MOC sensitivity to the winds lies in Ψ_{eddy}.

4.2.5 Sensitivity to Sponge Layer Restoring Timescale

Here we briefly address the sensitivity of the model to strength of the restoring timescale in the sponge layer, which we will call λ_{sponge}. Our intention was that the sponge layer would respond passively to the surface heat flux, simply returning the heat lost or gained at the surface rather than driving the circulation actively. For this to be the case, the overturning should not be overly sensitive to the value of λ_{sponge}. We experimented with four different values of λ_{sponge}, ranging from 7 days^{-1} up to 120 days^{-1}. The strength of the upper and lower overturning cells for these different values are plotted in Fig. 4-5. For the lower cell, there is no clear dependence on λ_{sponge} at all. For the upper cell, over the first three values of λ_{sponge}, there
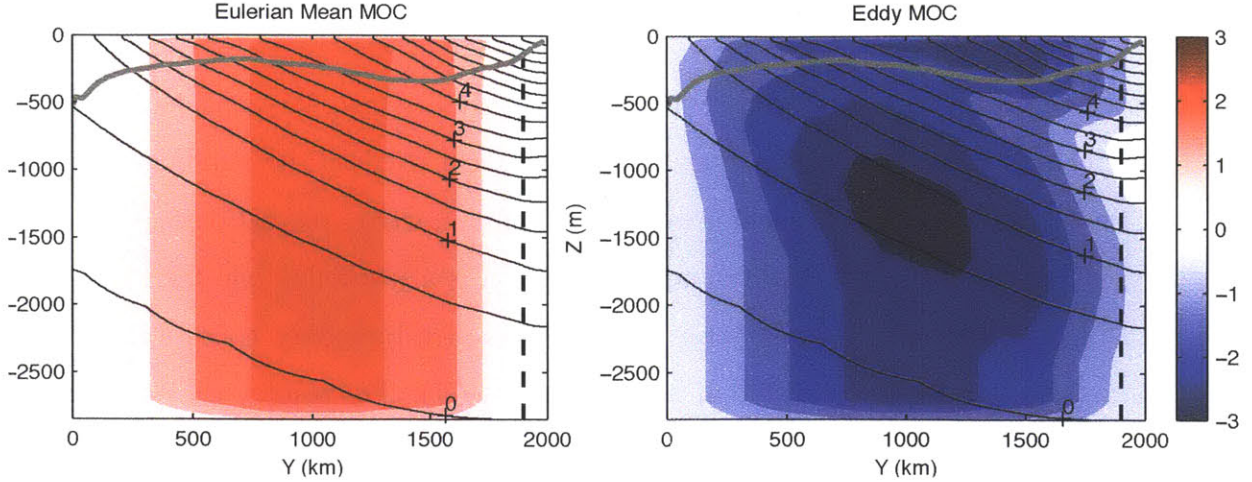
Figure 4-4: The Eulerian-mean streamfunction $\overline{\Psi}$ (left panel) and the eddy stream-function Ψ_{eddy} (left panel), as defined by (4.8). The units are Sverdrups (10^6 m^3 s^{-1}), and the contour interval is 0.5 Sv. Otherwise the same as Fig. 4-3, right panel.

is no significant change. For the weakest relaxation, the upper cell strength actually increases by about 20 %. This is a slightly counterintuitive result, since in the limit of no relaxation, the overturning shuts down completely. The qualitative structure of the overturning, with three distinct cells, does not change at all. In general, the weak dependence on λ_{sponge} indicates that the surface forcing, rather than the sponge layer, governs the overturning.
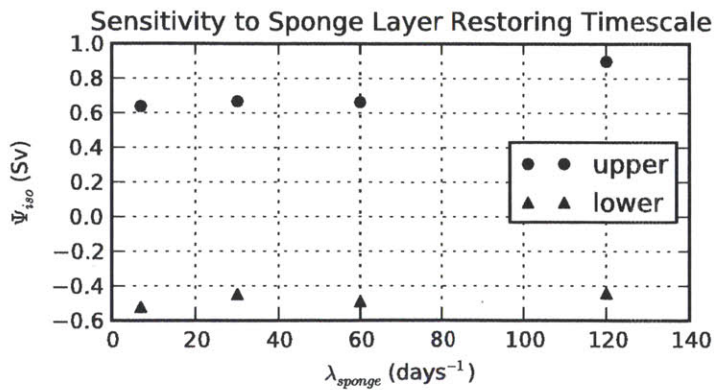
Figure 4-5: Sensitivity of overturning strength to λ_{sponge} the sponge layer restoring timescale.

133

4.2.6 Model Response to Wind Changes

We now examine the MOC sensitivity to altered wind stress. We consider two principal cases. First, the surface buoyancy flux is held fixed as the winds are varied. In the second set of experiments, we employ an interactive, relaxation-type boundary condition. The fixed-flux boundary condition is a justifiable one for freshwater and incoming shortwave radiation, but an interactive boundary condition is more appropriate for sensible and latent heat (Haney, 1971). The results are summarized in Fig. 4-6, where the strengths of the upper and lower cells in each experiment are plotted on a single graph. Since Ψ_{iso} is roughly constant along isopycnals below the diabatic layer, we diagnosed the transports by simply finding the maximum and minimum values of Ψ_{iso} below 500 m at $y = 1800$ km, 100 km south of the edge of the sponge layer. We will henceforth refer to these maximum and minimum values of Ψ_{iso} as MOC_{upper} and MOC_{lower}. Besides the individual upper and lower cells, there is a third relevant quantity: the total volume flux of upwelled deep water: $MOC_{upwell} = MOC_{upper} - MOC_{lower}$. This value is also shown in Fig. 4-6, along with the strength of $\overline{\Psi}$, the Ekman circulation. MOC_{upper}, MOC_{lower}, MOC_{upwell} are weaker than $\overline{\Psi}$ in almost all cases.

In general, the various MOC values appear to have linear dependence on the wind. This is not a universal rule for all possible models and ranges of parameters (e.g. Viebahn and Eden, 2010), but it is an accurate and useful approximation for our particular experiments. This simplification allows us to characterize the MOC sensitivities in a single number by a simple least-squares linear fit applied to Fig. 4-6. The slope $\partial MOC / \partial \tau_0$ gives a sense of how strongly each cell depends on the wind. These values are given in the first column of Tab. 4.2, along with the value of R^2 for the regression. The R^2 values reveal that the linear fit is very good in most cases.

Fixed Flux Boundary Condition

The MOC transports are rather insensitive to the wind in the fixed flux experiments. MOC_{lower} shows no correlation with τ_0, varying in a narrow range about 0.4 Sv.
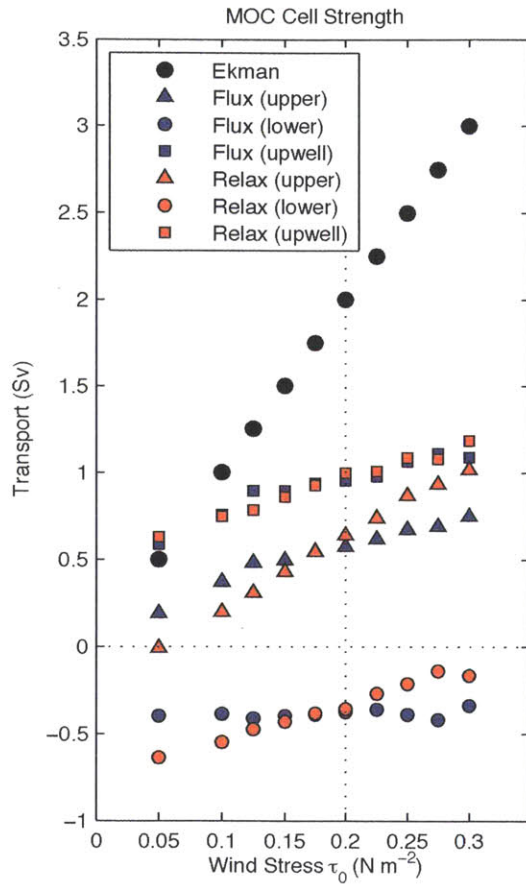
Figure 4-6: A summary of the MOC cell strength in all of the different experiments. The Ekman circulation $\overline{\Psi}$ is shown in black, and the residual circulations of the various MOC cells (upper, lower, and net upwelling) are plotted in color. Fixed-surface-flux experiments are represented in blue; surface-relaxation experiments in orange. The shapes correspond to the values of MOC_{lower}, MOC_{upper}, and MOC_{upwell}. The reference case, $\tau_0 = 0.2$ N m^{-2} is indicated by the dotted line.

MOC_{upper} is quite weak for the weakest winds ($\tau_0 = 0.05$ and 0.1 N m^{-2}), but for the rest of the experiments (0.125 N m$^{-2} \geq \tau_0 \geq 0.3$ N m^{-2}), the changes in MOC_{upper} are slight: it increases only from 0.5 Sv to 0.6 Sv over this range. The linear fit for $\partial MOC_{upper}/\partial \tau_0$ (Tab. 4.2) shows a sensitivity $1/4$ that of the Ekman circulation. Examination of the structure of Ψ_{iso} show that, for weak winds, the upper cell becomes confined more and more to the surface diabatic layer and does not reach the interior. Since MOC_{lower} doesn't change, MOC_{upwell} follows the changes in MOC_{upper}. The small changes in residual MOC reflect the fact that, as the magnitude of $\overline{\Psi}$ increases with the wind, Ψ_{eddy} also strengthens (becoming increasingly negative), leading to a high degree of compensation between mean and eddy circulations.

Relaxation Boundary Condition

We implement the interactive boundary condition in the MITgcm by relaxing the temperature in the top model level, referred to as T_s, to a prescribed function of latitude $T^*(y)$. For the base-case winds ($\tau_0 = 0.2$ N m^{-2}), we wish to have the same effective heat flux as the fixed-flux reference case described above. For a layer of depth Δz subject to relaxation at a rate λ, the effective heat flux is

$$Q_{eff} = -\Delta z \rho_0 c_p \lambda (T_s - T^*) . \tag{4.9}$$

We chose a relaxation timescale of $\lambda = 30$ days^{-1}.[1] Given T_s from the base-case fixed-flux experiment, the desired heat flux Q (4.1), and $\Delta z = 10$ m, this expression can be rearranged to find T^*. As expected, when the $\tau_0 = 0.2$ N m^{-2} simulation is run with this forcing, it reaches the same equilibrium as the base-case fixed-flux state described in the previous section, with the same MOC transport, since the heat flux felt by the ocean is nearly unchanged. However, when τ_0 is changed, T_s can and does change, resulting in an altered air-sea heat flux and, evidently, greater sensitivity of Ψ_{iso} to the winds.

The results of these experiments are also shown in Fig. 4-6. The changes are

---

[1]This choice of parameters corresponds to a sensitivity of $\partial Q_{eff}/\partial T_s \sim 15$ W m^{-2} K^{-1}.

significantly larger than the fixed-flux case. Both MOC_{upper} and MOC_{lower} increase with stronger winds; this means a *strengthening* of the upper cell (since it is positive, i.e. clockwise) and a *weakening* of the lower (negative, counterclockwise) cell. The linear fit (Tab. 4.2) shows that MOC_{upper} is nearly twice as sensitive as the fixed-flux case. Since the changes in $\overline{\Psi}$ are the same under both boundary conditions, the higher sensitivity implies that the magnitude Ψ_{eddy} is not as sensitive to τ_0, leading to less compensation.

Viebahn and Eden (2010) performed a very similar experiment, simulating only an upper cell and using a relaxation boundary condition for buoyancy. Their results are broadly consistent with ours: a sensitivity of the residual circulation much weaker than the sensitivity of the Ekman circulation. However, they observed decreasing sensitivity with increasing winds, while the trend in our MOC_{upper} appears quite linear. This qualitative difference is most likely attributable to the different northern boundary—they had a small, unforced basin attached to the northern edge of their channel, rather than a sponge layer.

4.3   The Surface Buoyancy Boundary Condition

Our experiments make it clear that a residual overturning driven by a fixed buoyancy flux is less sensitive to the winds than one with an interactive buoyancy flux. In this section we seek to understand this behavior diagnostically through the residual buoyancy budget, using the framework of MR.

4.3.1   Transformed-Eulerian-Mean Buoyancy Budget

We begin by reviewing some essential elements of TEM theory (Andrews and McIntyre, 1976; Andrews et al., 1987; Treguier et al., 1997; Plumb and Ferrari, 2005). The reader is referred to MR for a complete discussion of the theory in the context of ACC dynamics.

The time and zonally-averaged buoyancy equation for our domain (outside of the

sponge layer) is

$$\bar{v}\frac{\partial \bar{b}}{\partial y} + \bar{w}\frac{\partial \bar{b}}{\partial z} + \frac{\partial (\overline{v'b'})}{\partial y} + \frac{\partial (\overline{w'b'})}{\partial z} = \frac{\partial B}{\partial z} \qquad (4.10)$$

where $B = (g\alpha/\rho_0 c_p)Q$ is the downward buoyancy flux from the surface forcing. (We have neglected the relatively small fluxes due to diffusion.) The goal of TEM theory is to simplify the eddy-flux terms by separating them into advective and diabatic components. The eddy advection can then be combined with the mean advection in a residual streamfunction Ψ_{res}:

$$\Psi_{res} = \overline{\Psi} + \Psi^* . \qquad (4.11)$$

MR choose to define the TEM eddy streamfunction as

$$\Psi^* = -\frac{\overline{w'b'}}{\bar{b}_y} . \qquad (4.12)$$

The TEM residual streamfunction Ψ_{res}, defined using (4.11) and (4.12), is nearly identical to Ψ_{iso}. Now (4.10) can be manipulated into the form

$$J(\Psi_{res}, \bar{b}) = \frac{\partial B}{\partial z} - \frac{\partial}{\partial y}[(1-\mu)\overline{v'b'}] , \qquad (4.13)$$

where the Jacobian term J represents advection by the residual circulation and the factor μ measures the diabatic eddy flux contribution:

$$\mu = -\frac{\overline{w'b'}}{\overline{v'b'}} \left(\frac{\bar{b}_z}{\bar{b}_y}\right) . \qquad (4.14)$$

When the eddy flux is directed along mean isopycnals, $\mu = 1$ and the second term on the RHS of (4.13) vanishes. If both terms on the RHS are zero, as expected in the ocean interior, then $J(\Psi_{res}, \bar{b}) = 0$ means that Ψ_{res} is constant along isopycnals.

At this point, MR make several assumptions to arrive at an analytic solution. First, they assume the existence of a mixed layer of fixed depth h_m in which $\bar{b}_z = 0$. Following Treguier et al. (1997), they assume that $\mu = 1$ in the ocean interior and varies from 1 at the base of the mixed layer to 0 at the surface. The buoyancy flux B

138

is also assumed to reach zero by the base of the mixed layer. Integrating (4.13) over this mixed layer, one obtains

$$\Psi_{res}(y, z = -h_m)\frac{\partial \bar{b}_s}{\partial y} = B + D \ . \tag{4.15}$$

where $\bar{b}_s(y)$ is the surface mixed-layer buoyancy. We have also defined

$$D = -\int_{-h_m}^{0} (1 - \mu)\frac{\partial}{\partial y}\overline{v'b'} \ dz \tag{4.16}$$

as the mixed-layer-integrated diabatic eddy flux divergence. Equation (4.15) states that advection by the residual flow across the mixed-layer buoyancy gradient is balanced by diabatic forcing and diabatic eddy fluxes.
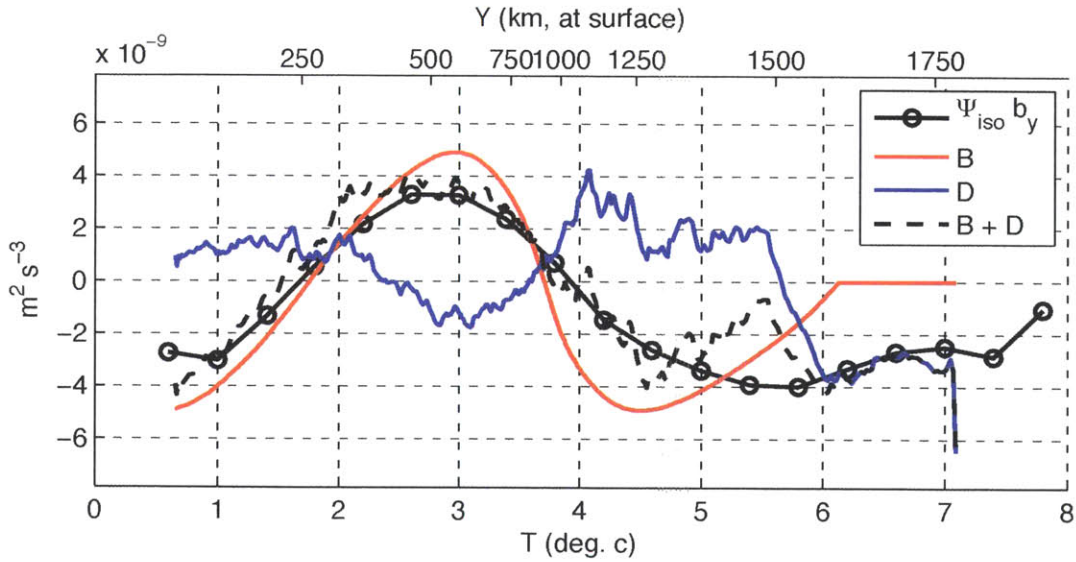
Figure 4-7: The terms in the approximate form of the Marshall-Radko balance (4.17). The plot is shown as a function of T on the bottom of the x-axis, but can also be considered a function of y, whose corresponding values are shown at the top of the x-axis.

In the MR model (of which (4.15) is a central component), Ψ_{res} reaches its full value at the base of the mixed layer. However, in our model, the surface diabatic layer (200 - 300 m) extends much deeper than the shallow mixed layer ($\sim$ 50 m). Fig. 4-3 makes it clear that Ψ_{iso} (approximately equivalent to Ψ_{res}) does not reach

its full interior value until below the diabatic layer. To overcome this complication, we express B, D, and $\partial \overline{b}/\partial y$ as functions of the vertically-averaged buoyancy within the diabatic layer (b_{dl}). We can then write (4.15) approximately as

$$\Psi_{iso}(\overline{b})\frac{\partial \overline{b}}{\partial y}(b_{dl}) \simeq B(b_{dl}) + D(b_{dl}) \ . \tag{4.17}$$

We can see by plotting the three terms of this equation (Fig. 4-7) that the agreement is good throughout most of the domain. This diagnosis shows that the diabatic forcing B determines the strength and sense of the interior MOC. The diabatic-eddy-flux term D is small but not negligible; it generally opposes B, resulting in a weaker Ψ_{iso}. The largest imbalance in this approximate form arises in the region associated with uppermost counter-clockwise cell (between $T = 5°C$ and $T = 6°C$), which contains a recirculation cell entirely within the diabatic layer, a complication not considered in the MR theory. This surface cell is not the focus of our analysis.

4.3.2 Buoyancy Flux Sensitivity to Winds

The residual buoyancy budget as expressed by (4.15) or (4.17) already reveals the strong constraint imposed on the MOC by a fixed surface buoyancy flux: since the term B cannot change, changes in the MOC must be accompanied by changes in $\partial b_s/\partial y$ or D. In the relaxation case, in contrast, B can also change, implying a higher degree of freedom for the MOC. This freedom is reflected in the higher MOC sensitivity in the relaxation experiments.

As described above for the reference case, we can diagnose the forcing terms B and D from each of our experiments to understand how these terms change with the wind—this is shown in Fig. 4-8, which contains contour plots of B and D as functions of y and τ_0. Also plotted are contours of the zonal-mean SST, from which it is easy to see the changes in $\partial b_s/\partial y$. From this figure, we can see that two factors contribute to the strengthening of the upper cell in the fixed-flux case. First, the diabatic eddy flux D (Fig. 4-8c), which generally opposes the heating from B centered on $y = 666$ km, decreases with increasing winds, leading to greater total buoyancy gain in this

region. Second, the SST contours in this region spread apart as the winds increase, decreasing $\partial b_s / \partial y$, which further contributes in the increase in Ψ_{res}. On the other hand, in the lower cell formation region (the most southern part of the domain), trends in D and $\partial b_s / \partial y$ evidently cancel, leading to no trend in the Ψ_{res} associated with the lower cell.

The changing air-sea buoyancy flux B in the relaxation case is evident in Fig. 4-8b. The flux is everywhere increasing as the winds increase, in accord with the fact that SSTs are decreasing (see (4.9)). (SSTs also change in the fixed-flux case, but since the flux is not interactive, this has no effect on B.) This is completely consistent with the increased upper cell transport and decreased lower cell transport. In comparison with the fixed-flux case, the changes in $\partial b_s / \partial y$ are less significant, resulting from the fact that SST is being relaxed to the same function of y in all experiments. Changes in D seem insignificant for the upper cell region but still potentially important for the lower cell.

Dependence of the air-sea buoyancy flux B on wind stress was observed by Badin and Williams (2010) in a similar yet coarse-resolution model. Their study also noted the sensitivity of B to the choice of Gent-McWilliams eddy-transfer coefficient. In our interactive-buoyancy-flux experiments, both the eddy transfer and the buoyancy flux are free to respond to changing winds, resulting in a tangled equilibration problem. The diagnostics presented in this section merely show how the buoyancy budget is consistent with the residual circulation—they do not explain the magnitude of the sensitivity. For that, we need to look closer at the eddy circulation itself.

4.4 Constraints on the Eddy Circulation

In this section we seek to understand what sets the strength of the eddy circulation. This discussion is most relevant to the interactive-buoyancy-flux experiments, whose residual circulation cannot be assumed *a priori* based on knowledge of the buoyancy flux. The essential question is: how well can we estimate the sensitivities of Ψ_{iso} reported in Tab. 4.2 based on first principles?
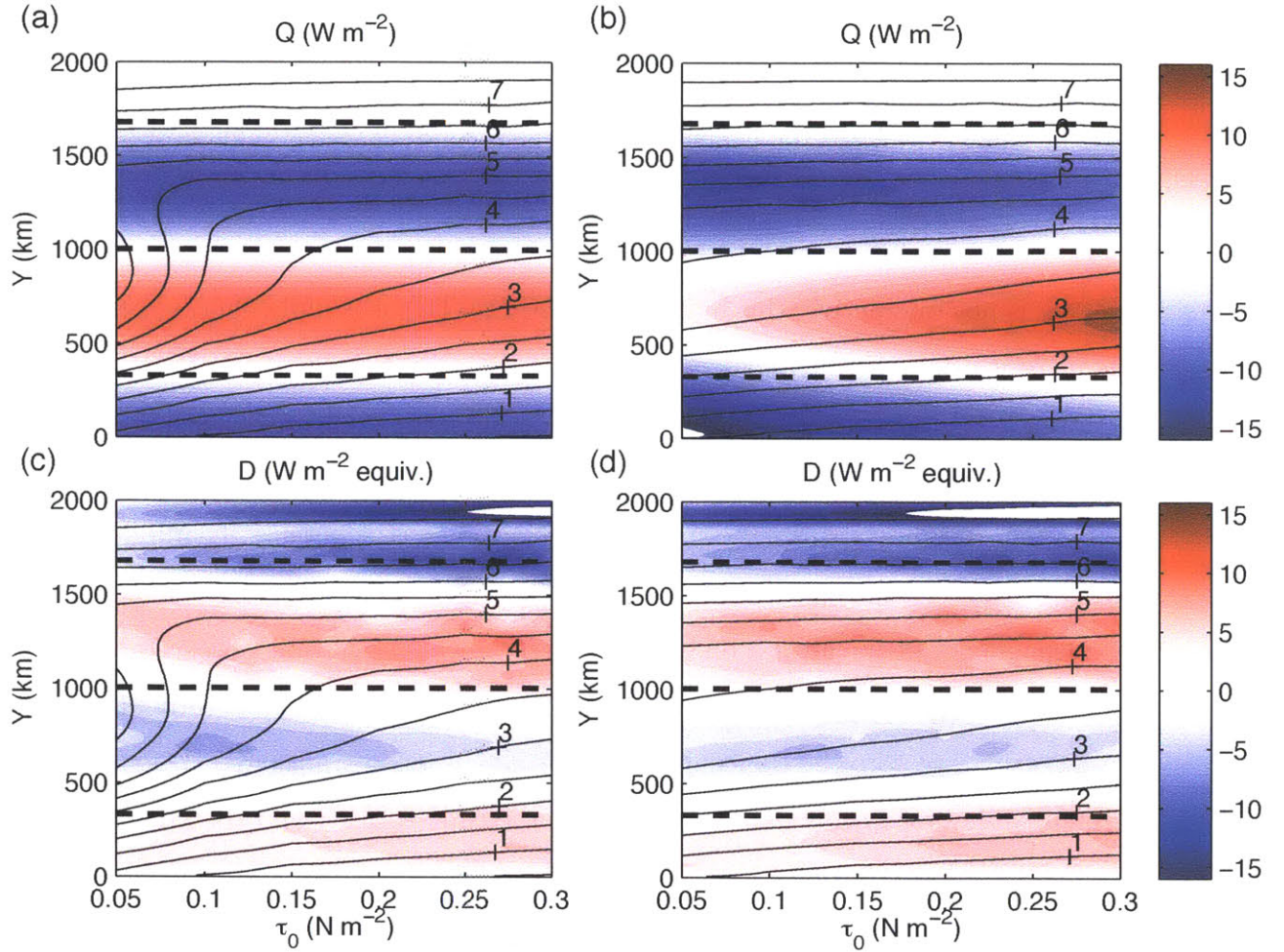
Figure 4-8: The forcing terms of the surface residual buoyancy budget (4.22) for changing values of wind τ_0, expressed in units of W m^{-2} equivalent by multiplying by $\rho_0 c_p (g\alpha)^{-1}$. The air-sea buoyancy flux B for the fixed-flux case is shown in (a), and the diabatic eddy flux D is shown in (c). (b) and (d) are the same terms, but for the relaxation surface boundary condition. The thin black lines are contours of the zonal-average SST, contour interval $0.5°$ C, from which changes in the surface buoyancy gradient $\partial b_s / \partial y$ can be inferred. The thick dashed black lines indicate the boundaries of the regions of applied surface heating and cooling from the reference experiment $\tau_0 = 0.2$ N m^{-2}.

4.4.1 Decomposing the Eddy Circulation: Slope and Diffusivity

In the adiabatic interior, the TEM eddy circulation can be written as

$$\Psi^* = \frac{\overline{v'b'}}{\overline{b}_z} . \tag{4.18}$$

This form is identical to the earlier definition (4.12) when $\mu = 1$, which is a good approximation away from the surface diabatic layer and sponge layer and very close to Ψ_{eddy} as defined in (4.8).

Assuming a flux gradient relationship $\overline{v'b'} = -K(y,z)\overline{b}_y$, where K is the eddy diffusivity, we can write (4.18) as

$$\Psi^* = Ks \tag{4.19}$$

where $s = -\overline{b}_y/\overline{b}_z$ is the mean isopycnal slope. (4.19) is the basis of the famous Gent-McWilliams parameterization for mesoscale eddies (Gent and McWilliams, 1990; Gent et al., 1995). Here it is simply a rearrangement of the definition of Ψ^* given the definition of K. Using the definition of $\overline{\Psi}$ (4.6), the residual circulation then becomes

$$\Psi_{res} = -\frac{\tau_s}{\rho_0 f} + Ks . \tag{4.20}$$

This expression is a centerpiece of the MR model.

Viebahn and Eden (2010) applied (4.20) to their eddy-resolving model in order to ascertain the relative importance of changes in K and s. We follow a very similar path. Consider a reference state in which $\tau_0 = \tau_{0\_ref} = 0.2$ N m^{-2}: the variables for this state will be denoted K_{ref}, s_{ref}, etc. For different values of τ_0, the departures of these variables from the reference state will be expressed as ΔK, where $\Delta K = K - K_{ref}$, and similarly for the other variables. Using this notation, we can express Ψ_{res} for any

143

τ_0 state as

$$\Psi_{res} = \overline{\Psi}_{ref}\left(1 + \frac{\Delta\overline{\Psi}}{\overline{\Psi}_{ref}}\right) + \Psi^*_{ref}\left(1 + \frac{\Delta\Psi^*}{\Psi^*_{ref}}\right) \tag{4.21}$$

$$\simeq \overline{\Psi}_{ref}\left(1 + \frac{\Delta\tau_0}{\tau_{0\_ref}}\right) + \Psi^*_{ref}\left(1 + \frac{\Delta K}{K_{ref}} + \frac{\Delta s}{s_{ref}}\right) , \tag{4.22}$$

where a quadratic Δ-term has been dropped. (Note that $\overline{\Psi}_{ref} = \tau_{s\_ref}/\rho_0 f$ and $\Psi^*_{ref} = K_{ref}s_{ref}$.) The first term in (4.22) expresses the linear scaling of the Ekman-driven circulation with the wind. The second term expresses the eddy response. If we can develop a theory for the fractional changes in K and s with changing τ_0, we can effectively predict the MOC departure from a reference state for a change in winds.

Viebahn and Eden (2010) found that changes in s were very small compared to changes in K, and that the changes in Ψ^* could therefore be attributed primarily to changes in K. To test this idea in our model, we calculate $\Delta\Psi^*/\Psi^*_{ref}$, $\Delta K/K_{ref}$, and $\Delta s/s_{ref}$ from the model output. The calculation is performed at a depth of 477 m, below the surface diabatic layer, but shallow enough to see all the MOC cells. (Above this depth, we find that (4.18) is not a very good approximation of Ψ_{iso}.) The terms are plotted in Fig. 4-9 as a function of y and τ_0. We see that Ψ^* changes by about 50% from the reference case in either direction (weaker or stronger winds). K undergoes changes in magnitude almost as large. However, s is notably less sensitive, weakening by 20% for weak winds and barely changing at all for stronger winds. Changes in s are most significant in the southernmost part of the domain, where new isopycnals outcrop with increasing winds. For the fixed-flux experiments, in contrast, s undergoes large changes in a wider part of the domain (not shown).

The relative insensitivity of s seems somewhat inevitable given the boundary conditions. Since the buoyancy is relaxed to prescribed values at both the surface and the northern boundary, the large-scale isopycnal slope is effectively prescribed as well. (Of course, small changes in surface buoyancy are necessary to bring about changes in heat flux, as seen in Fig. 4-8.) Only isopycnals that don't outcrop are unconstrained on the southern edge, resulting in higher values of $\Delta s/s_{ref}$ in the far

144
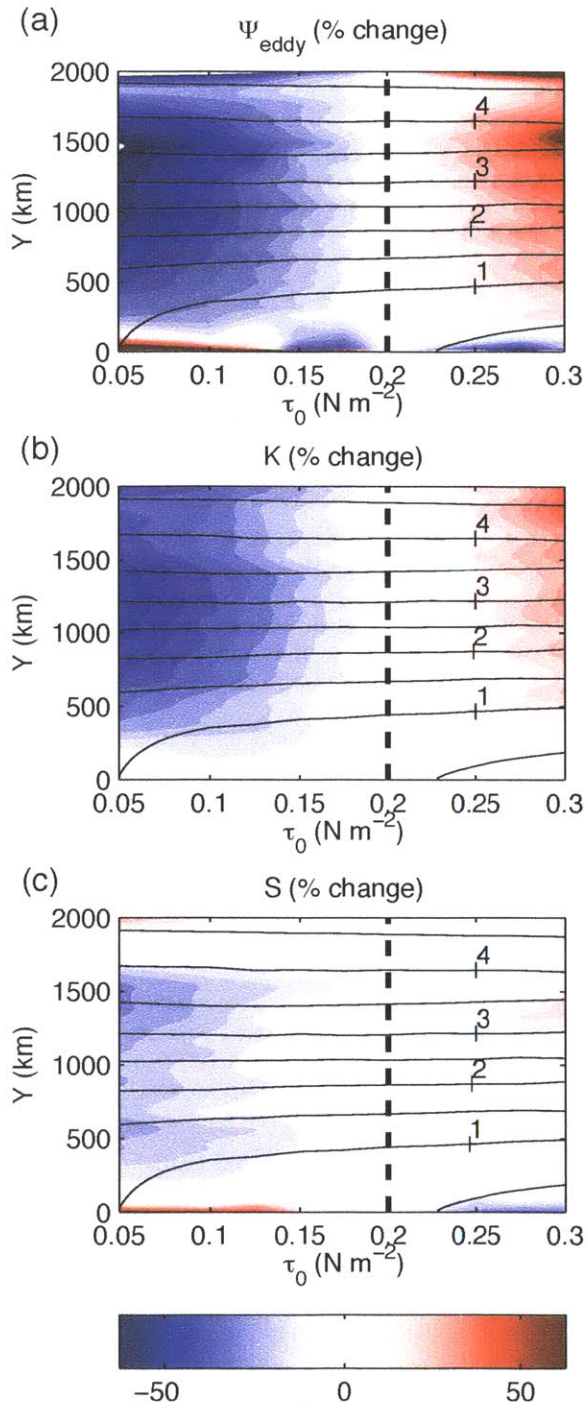
Figure 4-9: Fractional changes in (a) eddy circulation $\Delta\Psi^*/\Psi^*_{ref}$, (b) eddy diffusivity , $\Delta K/K_{ref}$, and (c) isopycnal slope $\Delta s/s_{ref}$ from the reference case (indicated by the dashed black line), computed at 477 m depth. The black contours are the mean isotherms at this depth, contour interval 0.5° C.

southern part of the domain. Viebahn and Eden (2010) found Δs to be small in an experiment with no sponge layer.

Focusing on the same surface ($z = -477$ m), we can use (4.22) to directly estimate MOC_{upper} and MOC_{lower} by picking points in y that correspond with the maximum and minimum values of Ψ_{iso}. (These points do not move significantly in space with changes in τ_0.) By calculating Δs and ΔK at these points, we can evaluate (4.22). The linear MOC sensitivities produced in this way are given in the third column of Tab. 4.2. These sensitivities agree very well with the values given by Ψ_{iso}, indicating that (4.22) is a good approximation.

Given the observed smallness of Δs, we can ask, to what extent is the sensitivity of the MOC due to ΔK? To answer this question, we evaluate (4.22) with $\Delta s = 0$, and compute the linear sensitivity. For comparison, we also do the opposite, setting $\Delta K = 0$ and using only Δs. The results, given in the fourth column of Tab. 4.2, indicate that ΔK is the dominant factor in the upper cell sensitivity in both the fixed-flux and relaxation experiments. Especially in the relaxation experiment, the sensitivity due to Δs alone is close to the $\overline{\Psi}$ sensitivity, suggesting a negligible role for Δs. In contrast, ΔK and Δs seem to play equal roles in the lower cell sensitivity.

4.4.2 Eddy Diffusivity Dependence on Wind Stress

Given the prominent role of ΔK in determining the MOC sensitivity, we focus now on understanding its scaling behavior with the winds. As a starting point, we plot the full $K(y, z)$ for three different values of τ_0 in Fig. 4-10. In general, K is positive nearly everywhere and appears intensified very near the surface and towards the bottom, with a minimum at mid depth. The details of the vertical structure of K are interesting, but are not our focus here. (A paper on this topic is in preparation.) For now, we simply note that the spatial structure does not change qualitatively with τ_0, allowing us to imagine a fixed spatial structure that simply scales with τ_0. (Viebahn and Eden (2010) found a strikingly similar spatial pattern.) Many studies, including MR and Visbeck et al. (1997), have assumed that K itself is proportional to s. Instead, we employ a mixing length theory, which relates K to the eddy kinetic

146

energy, and thus to the mechanical energy balance.
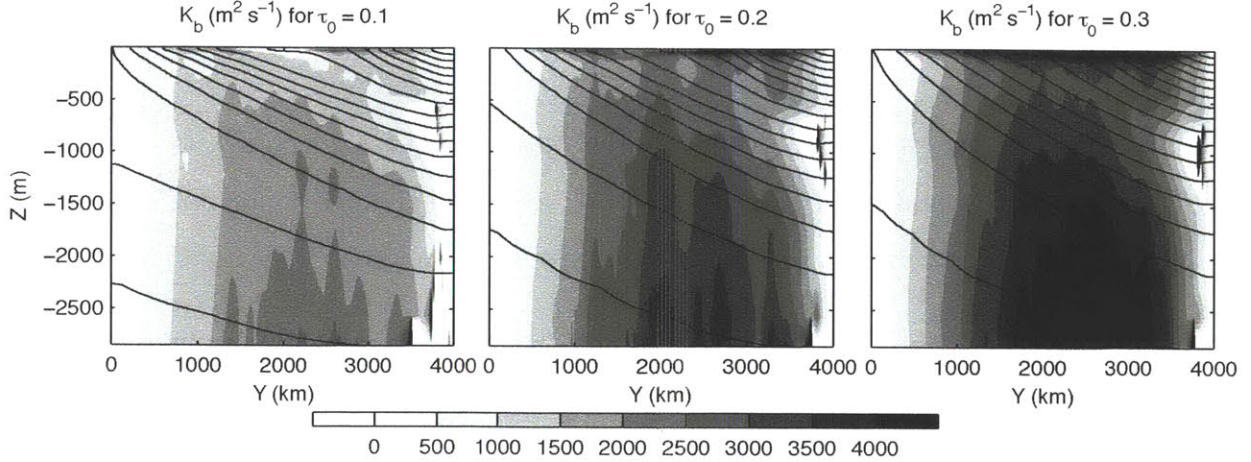
Figure 4-10: Flux-gradient buoyancy diffusivity $K(y,z)$ for three different wind strengths and fixed-flux boundary condition, shown with contour interval 500 m^2 s^{-1}. The black contours are the mean isotherms, contour interval 0.5° C.

Mixing-length theory (Taylor, 1921; Prandtl, 1925) claims that the eddy diffusivity can be expressed as a characteristic eddy velocity V_e times an eddy length scale L_e, such that $K \simeq V_e L_e$. Many authors have applied this idea to estimate eddy diffusivities in the ocean (Holloway, 1986; Keffer and Holloway, 1988; Davis, 1991; Stammer, 1998; Eden and Greatbatch, 2008; Ferrari and Nikurashin, 2010).[2] A general theory predicting V_e and L_e for geostrophic turbulence does not yet exist, but the topic is a very active area of research (Held and Larichev, 1996; Lapeyre and Held, 2003; Thompson and Young, 2007).

Cessi (2008) suggested that the appropriate V_e to use for the buoyancy diffusivity is the *barotropic* eddy velocity, i.e. the RMS anomaly of the vertically-averaged velocity, because barotropic stirring can most efficiently mix buoyancy across sloping isopycnals. We make the key assumption that this value, and thus K itself, is proportional (but not necessarily equal) to the *bottom* eddy velocity. In terms of eddy

---

[2]Ferrari and Nikurashin (2010) recently refined the idea to include the modulation of L_e by the presence of mean flows, and there is indeed mounting evidence that the spatial variations in K in the Southern Ocean are modulated by the strong jets found there (Marshall et al., 2006; Smith and Marshall, 2009; Abernathey et al., 2010; Naveira Garabato et al., 2010).

kinetic energy (the square of V_e), this statement becomes

$$EKE_{bt} \propto EKE_b = \langle \tfrac{1}{2}|\mathbf{u}_b'|^2 \rangle \qquad (4.23)$$

where $\mathbf{u}_b'$ is the velocity anomaly at the bottom. The angle brackets indicate an average in x, y and time. (The ideas could be easily extended to include dependence on y, but here we find it simpler to concentrate on the domain average.)

Following Cessi et al. (2006) and Cessi (2008), we consider the mechanical energy budget. Since our model employs linear bottom drag, the leading-order balance of the system is

$$\langle \tau_s \overline{u}_s \rangle \simeq \rho_0 r_b \langle |\mathbf{u}_b|^2 \rangle \;, \qquad (4.24)$$

with additional small contributions from viscous dissipation, side drag, and conversion to potential energy. (The zonal-mean surface velocity $\overline{u}_s$ has been used because τ_s is constant in x and time.) Physically, (4.24) expresses the fact that the wind power input to the system is dissipated by bottom drag. Cessi et al. (2006) found this balance to hold well in a similar numerical model. We checked (4.24) in our model and found it to hold not only globally but also in a zonal-average budget to within 10% error (not shown).

The bottom velocity $\mathbf{u}_b$ includes both the mean and eddy velocity: $\langle |\mathbf{u}_b|^2 \rangle = \langle \overline{u}_b^2 \rangle + \langle \overline{v}_b^2 \rangle + \langle |\mathbf{u}_b'|^2 \rangle$. The $\overline{v}_b$ term is negligible in comparison to $\overline{u}_b$. Furthemore, we already know from (4.5) that $\overline{u}_b \simeq \tau_s / (\rho_0 r_b)$. This allows (4.24) to be rearranged to the form

$$\rho_0 r_b \langle |\mathbf{u}_b'|^2 \rangle = \langle \tau_s (\overline{u}_s - \overline{u}_b) \rangle \;. \qquad (4.25)$$

It is important to note that the eddy energy in this expression depends only on the *baroclinic* shear $\overline{u}_s - \overline{u}_b$. The large *barotropic* velocity due to the absence of topography doesn't affect the eddy energy balance. Furthermore, since topographic form drag does not participate in the energy cycle (Ferrari and Wunsch, 2009), we can expect (4.25) to hold in more realistic models with topography. (Note that in the presence of topopgraphy, $\overline{u}_b \simeq 0$.) The baroclinic shear can be obtained from the

148

thermal wind equation:

$$\overline{u}_s - \overline{u}_b = -\frac{1}{f} \int_{-H}^{0} \overline{b}_y(y, z)dz \ . \tag{4.26}$$

Since the large-scale meridional buoyancy gradient $\overline{b}_y$ is determined by the large scale forcing, we can expect this thermal-wind contribution to remain approximately constant[3]. This suggests the scaling relationship

$$EKE_b = \tfrac{1}{2}\langle|\mathbf{u}'_b|^2\rangle \simeq \frac{g\alpha\Delta T H}{\pi f_0 \rho_0 r_b L_y}\tau_0 \tag{4.27}$$

where ΔT is the large-scale temperature difference across the channel, set by the relaxation SST. We have also used the fact that $\langle\tau_s\rangle = 2\tau_0/\pi$. Our mixing length hypothesis claims that K is related to this quantity as $EKE_b = \tfrac{1}{2}(\langle K\rangle/L_e)^2$, where the mixing length constant L_e has absorbed the unknown constant of proportionality between EKE_{bt} and EKE_b.

We can diagnose all these quantities from the model to test our ideas. We assume that the $L_e = $ constant $ = 30$ km. In reality, the mixing length also varies by $\sim 10\%$ (as diagnosed from the simulations), but we can achieve decent agreement without considering these effects, and a theory for L_e is beyond the scope of this paper. EKE_b, EKE_{bt}, $(\langle K\rangle/L_e)^2$, and the scaling prediction from (4.27) are all plotted in Fig. 4-11 on a logarithmic scale as a function of τ_0. Both the fixed-flux and relaxation cases are plotted. The three diagnosed quantities, and the theoretical prediction, show similar slopes, especially for high value of τ_0. The small departures of $\langle K\rangle$ from the EKE values can be explained by our neglect of changes in L_e. The small departures of EKE_b from the scaling theory likewise can be explained by our neglect of second-order energy sources and sinks in (4.24). But based on the general agreement, we conclude that a useful approximation for the eddy buoyancy diffusivity in our model is

$$K \simeq K_{ref} \left(\frac{\tau_0}{\tau_{0\_ref}}\right)^{1/2} \ . \tag{4.28}$$

---

[3]This is equivalent to assuming that the baroclinic transport in the model is "saturated" (Straub, 1993), which is indeed the case for our experiments.
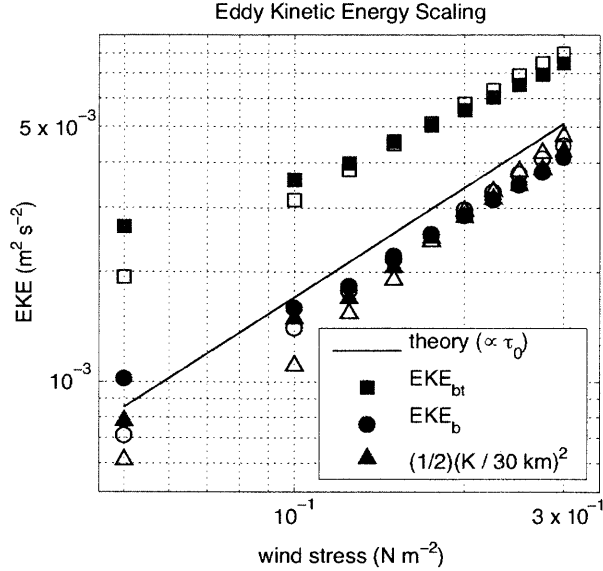
Figure 4-11: Globally-averaged eddy kinetic energies diagnosed from the model. The quantities plotted are the barotropic EKE (square), the bottom EKE (circle), and the EKE implied by the diffusivity K (triangle), assuming a constant mixing length of 30 km. The black line is the EKE predicted by the scaling relation (4.27). The fixed-heat-flux experiments are white, while the relaxation experiments are gray.

When applying this formula locally in space, we must, however, expect errors due to the changing spatial structure of K shown in Fig. 4-10.

4.4.3 Predicting the MOC Sensitivity

Using the scaling from (4.28) in (4.22), along with the assumption that changes in s can be neglected to first order, we arrive at

$$\Psi_{res} \simeq \overline{\Psi}_{ref}\left(1 + \frac{\Delta\tau_0}{\tau_{0\_ref}}\right) + \Psi^*_{ref}\left[1 + \left(\frac{\Delta\tau_0}{\tau_{0\_ref}}\right)^{1/2}\right] . \qquad (4.29)$$

From this equation, the linear sensitivities of MOC_{upper} and MOC_{lower} can be calculated analytically given $\overline{\Psi}_{ref}$ and Ψ^*_{ref}; they are given in the final column of Tab. 4.2. Two important points must be kept in mind in interpreting these values. First, such estimates can only be as good as the ΔK-only sensitivity already presented, which we noted was most accurate for the relaxation-case upper cell. Second, since

150

$\overline{\Psi}_{ref}$ and Ψ^*_{ref} are nearly the same for both fixed-flux and relaxation experiments, the scaling for ΔK produces nearly identical predictions for the different cases. The final prediction from the scaling theory of the sensitivity of the upper cell in the relaxation case, 6.9 Sv (N m^{-2})$^{-1}$, is higher than the ΔK-only sensitivity, 5.9 Sv (N m^{-2})$^{-1}$, which itself is higher than the true sensitivity, 4.5 Sv (N m^{-2})$^{-1}$. Yet all these values are significantly weaker than the sensitivity of $\overline{\Psi}$, 11.1 Sv (N m^{-2})$^{-1}$. The agreement between the relaxation-case lower-cell sensitivity from the scaling and the true sensitivity is spurious, a case of two wrongs (the neglect of Δs and the failure of (4.28) locally for the lower cell region) making a right. Although our scaling theory is far from comprehensive, we are encouraged by the agreement for the upper-cell relaxation case and consider it a useful stepping stone in a difficult problem.

Table 4.2: Linear MOC dependence on wind, i.e. $\partial MOC/\partial \tau_0$, as determined by least-squares fit. The value of R^2 for the linear regression is given in parenthesis, a measure of the goodness of fit. The values are computed at fixed points in space near where maxima and minima of Ψ_{iso} occur: $z = -477$ m, $y = 1150$ km (upper cell) and $y = 300$ km (lower cell). The first column shows Ψ_{iso}, and the second column $\overline{\Psi}$. The rightmost four columns represent the approximations produced by (4.22), (4.22) with Δs set to zero, (4.22), (4.22) with ΔK set to zero, and finally (4.29), the prediction for the MOC sensitivity given by neglecting Δs and and assuming that K scales locally with (4.28). All units are Sv / (N m^{-2}).

	Ψ_{iso}	$\overline{\Psi}$	ΔK and ΔS	ΔK only	ΔS only	ΔK (scali
fixed-flux, upper cell	2.6 (0.98)	11.2 (1.00)	2.2 (0.96)	5.2 (0.99)	8.1 (1.00)	6.8
fixed-flux, lower cell	-0.1 (0.01)	4.5 (1.00)	0.2 (0.16)	2.1 (0.96)	2.6 (0.97)	1.4
relax, upper cell	4.5 (1.00)	11.1 (1.00)	4.2 (0.99)	5.9 (1.00)	9.3 (1.00)	6.9
relax, lower cell	1.9 (0.99)	4.6 (1.00)	1.9 (0.98)	3.1 (1.00)	3.3 (0.99)	1.6

4.4.4 Quadratic Bottom Drag

Many models choose to represent bottom drag with a quadratic term, proportional to the *square* of the bottom flow, rather than with the linear form we have used. Geostrophic turbulence in the presence of quadratic bottom drag is less sensitive to the value of the bottom-drag coefficient, although both types of drag can pro-

duce eddy behavior consistent with ocean observations (Arbic and Scott, 2008). The scaling theory for EKE described above relies on a balance between surface winds and bottom drag, and although we only performed experiments with linear drag, it is worth considering how this theory would be altered if quadratic drag were used instead.

A quadratic drag parameterization leads to a bottom stress of the form

$$\boldsymbol{\tau}_b = \rho_0 c_d |\boldsymbol{u}_b| \boldsymbol{u}_b \tag{4.30}$$

where c_d is a non-dimensional parameter for the bottom drag strength, with a typical value of 0.0025 (Armi, 1978). The mechanical energy balance becomes, instead of (4.24)

$$\langle \tau_s \bar{u}_s \rangle \simeq \rho_0 c_d \langle |\mathbf{u}_b|^3 \rangle \,, \tag{4.31}$$

Two main issues arise that cause the quadratic-drag case to differ from the linear case. The first is the coupling of the mean and eddy flow at the bottom. Due to the nonlinearity, it is impossible to split the bottom drag into a contribution exclusively from the eddies. In the presence of a strong bottom flow, this would seriously undermine a scaling theory for the eddy energy like the one described above. We consider this issue to be of minor importance, however, because the mean bottom flow in the Southern Ocean is very weak due to the presence of topography. If *both* topography and quadratic drag were present (arguably the most realistic possible configuration), there would be no contribution to (4.31) from the mean flow, and the energy balance would again be between wind work on the baroclinic flow and bottom dissipation by the eddies. The only difference would be the power-law dependence. Instead of $EKE \propto \tau_s$, as we found with linear bottom drag, we would obtain $EKE \propto \tau_s^{2/3}$. This indicates that K would still depend on the winds, but with a weaker sensitivity. Ultimately we speculate that this would lead to *stronger* dependence of the MOC on the winds, but without a qualitative change in the picture we obtained with linear drag.

4.5   Discussion and Conclusion

One important conclusion of this study is that the sensitivity of the Southern Ocean MOC to the winds depends on the surface boundary condition for buoyancy. This is not an immediately intuitive result, since the winds are a purely mechanical forcing. However, it becomes clear once one considers the TEM (or equivalently, isopycnal-average) point of view expressed by (4.15): in a quasi-adiabatic ocean interior, the residual MOC is primarily set by diabatic water-mass transformation at the surface, and if the winds are unable to alter the transformation rates (as in the fixed-buoyancy-flux case), the sensitivity of the MOC is weak. In fact, evidence of this point emerges from the existing literature when comparing different models. For instance, Hallberg and Gnanadesikan (2006) used a predominantly fixed-flux surface boundary condition and found a relatively weak sensitivity of the residual MOC to increased winds. In contrast, Wolfe and Cessi (2010) used a relaxation boundary condition and found much greater sensitivity; in certain locations, they found an increase in residual MOC transport almost equal to the increase in Ekman transport, the upper limit of the sensitivity. The increased transport was accompanied by increased transformation in both southern and northern high latitudes. Although our model contains only an ACC channel, it manages to qualitatively reproduce the behavior of both these two different models just by changing the surface boundary condition. Similar conclusions were reached by Bugnion et al. (2006), using an adjoint method in a coarse-resolution model, and by Badin and Williams (2010).

The surface boundary condition of the real ocean is mixed. Certain contributions to the air-sea buoyancy flux, such as net shortwave radiation and precipitation, are largely independent of the SST and surface winds. Latent and sensible heat fluxes, on the other hand, are interactive (Haney, 1971). For the winds to play a strong role in modulating the residual MOC, as envisioned by Toggweiler and Russell (2008), our study suggests that the interactive fluxes must dominate. It should therefore be a top priority to continue to improve our understanding of the processes that determine the air-sea buoyancy flux in the Southern ocean—including sea-ice processes, which we

have completely neglected—and whether these components are sensitive to changes in wind or other climate changes.

Of the various simplifications we have made, perhaps the most restrictive and unrealistic is the fixed stratification imposed by the northern boundary sponge layer. In fact, many of the related studies we have cited have focused explicitly on the question of what sets the stratification (Marshall and Radko, 2003; Henning and Vallis, 2005; Wolfe and Cessi, 2010). In the analytical model of MR, the thermocline depth was found to be proportional to $\tau_0^{1/2}$, but their eddy closure ($K \propto |s|$) does not hold in our eddy resolving model. Henning and Vallis (2005) found a weaker scaling of the stratification with the wind ($\sim \tau_0^{1/4}$) in an eddy-resolving model of a channel coupled to a basin. Such results are encouraging because, if the stratification dependence on τ_0 is weak, it is more reasonable to approximate it as fixed, as we have done. Nevertheless, tests of our results in more realistic, global, eddy-resolving models are required.

Finally, we developed a scaling theory for the eddy-diffusivity and used it estimate the MOC sensitivity. Traditionally, scaling theories for eddies have been based on ideas from linear baroclinic instability, and the eddy diffusivity is assumed to be somehow proportional to the isopycnal slope (Green, 1970; Stone, 1972; Killworth, 1997; Visbeck et al., 1997). Although baroclinic instability plays a crucial role in the energy cycle of our model, linear theory cannot predict the fully equilibrated eddy energy. Instead we have followed some of the ideas developed by Cessi (2008), invoking the mechanical energy balance to gain insight into the eddy energy and diffusivity. Consequently our scaling theory for the eddy diffusivity (4.27) includes a dependence on both the wind stress parameter τ_0 and the bottom drag r_b, but not the isopycnal slope s. The scaling shows good agreement with the GCM results. Furthermore, we think it represents a promising way forward in understanding the role of eddies in the equilibration of the Southern Ocean.

We have examined only steady states, but the time-dependent response to wind changes is important and interesting. Meredith and Hogg (2006) have suggested Southern Ocean eddies can respond very fast ($\sim$ 1 year) to changes in wind, while

154

Treguier et al. (2010) found that the interannual MOC variability in a realistic model was dominated by Ekman transport, with little eddy compensation. This issue deserves further study as well.

Chapter 5

Conclusion

5.1 Summary

This thesis has presented three studies aimed at deepening our understanding of mesoscale ocean eddies and their role in the climate system. The first two chapters were primarily diagnostic, concerned with the spatial geography of eddy mixing rates and the implications of this geography. Chapter 2 explored the depth-latitude structure of mixing in the Southern Ocean, while Chapter 3 used satellite data to examine the global patterns of mixing at the surface. The final chapter presented an idealized, eddy resolving model of the Southern Ocean and analyzed its response to changes in wind stress. Although on the surface the final chapter sounds unconnected to the first two, eddy mixing rates were revealed to be the crucial quantity determining the the sensitivity of the overturning circulation to the wind changes. A common thread to all of these studies is that the behavior of mesoscale eddies is significantly more varied and complex than assumed by climate models, and that this complexity can potentially have significant consequences for large-scale climate.

In Chapter 2, we saw how mixing rates vary with depth and latitude across the ACC. At the surface in the core of the ACC, mixing is suppressed by the strong mean flow, while on the flanks of the jet (especially northward), mixing rates are higher. However, a subsurface maximum arises below the jet where EKE is still strong but the mean flow is weaker. The band of strong mixing shoals to the north

and connects smoothly with the surface maximum. We diagnosed horizontal mixing rates at the surface, which presumably apply to the mixing of buoyancy and other tracers at the surface, and isopycnal mixing rates in the interior, which we interpreted as diffusivities for potential vorticity. We used the interior diffusivities to estimate the eddy flux of potential vorticity and thus infer the residual overturning circulation. We did not take the step of attempting to compare this estimate with the "true" residual circulation; the complexity of the SOSE model made the task of actually calculating the residual circulation daunting. In fact, the desire for a simpler model inspired the development of the idealized channel model used in Chapter 4.

The goals of chapter 2 were twofold: I wanted to expand the view of mixing beyond just the Southern Ocean, and I wanted to incorporate real data into my thesis. The use of satellite data limited the analysis to the surface flow, but at the same time brings a degree of credibility to the results that is not possible with models alone. The first step was to perform effective diffusivity calculations in a "zonalized" East Pacific domain. This simplified flow facilitated the computation and comparison of different diagnostics. One particularly encouraging result was the close equivalence between Nakamura effective diffusivity and traditional zonally-averaged flux-gradient diffusivity; despite the widespread recent use of the Nakamura diagnostic, this equivalence has, to our knowledge, not yet been demonstrated in a real flow. We introduced the Osborn-Cox diffusivity and showed that it is a reliable diagnostic of local mixing associated with divergent eddy fluxes. We then calculated the Osborn-Cox diffusivity worldwide, producing a global map of eddy mixing, the first such global estimate using tracer-based methods. The mean flow was found to have a strong effect on mixing, leading to both suppression and enhancement depending of the region in question. As a final step, we used the map of mixing to estimate eddy flux of quasi-geostophic potential vorticity near the surface. We related this quantity to an eddy stress, which we found had a spatial pattern similar to the wind stress. The magnitude of the eddy stress was generally weaker than the wind stress, but far from negligible. On the other hand, the magnitude was much greater than the eddy stress that would be produced by the Gent and McWilliams (1990)

parameterization using common mixing coefficients. This suggests a significant role for eddies in the surface ocean circulation that is not adequately captured by climate models.

The idealized channel model of Chapter 4 presented a more self-contained setting to study eddies and their role in ocean circulation, with closed budgets of heat, momentum, and energy and a residual overturning circulation that could be calculated directly, rather than inferred. We focused on a concrete question: what is the residual overturning response to changes in winds? The sensitivity to the winds, it turned out, was largely determined by the changes in eddy mixing rates. Therefore this seemingly simple question forced us to grapple with the difficult and long-standing problem of baroclinic equilibration. We made progress by analyzing the eddy energy budget, and drew a link from the wind power input to the eddy dissipation at the bottom and finally to eddy mixing rates. By examining, from first principles, *why* eddy mixing rates have their observed magnitudes, the final chapter is truly more ambitious the the first two and, despite being only a single chapter, represents the greatest amount of my time and effort.

5.2   Future Directions

This research provokes many new questions. Many of these question lie at the intersections between the three chapters. First and foremost is to reconcile the mixing diagnostics in SOSE with those from the channel model. The channel model of chapter 3 focused primarily on the horizontal mixing of buoyancy, while the SOSE analysis calculated isopycnal tracer diffusivities, which we associate with potential vorticity mixing. Horizontal buoyancy diffusivity is a very convenient quantity when dealing with eddy-induced streamfunctions and is easily related to climate models through the Gent-McWilliams parameterization. It is also a very stable quantity to diagnose, since the lateral buoyancy gradient never changes sign in the Southern Ocean. However, potential vorticity is in some sense more fundamental, since the enstrophy budget requires it to be down-gradient on average. The vertical structure of buoyancy

159

diffusivity can be very different from the PV diffusivity (Smith and Marshall, 2009), and the relationship between the two is related to the baroclinic criticality of the flow (Held and Larichev, 1996; Thompson and Young, 2007; Jansen and Ferrari, 2012). Both diffusivities are presumably related to the full diffusivity tensor **K** of Plumb and Mahlman (1987). A straightforward comparison of all these quantities in the channel model would help clarify this somewhat foggy landscape of different diffusivities.

A related question is how to best make use of observational mixing data to infer eddy-induced circulations. The Diapycnal and Isopycnal Mixing Experiment in the Southern Ocean (DIMES, Gille et al., 2007) aims to directly measure mixing rates using floats and tracers. Klocker et al. (2011b) made an important contribution to the eventual interpretation of the DIMES results by showing that, under ideal circumstances, the tracer- and float-based isopycnal diffusivities should agree. But a further step is required. The original DIMES announcement claims that "[u]ltimately, results from the experiment should facilitate improvements in the representation of mixing in numerical models of the ocean and climate." In order to reach this point, we must know how to translate the tracer- and float-based data into diffusivities of potential vorticity and / or buoyancy, in a form that models can use. Our idealized channel model could be an ideal test-bed for making this link, allowing us to simulate DIMES-style experiments and test methodologies for inferring / parameterizing the eddy transport in terms of the simulated experimental results. Some first steps towards this goal are contained in Hill et al. (2011), who focus mainly on diapycnal mixing rather than mesoscale eddy mixing.

One unfortunate conclusion of Klocker et al. (2011b) is that the number of floats used in the DIMES experiment may not be enough to constrain even the *sign* of the Lagrangian isopycnal diffusivity. In other words, the magnitude of the error will likely exceed the mean, rendering the results effectively meaningless. If this is the case, the best means for measuring eddy mixing rates will continue to be satellite altimetric data. Chapter 3 presented a comprehensive global view of mixing rates derived from altimetric data, but this view is only *at the surface*. Therefore new theories and methods must be developed to extrapolate the surface results to the interior. Killworth

160

and Hughes (2002) concluded that in the ACC the flow can be accurately described in with an equivalent barotropic framework, wherein the horizontal geostrophic velocities decay exponentially with depth from their surface values. Klocker et al. (2011b) made use of this idea to rescale the satellite-derived surface velocities in the ACC and derive diffusivities at every depth, with results consistent with Abernathey et al. (2010) from the SOSE model. Unfortunately, the prospect of applying such a procedure globally is doubtful, since the equivalent barotropic structure does not apply outside of the ACC. Scott and Furnival (2011) recently assessed different strategies for extrapolating surface geostrophic velocities to the interior using basis functions (e.g. baroclinic modes) and introduced a new set of functions with relatively good predictive skill at 400m depth; this could be a way forward for assessing subsurface mixing rates globally. Alternatively, statistical / stochastic methods may be able to estimate the eddy fluxes directly without explicitly resolving the sub-surface flow, but such techniques are still in their infancy in oceanic applications (Keating et al., 2012). A final possibility would be to apply the formula of Ferrari and Nikurashin (2010) globally in conjunction with accurate estimates of the eddy phase speed, comparing with results from eddy-resolving models.

Another potential direction for the ideas explored in this thesis, Chapter 4 in particular, is in the area of eddy parameterization. A common refinement to the Gent and McWilliams (1990) parameterization is to make the eddy diffusivity proportional to the local Eady growth rate, related to the isopycnal slopes (e.g. Visbeck et al., 1997). This approach is grounded fundamentally in linear theory. In Chapter 4 we pursued a slightly different path; following Cessi (2008), we tried to relate the eddy mixing rate to the energy dissipation rate, a perspective consistent with theories of fully-developed, forced-dissipative baroclinic turbulence. Since the rate of energy input to the system was largely controlled by the wind, this pathway proved to be sufficient for understand the scaling of the mixing rates with the wind. It would be interesting to explore this idea in more generality and to ask to what extent wind-power input, dissipation, and eddy mixing are correlated globally. Along these lines, a framework for an energetically-motivated parameterizations of the eddy flux of

potential vorticity was recently developed by (Marshall et al., 2012). This area seems ripe for progress.

A final issue left relatively unexplored by this work is the issue of topography and its influence on mixing. It is well known that the presence of bottom topography can strongly affect eddy fluxes by altering potential vorticity gradients (Holloway, 1997). A recent study by Thompson (2010) showed that the presence of rough topography leads to intermittent and mixing and variability in zonal jets. A futher study (Thompson and Sallée, 2011) suggested that mixing in the Southern Ocean is concentrated in "hotspots" near topographic features. It would be very interesting to explore how the mixing patterns found in Chapters 2 and 3 correlate with topographic features. Futhermore, the model of Chapter 4 could be easily modified to create a mixing hotspot, allowing us to explore the role of topographically-induced mixing in the the meridional overturning circulation.

Bibliography

Abernathey, R., J. Marshall, and D. Ferreira, 2011: The dependence of southern ocean meridional overturning on wind stress. *J. Phys. Oceanogr.*, **41 (12)**, 2261–2278.

Abernathey, R., J. Marshall, E. Shuckburgh, and M. Mazloff, 2010: Enhancement of mesoscale eddy stirring at steering levels in the southern ocean. *J. Phys. Oceanogr.*, 170–185.

an D. Qin, S. S., M. Manning, Z. Chen, M. Marquis, K. Averyt, M. Tignor, and H. Miller, (Eds.) , 2007: *Contribution of Working Group I to the Fourth Assessment Report of the Intergovernmental Panel on Climate Change.* Cambridge University Press.

Anderson, R. F., S. Ali, L. I. Bradtmiller, S. H. H. Nielsen, M. Q. Fleisher, B. E. Anderson, and L. H. Burckle, 2009: Wind-driven upwelling in the southern ocean and the deglacial rise in atmospheric co2. *Science*, **323**, 1143–1150.

Andrews, D., J. Holton, and C. Leovy, 1987: *Middle Atmosphere Dynamics.* Academic Press.

Andrews, D. and M. McIntyre, 1976: Planetary waves in horizontal and vertical shear: The generalized elliasen-palm relation and the mean zonal acceleration. *J. Atmos. Sci.*, **33**, 2031–2058.

Arbic, B. K. and R. B. Scott, 2008: On quadratic bottom drag, geostrophic turbulence, and oceanic mesoscale eddies. *J. Phys. Oceanogr.*, **38**, 84–104.

Archer, D., H. Kheshgi, and E. Maier-Reimer, 1997: Multiple timescales for neutralization of fossil fuel co2. *Geophys. Res. Lett.*, **24**, 405–408.

Armi, L., 1978: Some evidence for boundary mixing in the deep ocean. *J. Geophys. Res.*, **81 (1971-1979)**.

Badin, G. and R. G. Williams, 2010: On the buoyancy forcing and residual circulation in the southern ocean: The feedback from ekman and eddy transfer. *J. Phys. Oceanogr.*, **40**, 295–311.

Boss, E. and L. Thompson, 1999: Lagrangian and tracer evolution in the vicinity of an unstable jet. *J. Phys. Oceanogr.*, **29**, 288–304.

Bower, A. S., 1991: A simple kinematic mechanism for mixing fluid parcels across a meandering jet. *J. Phys. Oceanogr.*, **21**, 173–182.

Bower, A. S., H. T. Rossby, and J. L. Lillibridge, 1985: The gulf stream–barrier or blender. *J. Phys. Oceanogr.*, **15**, 24–33.

Bower, A. S. and T. Rossby, 1989: Evience of cross-frontal exchange processes in the gulf stream based on isopycnal rafos float data. *J. Phys. Oceanogr.*, **19**, 1177–1191.

Bretherton, F. P., 1966: Critical layer instability in baroclinic flows. *Quart. J. Roy. Meteor. Soc.*, **92**, 325–334.

Bugnion, V., C. Hill, and P. H. Stone, 2006: An adjoint analysis of the meridional overturning circulation in an ocean model. *J. Climate*, **19**, 3732–3751.

Cenedese, C., J. Marshall, and J. A. Whitehead, 2004: A laboratory model of thermocline depth and exchange fluxes across circumpolar fronts. *J. Phys. Oceanogr.*, **34**, 656–668.

Cerovecki, I., R. A. Plumb, and W. Heres, 2009: Eddy transport and mixing in a wind and buoyancy driven jet on the sphere. *J. Phys. Oceanogr.*

Cerovecki, I., L. D. Talley, and M. R. Mazloff, 2011: Southern ocean air-sea buoyancy flux estimates, manuscript in preparation.

Cessi, P., 2008: An energy-constrained parameterization of eddy buoyancy flux. *J. Phys. Oceanogr.*, **38**, 1807–1820.

Cessi, P., W. R. Young, and J. A. Polton, 2006: Control of large-scale heat transport by small-scale mixing. *J. Phys. Oceanogr.*, **36**, 1877–1895.

Charney, J. G., 1947: 1947. *J. Meteor.*, **4**, 135–162.

Charney, J. G. and M. E. Stern, 1962: On the stability of internal baroclinic jets in a rotating atmosphere. *J. Atmos. Sci.*, **19**, 159–173.

Chelton, D. B. and M. G. Schlax, 1996: Global observations of oceanic rossby waves. *Sceince*, **272 (5259)**, 234–238.

Danabasoglu, G. and J. C. McWilliams, 1995: Sensitivity of the global ocean circulation to parameterizations of mesoscale tracer transports. *J. Climate*, **8**, 2967–2987.

Davis, R., 1991: Observing the general circulation with floats. *Deep Sea Res.*, **38A**, S531–S571.

de Szoeke, R. A. and M. D. Levine, 1981: The advective flux of heat by mean geostrophic motions in the southern ocean. *Deep Sea Res.*, **28A (10)**, 1057–1085.

Dong, S., J. Sprintall, S. Gille, and L. Talley, 2008: Southern ocean mixed-layer depth from argo float profiles. *J. Geophys. Res*, **113**, C06013.

Döös, K. and D. Webb, 1994: The deacon cell and other meridional cells of the southern ocean. *J. Phys. Oceanogr.*, **24**, 429–442.

d'Ovidio, F., E. Shuckburgh, and B. Legras, 2009: Local mixing events in the upper-troposphere and lower-stratosphere: Part 1, detection with the lyapunov diffusivity. *J. Atmos. Sci.*, in Press.

Dritschel, D. G. and M. McIntyre, 2008: Multiple jets as pv staircases: The phillips effect and the resilience of eddy-transport barriers. *J. Atmos. Sci.*, **65**, 855–875.

Eady, E., 1949: Long waves and cyclone waves. *Tellus*, **1**, 33–52.

Eden, C. and R. Greatbatch, 2008: Diapycnal mixing by meso-scale eddies. *Ocean Modeling*, **23**, 113–120.

Eden, C., R. Greatbatch, and D. Olbers, 2007: Interpreting eddy fluxes. *J. Phys. Oceanogr.*, **37**, 1282–1296.

Esler, J. G., 2008a: Robust and leaky transport barriers in unstable baroclinic flows. *Physics of Fluids*, **20**, 116 602.

Esler, J. G., 2008b: The turbulent equilibration of an unstable baroclinic jet. *J. Fluid Mech.*, **599**, 241–268.

Farneti, R., T. L. Delworth, A. J. Rosati, S. M. Griffies, and F. Zeng, 2011: The role of mesoscale eddies in the rectification of the southern ocean response to climate change, accepted to JPO.

Ferrari, R. and M. Nikurashin, 2010: Suppression of eddy diffusivity across jets in the southern ocean. *J. Phys. Oceanogr.*

Ferrari, R. and C. Wunsch, 2009: Ocean circulation kinetic energy: Reservoirs, sources, and sinks. *Annu. Rev. Fluid Mech.*, **41**, 253–282.

Ferreira, D., J. Marshall, and P. Heimbach, 2005: Estimating eddy stresses by fitting dynamics to observations using a residual-mean ocean circulation model and its adjoint. *J. Phys. Oceanogr.*, **35**, 1891–1910.

Forest, C. E., P. H. Stone, A. P. Sokolov, M. R. Allen, and M. D. Webster, 2002: of recent climate observations quantifying uncertainties in climate system properties with the use. *Science*, **295**, 113–117.

Ganachaud, A. and C. Wunsch, 2000: Improved estimates of global ocean circulation, heat transport and mixing from hydrographic data. *Nature*, **408**, 453–459.

Gent, P. and J. McWilliams, 1990: Isopycnal mixing in ocean circulation models. *J. Phys. Oceanogr.*, **20**, 150–155.

Gent, P., J. Willebrand, T. McDougal, and J. McWilliams, 1995: Parameterizing eddy-induced tracer transports in ocean circulation models. *J. Phys. Oceanogr.*, **25**, 463–475.

Gent, P. R. and J. C. McWilliams, 1996: Eliassen-palm fluxes and the momentum equations in non-eddy-resolving ocean circulation models. *J. Phys. Oceanogr.*, **26**, 2539–2547.

Gill, A. E., J. S. Green, and A. J. Simmons, 1974: Energy partition in the large-scale ocean circulation and the production of mid-ocean eddies. *J. Marine Res.*, **21**, 499–528.

Gille, S. T., K. Speer, J. R. Ledwell, and A. C. Naveira Garabato, 2007: Mixing and stirring in the southern ocean. *EOS*, **88 (39)**, 382–383.

Gourestski, V. and K. Kolterman, 2004: Woce global hydrographic climatology. Tech. rep., Berichte des Bundesamtes fur Seeschifffahrt und Hydrohraphie.

Greatbatch, R., 1998: Exploring the realtionship between eddy-induced transport velocity, vertical momentum transfer, and the isopycnal flux of potential vorticity. *J. Phys. Oceanogr.*, **28**, 422–432.

Green, J. S., 1970: Transfer properties of the large-scale eddies and the general circulation of the atmosphere. *Quart. J. Roy. Meteor. Soc.*, **96**, 157–185.

Greenslade, M. D. and P. Haynes, 2008: Vertical transition in transport and mixing in baroclinic flows. *J. Atmos. Sci.*, **65**, 1137–1158.

Hallberg, R. and A. Gnanadesikan, 2006: The role of eddies in determining the structure and response of the wind-driven southern hemisphere overturning: Results from the modeling eddies in the souther ocean (meso) project. *J. Phys. Oceanogr.*, **36**, 2232–2252.

Haney, R. L., 1971: Surface thermal boundary condition for ocean circulation models. *J. Phys. Oceanogr.*, **1**, 241–248.

Haynes, P., D. A. Poet, and E. Shuckburgh, 2007: Transport and mixing in kinematic and dynamically consistent flows. *J. Atmos. Sci.*, **64**, 3640–3652.

Haynes, P. and E. Shuckburgh, 2000a: Effective diffusivity as a diagnostic of atmospheric transport. part i: stratosphere. *J. Geophys. Res*, **105**, 22777–22794.

Haynes, P. and E. Shuckburgh, 2000b: Effective diffusivity as a diagnostic of atmospheric transport. part ii: Troposphere and lower stratosphere. *J. Geophys. Res*, **105**, 795–810.

Held, I. and T. Schneider, 1999: The surface branch of the zonally averaged mass transport circulation in the troposphere. *J. Atmos. Sci.*, **56**, 1668–1697.

Held, I. M. and V. D. Larichev, 1996: A scaling theory for horizontally homogeneous, baroclinically unstable flow on a beta plane. *J. Atmos. Sci.*, **53** (7), 946–953.

Henning, C. C. and G. K. Vallis, 2005: The effects of mesoscale eddies on the stratification and transport of an ocean with a circumpolar channel. *J. Phys. Oceanogr.*, **35**, 880–897.

Hill, C., D. Ferreira, J.-M. Campin, J. Marshall, R. Abernathey, and N. Barrier, 2011: Controlling spurios diapycnal mixing in eddy-resolving height-coordinate ocean models: Insights from virtual deliberate tracer release experiments. *Ocean Modelling.*

Holloway, G., 1986: Estimation of oceanic eddy transports from satellite altimetry. *Nature*, **323**, 343–344.

Holloway, G., 1997: Eddy transport of thickness and momentum in layer and level models. *J. Phys. Oceanogr.*, **27**, 1153–1158.

Hughes, C. W., 1997: Comments on on the obscurantist physics of 'form drag' in theorizing about the circumpolar current. *J. Phys. Oceanogr.*, **27**, 209–210.

Hughes, C. W. and B. A. de Cuevas, 2001: Why western boundary currents in realistic oceans are inviscid: A link between form stress and bottom pressure torques. *J. Phys. Oceanogr.*, **31**, 2871–2885.

Hutchinson, D. K., A. M. Hogg, and J. R. Blundell, 2010: Southern ocean response to relative velocity wind stress forcing. *J. Phys. Oceanogr.*, **40**, 326–340.

Ito, T. and J. Marshall, 2008: Control of lower-limb overturning circulation in the southern ocean by diapycnal mixing and mesoscale eddy transfer. *J. Phys. Oceanogr.*, **38**, 2832–2845.

Ivchenko, V. O., K. J. Richards, and D. P. Stevens, 1996: The dynamics of the antarctic cicumpolar current. *J. Phys. Oceanogr.*, **26**, 753–785.

Jackett, D. and T. McDougall, 1997: A neutral density variable for the world's oceans. *J. Phys. Oceanogr.*, **27**, 237–263.

Jansen, M. and R. Ferrari, 2012: Macroturbulent equilibration in a thermally forced primitive equation system. *J. Atmos. Sci.*

Johnson, G. C. and H. L. Bryden, 1989: On the size of the antarctic circumpolar current. *Deep Sea Res.*, **36**, 39–53.

Karsten, R., H. Jones, and J. Marshall, 2002: The role of eddy transfer in setting the stratification and transport of a circumpolar current. *J. Phys. Oceanogr.*, **32**, 39–54.

Karsten, R. and J. Marshall, 2002a: Constructing the residual circulation of the acc from observations. *J. Phys. Oceanogr.*, **32**, 3315–3272.

Karsten, R. H. and J. Marshall, 2002b: Testing theories of the vertical stratification of the acc against observations. *Dyn. Atmos. Oceans*, **36**, 233-246.

Keating, S. R., A. J. Majda, and K. S. Smith, 2012: New methods for estimating ocean eddy heat transport using satellite altimetry. *Mon. Weather Rev.*

Keffer, T. and G. Holloway, 1988: Estimating southern ocean eddy flux of heat and salt from satellite altimetry. *Nature*, **332**, 624 - 626.

Killworth, P. D., 1997: On the parameterization of eddy transfer: Part i: Theory. *J. Marine Res.*, **55**, 1171-1197.

Killworth, P. D. and C. Hughes, 2002: The antarctic circumpolar current as a free equivalent-barotropic jet. *J. Marine Res.*, **60**, 19-45.

Klocker, A., R. Ferrari, and J. H. LaCasce, 2011a: Estimating supression of eddy mixing by mean flows. *J. Phys. Oceanogr.*

Klocker, A., R. Ferrari, J. H. LaCasce, and S. T. Merrifield, 2011b: Reconciling float-based and tracer-based estimates of eddy diffusivities. *J. Phys. Oceanogr.*

Kuo, A., R. A. Plumb, and J. Marshall, 2005: Transformed eulerian-mean theory. part ii: Potential vorticity homogenization and equilibrium of a wind- and buoyancy-driven zonal flow. *J. Phys. Oceanogr.*, **45**, 175-187.

Kushner, P. J. and I. M. Held, 1998: A test, using atmospheric data, of a method for estimating oceanic eddy diffusivity. *Geophys. Res. Lett.*, **25 (22)**, 4213-4216.

LaCasce, J. H., 2008: Statistics from lagrangian observations. *Progress in Oceanography*, **77**, 1-29.

Lagerloef, G., G. Mitchum, R. Lukas, and P. Niiler, 1999: Tropical pacific near-surface currents estimated from altimeter, wind and drifter data. *J. Geophys. Res.*, **104**, 313-23.

Lapeyre, G. and I. M. Held, 2003: Diffusivity, kinetic energy dissipation, and closure theories for the poleward eddy heat flux. *J. Atmos. Sci.*, **60**, 2907-2917.

Large, W. G., J. C. McWilliams, and S. C. Doney, 1994: Oceanic vertical mixing: A review and a model with a nonlocal boundary layer parameterization. *Reviews of Geophysics*, **32 (4)**, 363-403.

Large, W. G. and S. G. Yeager, 2009: The global climatology of an interannually varying air-sea flux data set. *Clim. Dyn.*, **33 (2-3)**, 341-364.

Larichev, V. D. and I. M. Held, 1995: Eddy amplitudes and fluxes in a homogeneous model of fully developed baroclinic instability. *J. Atmos. Sci.*, **25**, 2285-2297.

Le Quéré, C., M. R. Raupach, J. G. Canadell, and G. Marland, 2009: Trends in the sources and sinks of carbon dioxide. *Nature Geoscience*, **2**, 831-837.

Ledwell, J. R., L. C. St. Laurent, and J. B. Girton, 2011: Diapycnal mixing in the antarctice circumpolar current. *J. Phys. Oceanogr.*, **41 (241-246)**.

Ledwell, J. R., A. J. Watson, and C. S. Law, 1998: Mixing of a tracer in the pycnocline. *J. Geophys. Res.*, **103 (C10)**, 21,499–21,592.

Levitus, S., J. I. Antonov, T. P. Boyer, R. A. Locarnini, H. E. Garcia, and A. V. Mishonov, 2998: Global ocean heat content 1955 – 2008 in light of recently revealed instrumentation problems. *Geophys. Res. Lett.*, **36**, L07608.

Lorenz, E. N., 1955: Available potential energy and the maintenance of the general circulation. *Tellus*, **7 (2)**, 157–167.

Lumpkin, R. and K. Speer, 2007: Global meridional overtuning. *J. Phys. Oceanogr.*, **37**, 2550–2537.

Marshall, D., 1997: Subduction of water masses in an eddying ocean. *J. Marine Res.*, **55**, 201–222.

Marshall, D. P., J. R. Maddison, and P. S. Berloff, 2012: A framework for parameterizing eddy potential vorticity fluxes. *J. Phys. Oceanogr.*

Marshall, G., 2003: Trends in the southern annular mode from observations and reanalyses. *J. Climate*, **16**, 4134–4144.

Marshall, J., 1981: On the parameterization of geostrophic eddies in the ocean. *J. Phys. Oceanogr.*, **11**, 1257–1271.

Marshall, J., A. Adcroft, C. Hill, L. Perelman, and C. Heisey, 1997a: A finite-volume, incompressible navier stokes model for studies of the ocean on parallel computers. *J. Geophys. Res.*, **102**, 5753–5766.

Marshall, J., C. Hill, L. Perelman, and A. Adcroft, 1997b: Hydrostatic, quasi-hystrostatic, and non-hydrostatic ocean modeling. *J. Geophys. Res.*, **102**, 5733–5752.

Marshall, J., D. Olbers, H. Ross, and D. Wolf-Gladrow, 1993: Potential vorticity constraints on the dynamics and hydrography of the southern ocean. *J. Phys. Oceanogr.*, **23**, 465–487.

Marshall, J. and T. Radko, 2003: Residual mean solutions for the antarctic circumpolar current and its associated overturning circulation. *J. Phys. Oceanogr.*, **33**, 2341–2354.

Marshall, J. and T. Radko, 2006: A model of the upper branch of the meridional overturning of the southern ocean. *Progress in Oceanography*, **70**, 331–345.

Marshall, J., E. Shuckburgh, H. Jones, and C. Hill, 2006: Estimates and implications of surface eddy diffusivity in the southern ocean derived from tracer transport. *J. Phys. Oceanogr.*, **36**, 1806–1821.

Marshall, J. and G. Shutts, 1981: A note on rotational and divergent eddy fluxes. *J. Phys. Oceanogr.*, **21**, 1677–1681.

Marshall, J. and K. Speer, 2011: Closing the meridional overturning circulation through southern ocean upwelling. *Nature Geoscience*.

Mazloff, M., 2008: The southern ocean meridional overturning circulation as diagnosed from an eddy permitting state estimate. Ph.D. thesis, Massachusetts Institute of Technology.

Mazloff, M., P. Heimbach, and C. Wunsch, 2009: An eddy permitting southern ocean state estimate, in Preparation.

McCarthy, M. C. and L. D. Talley, 1999: Three-dimensional isoneutral potential vorticity structure in the indian ocean. *J. Geophys. Res.*, **104 (C6)**, 13 251–13 267.

McCartney, M. S., 1977: Subantarctic mode water. *A Voyage of Discovery, George Deacon 70th Anniversary Volume*, M. V. Angel, Ed., Pergamon, 103–119.

McIntosh, P. C. and T. J. McDougall, 1996: Isopycnal averaging and the residual mean circulations. *J. Phys. Oceanogr.*, **26**, 1655–1661.

McIntyre, M. and T. Palmer, 1983: Breaking planetary waves in the stratosphere. *Nature*, **305**, 593–600.

McWilliams, J. C., W. R. Holland, and J. H. S. Chow, 1978: A description of numerical antarctic circumpolar currents. *Dyn. Atmos. Oceans*, **2**, 213–291.

Meredith, M. P. and A. M. Hogg, 2006: Circumpolar response of southern ocean eddy activity to a change in the southern annular mode. *Geophys. Res. Lett.*, **33**, L16 608.

Munk, W. and E. Palmén, 1951: Note on the dynamics of the antarctic circumpolar current. *Tellus*, **3**, 53–55.

Nakamura, N., 1996: Two-dimensional mixing, edge formation, and permeability diagnosed in an area coordinate. *J. Atmos. Sci.*, **53**, 1524–1537.

Nakamura, N., 2001: A new look at eddy diffusivity as a mixing diagnostic. *J. Atmos. Sci.*, **58**, 3685–3702.

Nakamura, N. and J. Ma, 1997: Modified lagrangian-mean diagnostics of the stratospheric polar vortices 2. nitrous oxide and seasonal barrier migration in the cryogenic limb array etaion spectrometer and skyhi general circulation model. *J. Geophys. Res.*, **102**, 25,721–25,735.

Naveira Garabato, A. C., R. Ferrari, and K. L. Polzin, 2010: Eddy-induced mixing in the southern ocean. *J. Phys. Oceanogr.*

Olbers, D., 1998: Comments on "on the obscurantist physics of 'form drag' in theorizing about the circumpolar current". *J. Phys. Oceanogr.*, **28**, 1647-1655.

Olbers, D., D. Borowski, C. Voelker, and J. Wolff, 2004: The dynamical balance, transport and circulation of the antarctic circumpolar current. *Antarctic Science*, **16**, 439-470.

Osborn, T. R. and C. S. Cox, 1972: Oceanic fine structure. *Geo. Astro. Fluid Dyn.*, **3 (1)**, 321-345.

Pedlosky, J., 1987: *Geophysical Fluid Dynamics*. Springer.

Picaut, J., S. P. Hayes, and M. J. McPhaden, 1989: Use of the geostrophic approximation to estimate time-varying zonal currents at the equator. *J. Geophys. Res.*, **94 (C3)**, 3228-3236.

Plumb, R. A., 1986: Three-dimensional propagation of transient quasi-geostrophic eddies and its relationship with the eddy forcing of the time-mean flow. *J. Atmos. Sci.*, **43 (1657-1678)**.

Plumb, R. A., 2007: Dynamics and transport in the stratosphere (12.831), unpublished Class Notes.

Plumb, R. A. and R. Ferrari, 2005: Transformed eulerian-mean theory. part i: Non-quasigeostrophic theory for eddies on a zonal-mean flow. *J. Phys. Oceanogr.*, **35**, 165-174.

Plumb, R. A. and J. D. Mahlman, 1987: The zonally-averaged transport characteristics of the gfdl general circulation/tracer model. *J. Atmos. Sci.*, **44**, 298-327.

Polvani, L., D. Waugh, G. Correa, and S.-W. Son, 2011: Stratospheric ozone depletion: the main driver of 20th century atmospheric circulation changes in the southern hemisphere. *J. Climate*.

Prandtl, L., 1925: Bericht untersuchungen zur ausgebildeten turbulenz. *Zs. angew. Math. Mech.*, **5**, 136-139.

Prather, M. J., 1986: Numerical advection by conservation of second-order moments. *J. Geophys. Res.*, **91 (D6)**, 6671-6681.

Rhines, P., 1979: Geostrophic turbulence. *Annu. Rev. Fluid Mech.*, **11**, 401-441.

Rhines, P. and W. Young, 1982: How rapidly is a passive scalar mixed within closed streamlines. *J. Fluid Mech.*, **133**, 133-145.

Rintoul, S., C. Hughes, and D. Olbers, 2001: *The antarctic circumpolar current system*, 171-302. Academic Press, London.

171

Risien, C. M. and D. B. Chelton, 2008: A global climatology of surface wind and wind stress fields from eight years of quikscat scatterometer data. *J. Phys. Oceanogr.*, **38 (2379-2413)**.

Rogerson, A. M., P. D. Miller, L. J. Pratt, and C. K. R. T. Jones, 1999: Lagrangian motion and fluid exchange in a barotropic meandering jet. *J. Phys. Oceanogr.*, **29**, 2635–2655.

Sallée, J. B., K. Speer, R. Morrow, and R. Lumpkin, 2008: An estimate of lagragian eddy statistics and diffusion in the mixed layer of the southern ocean. *J. Marine Res.*, **66 (4)**, 441–463.

Scott, R. B. and D. G. Furnival, 2011: Assessment of traditional and new eigenfunction bases applied to extrapolation of surface geostrophic current time series to below the surface in an idealized primitive equation simulation. *J. Phys. Oceanogr.*

Shuckburgh, E. and P. Haynes, 2003: Diagnosing transport and mixing using a tracer-based coordinate system. *Physics of Fluids*, **15 (11)**, 3342–3357.

Shuckburgh, E., H. Jones, J. Marshall, and C. Hill, 2009a: Quantifying the eddy diffusivity of the southern ocean i: temporal variability. *J. Phys. Oceanogr.*, in Press.

Shuckburgh, E., H. Jones, J. Marshall, and C. Hill, 2009b: Quantifying the eddy diffusivity of the southern ocean ii: spatial variability and the role of the mean flow. *J. Phys. Oceanogr.*, in Press.

Shuckburgh, E., G. Maze, D. Ferreira, J. Marshall, H. Jones, and C. Hill, 2011: Mixed layer lateral eddy fluxes mediated by air–sea interaction. *J. Phys. Oceanogr.*, **41**, 130–144.

Smith, K. S., 2007: The geography of linear baroclinic instability in the earth's oceans. *J. Marine Res.*, **65**, 655–683.

Smith, K. S. and J. Marshall, 2009: Evidence for enhanced eddy mixing at mid-depth in the southern ocean. *J. Phys. Oceanogr.*, **39**, 50–69.

Sokolov, A. P., C. E. Forest, and P. H. Stone, 2003: Comparing oceanic heat uptake in aogcm transient climate change experiments. *J. Climate*, **16**, 1573–1582.

Speer, K., S. Rintoul, and B. Sloyan, 2000: The diabatic deacon cell. *J. Phys. Oceanogr.*, **30**, 3212–3223.

Stammer, D., 1998: On eddy characteristics, eddy transports, and mean flow properties. *J. Phys. Oceanogr.*, **28**, 727–739.

Stephens, C., J. Antonov, T. Boyer, M. Conkright, R. Locarini, T. O'Brien, and H. Garcia, 2001: *World Ocean Atlas 2001, Volume 1: Temperature*, Vol. 49. NOAA Atlas NESDIS.

172

Stone, P., 1978: Baroclinic adjustment. *J. Atmos. Sci.*, **35**, 561–571.

Stone, P. H., 1972: A simplified radiative-dynamical model for the static stability of rotating atmospheres. *J. Atmos. Sci.*, **29 (3)**, 405–417.

Straub, D., 1993: On the transport and angular momentum balance of channel models of the antarctic circumpolar current. *J. Phys. Oceanogr.*, **23 (776-783)**.

Talley, L. D., 2008: Freshwater transport estimates and the global overturning circulation: Shallow, deep and throughflow components. *Progress in Oceanography*, **78**, 257–303.

Taylor, G. I., 1921: Diffusion by continuous movements. *Proc . London Math. Soc.*, **s2-20**, 196–212.

Thompson, A. F., 2008: The atmospheric ocean: eddies and jets in the antarctic circumpolar current. *Phil. Trans. of the Royal Society A*, **366**, 4529–4541.

Thompson, A. F., 2010: Jet formation and evolution in baroclinic turbulence with simple topography. *J. Phys. Oceanogr.*, **40**, 257–274.

Thompson, A. F. and J. B. Sallée, 2011: Jets and topography: Jet transitions and impacts on transport, in Preparation.

Thompson, A. F. and W. R. Young, 2006: Scaling baroclinic eddy fluxes: Vortices and energy balance. *J. Phys. Oceanogr.*, **36**, 720–738.

Thompson, A. F. and W. R. Young, 2007: Two-layer baroclinic eddy heat fluxes: Zonal flows and energy balance. *J. Atmos. Sci.*, **64**, 3214–3232.

Thompson, D. W. J. and J. M. Wallace, 2000: Annular modes in the extratropical circulation. part ii: Trends. *J. Climate*, **13**, 1018–1036.

Toggweiler, J. R., 2009: Shifting westerlies. *Science*, **232**, 1434–1435.

Toggweiler, J. R. and B. Samuels, 1998: On the ocean's large-scale circulation near the limit of no vertical mixing. *J. Phys. Oceanogr.*, **28**, 1832–1853.

Toggweiler, R. and J. Russell, 2008: Ocean circulation in a warming climate. *Nature*, **451**, 286–288.

Treguier, A. M., 1999: Evaluating eddy mxiing coefficients from eddy-resolving oecean models: A case study. *J. Marine Res.*, **57**, 89–108.

Treguier, A. M., I. Held, and V. Larichev, 1997: Parameterization of quasigeostrophic eddies in primitive equation ocean models. *J. Phys. Oceanogr.*, **27**, 567–580.

Treguier, A. M., J. Le Sommer, and J. M. Molines, 2010: Response of the southern ocean to the southern annular mode: Interannual variability and multidecadal trend. *J. Phys. Oceanogr.*, **40 (1659-1668)**.

Tulloch, R., J. Marshall, and K. S. Smith, 2009: Interpretation of the propagation of surface altimetric observations in terms of planetary waves and geostrophic turbulence. *J. Geophys. Res.*, **114**, C02 005.

Vallis, G., 2006: *Atmospheric and Oceanic Fluid Dynamics*. Cambridge University Press.

Viebahn, J. and C. Eden, 2010: Toward the impact of eddies on the response of the southern ocean to climate change. *Ocean Modelling*, **34**, 150 165.

Visbeck, M., J. Marshall, and T. Haine, 1997: Specification of eddy transfer coefficients in coarse-resolution ocean circulation models. *J. Phys. Oceanogr.*, **27**, 381 403.

Watson, A. J. and A. C. Naveira Garabato, 2006: The role of southern ocean mixing and upwelling in glacial-interglacial atmospheric co2 change. *Tellus*, **58B**, 73 87.

Waugh, D. W. and E. R. Abraham, 2008: Stirring in the global surface ocean. *Geophys. Res. Lett.*, **35**, L20 605.

Welander, P., 1973: Lateral friction in the oceans as an effect of potential vorticity mixing. *Geophys. Fluid Dynamics*, **5 (1)**, 173 189.

Winters, K. and E. D'Asaro, 1996: Diascalar flux and the rate of fluid mixing. *J. Fluid Mech.*, **317**, 179 193.

Wolfe, C. and P. Cessi, 2011: The adiabatic pole-to-pole overturning circulation. *J. Phys. Oceanogr.*

Wolfe, C. L. and P. Cessi, 2009: Overturning circulation in an eddy-resolving model: The effect of the pole-to-pole temperature gradient. *J. Phys. Oceanogr.*, **39**, 125 143.

Wolfe, C. L. and P. Cessi, 2010: What sets the strength of the mid-depth stratification and overturning circulation in eddying ocean models?, accepted to JPO.

Wunsch, C. and R. Ferrari, 2004: Vertical mixing, energy, and the general circulation of the ocean. *Annu. Rev. Fluid Mech.*, **36**, 281 314.

Wunsch, C. and P. Heimbach, 2006: Practical global oceanic state estimation. *Physica D*, **230**, 197 208.

Wunsch, C. and P. Heimbach, 2009: The globally integrated ocean circulation (moc), 1992-2006: seasonal and decadal variability. *J. Phys. Oceanogr.*, **39 (2)**, 351 368.

Young, W. R., P. B. Rhines, and C. J. R. Garrett, 1982: Shear-flow dispersion, internal waves and horizontal mixing in the ocean. *J. Phys. Oceanogr.*, **12**, 515 527.

Yuan, G.-C., L. J. Pratt, and C. K. R. T. Jones, 2002: Barrier destruction and lagrangian predictability at depth in a meandering jet. *Dyn. Atmos. Oceans*, **35**, 41–61.

Zhao, R. and G. Vallis, 2008: Parameterizing mesoscale eddies with residual and eulerian schemes, and a comparison with eddy-permitting models. *Ocean Modelling*, **23**, 1–12.

Zhurbas, V. and I. S. Oh, 2003: Lateral diffusivity and lagrangian scales in the pacific ocean as derived from drifter data. *J. Geophys. Res.*, **108 (C5)**, 3141.

Zhurbas, V. and I. S. Oh, 2004: Drifter-derived maps of lateral diffusivity in the pacific and atlantic oceans in relation to surface circulation patterns. *J. Geophys. Res.*, **109**, C05015.

Zurita-Gotor, P. and R. Lindzen, 2004a: Baroclinic equilibration and the maintainance of the momentum balance. part i: A barotropic analog. *J. Atmos. Sci.*, **61**, 1469–1481.

Zurita-Gotor, P. and R. Lindzen, 2004b: Baroclinic equilibration and the maintainance of the momentum balance. part ii: 3d results. *J. Atmos. Sci.*, **61**, 1483–1499.